Astronomy Reports, Vol. 47, No. 9, 2003, pp. 709–716. Translated from Astronomicheskiĭ Zhurnal, Vol. 80, No. 9, 2003, pp. 771–779.
Original Russian Text Copyright © 2003 by Burgin.

Hydrogen Subordinate Line Emission at the Epoch of Cosmological Recombination

M. S. Burgin

Astro Space Center, Lebedev Physical Institute, Russian Academy of Sciences, Profsoyuznaya ul. 84/32, Moscow, 117997 Russia

Received December 10, 2002; in final form, March 14, 2003

Abstract—The balance equations for the quasi-stationary recombination of hydrogen plasma in a blackbody radiation field are solved. The deviations of the excited level populations from equilibrium are computed and the rates of uncompensated line transitions determined. The expressions obtained are stable for computations of arbitrarily small deviations from equilibrium. The average number of photons emitted in hydrogen lines per irreversible recombination is computed for plasma parameters corresponding to the epoch of cosmological recombination. *© 2003 MAIK "Nauka/Interperiodica".*

1. INTRODUCTION

When the cosmological expansion of the Universe lowered the temperature sufficiently, the initially ionized hydrogen recombined. According to [1, 2], an appreciable fraction of the photons emitted at that time in subordinate lines survive to the present, leading to the appearance of spectral lines in the cosmic background (relict) radiation. Measurements of the wavelengths, intensities, and profiles of these lines can provide information about the plasma temperature, density, and redshift corresponding to the epoch of recombination, as well as the duration of this epoch.

In a general formulation, computing the intensities and profiles of recombination lines requires the solution of coupled non-stationary differential equations describing the radiative transfer and the evolution of the distributions of atoms over their energy levels. However, in reality, the problem is drastically simplified by the smallness of two dimensionless parameters: the ratio of the numbers of baryons and photons and the ratio of the relaxation time for the distribution of hydrogen atoms over levels with principal quantum numbers $n \geq 2$ to the characteristic time for variations of the degree of ionization. These small parameters enable us to separate the computation of the emission coefficients into three subtasks that can be considered independent in a first approximation.

First, the recombination kinetics can be computed for a given baryon density, radiation temperature, and cosmological expansion rate. According to [3, 4], the two-photon decay of the 2S state is the main process responsible for the growth of the ground-state population of the hydrogen atoms with time, since the Universe is virtually completely opaque in the resonance lines and Lyman continuum, and the small probability of this decay is responsible for the appreciable difference between the actual degree of ionization and the value corresponding to the Saha–Boltzmann equilibrium. A detailed analysis of processes affecting the recombination rate and computations of the temporal behavior of the degree of ionization for various scenarios for the cosmological expansion are presented in [5, 6].

The second task involves computing the rate of emission of suprathermal photons in excess of the Planck background radiation, that is, the rate of uncompensated transitions. To first approximation, the rate of uncompensated transitions in subordinate lines is proportional to the rate of uncompensated transitions $2 \Rightarrow 1$. Here and below, $n_u \Rightarrow n_l$ denotes the transition between states with the principal quantum numbers n_u and n_l. The technique of computing the proportionality coefficient by modeling a random walk of electrons between energy levels was proposed in [7], while [8, 9] present an approximate analytical solution for the corresponding equation.

Finally, the third task of solving for the non-stationary radiative transfer in the recombination lines must be carried out in order to compute the distortions in the contemporary relict-radiation spectrum. Since these distortions are extremely weak and their reverse effect on the recombination and population of excited levels is negligible, computing the radiation intensity reduces to integrating the functions determined previously.

The present work is devoted to solving the second task. A numerical solution of the balance equation for the recombination of plasma exposed to the relict radiation yields the populations of excited hydrogen levels and the rates of uncompensated transitions in subordinate lines.

2. FUNDAMENTAL ASSUMPTIONS

We adopt below the physical scenario proposed in [7, 8]. An ensemble of hydrogen atoms located in discrete levels with $n \geq 2$ is considered. The ensemble interacts with a blackbody radiation field and hydrogen plasma, with the radiation and plasma temperatures specified to be equal. The populations in levels with the same n but different orbital quantum numbers l are proportional to the corresponding statistical weights.

Radiative (both spontaneous and stimulated) transitions and transitions induced by inelastic electron collisions occur between levels $n \geq 2$. Radiative recombinations to levels $n \geq 2$ add new atoms to the ensemble, while photoionization by the relict radiation removes atoms from the ensemble.

In addition, emptying and replenishment of the ensemble occur due to transitions to and from the $n = 1$ level. Photons emitted in resonance lines are absorbed almost immediately, with the transition rates of emission and absorption being equal for each $\mathrm{L}_\beta, \mathrm{L}_\gamma, \ldots$ line, so that these processes completely compensate each other.

There is not complete compensation for L_α, and the net effect of these transitions is modeled by the outflow $2 \Rightarrow 1$, with the rate being proportional to the population in the second level. In the approximation used, this outflow of atoms from the ensemble is responsible for the nonequilibrium distribution of atoms over the $n \geq 2$ levels and, ultimately, for the formation of lines.

The relaxation of the atomic distribution within the $n \geq 2$ ensemble is determined by allowed transitions, with characteristic times $t_i \approx 10^{-8}$ s. The characteristic time for the evolution of external processes coincides with the duration of the epoch of recombination t_e; that is, 10^4–10^5 yrs. The small ratio t_i/t_e enables us to consider the distribution of the ensemble atoms over their levels to be stationary.

3. INPUT EQUATIONS

Let N_e be the electron density, T the temperature of the recombining plasma, and N_i the number density of atoms excited to the level with principal quantum number $n(i) = i + 1$. We denote $N_i^{(0)}$ to be the corresponding number density for the case when the plasma, radiation, and atoms with $n \geq 2$ are in full thermodynamic equilibrium.

In accordance with [5, 7], we will divide the atomic hydrogen levels considered into two groups, with their boundary being determined by the parameters M and M', where $2 < M \leq M'$. For $n(i) \leq M$, we determine the densities N_i from the stationarity conditions, and assume $N_i = N_i^{(0)}$ for $M < n(i) \leq M'$.

In the approximation used, the stationarity conditions take the form

$$\sum_{j=1}^{K} R_{ji}N_j - L_iN_i + B_i = 0, \tag{1}$$

where $K = M - 1$ is the order of the stationarity equations solved below. The term $R_{ji}N_j$ describes transitions within the ensemble, L_iN_i processes that extract atoms from the ensemble, and B_i processes that add new atoms to the ensemble.

The coefficients of this equation are determined by the relations

$$R_{ji} = R^r_{ji} + R^e_{ji} \quad (i \neq j), \tag{2}$$

$$R^r_{ji} = A_{n(j)n(i)}\left(1 + n_{ph}(E_{ij})\right) \quad (j > i), \tag{3}$$

$$R^r_{ji}N_j^{(0)} = R^r_{ij}N_i^{(0)} \quad (i \neq j), \tag{4}$$

$$R^e_{ji} = N_e q_{n(j)n(i)} \quad (j < i), \tag{5}$$

$$R^e_{ji}N_j^{(0)} = R^e_{ij}N_i^{(0)} \quad (i \neq j), \tag{6}$$

$$R_{ii} = -\sum_{j=1}^{i-1} R_{ji} - \sum_{j=i+1}^{K} R_{ji},$$

$$L_i = L_i^{(0)} + \sigma L_i^{(1)}, \tag{7}$$

$$L_i^{(0)} = R_{n(i)c}(T) + \sum_{k=M+1}^{M'} R_{ik},$$

$$L_i^{(1)} = \begin{cases} 1 & \text{for } i = 1 \\ 0 & \text{for } i > 1 \end{cases}$$

and

$$B_i = L_i^{(0)}N_i^{(0)}. \tag{8}$$

Here, A_{ul} is the Einstein coefficient for the spontaneous transition $u \Rightarrow l$, $n_{ph}(E)$ is the number filling factor for relict photons with energy E, E_{ij} is the energy of the transition $n(i) \Rightarrow n(j)$, q_{lu} is the coefficient for collisional excitation of the transition $l \Rightarrow u$,

$$R_{nc} = c\int_{E(n)}^{\infty} a_n(E_{ph})\rho_{ph}(E_{ph})dE_{ph} \tag{9}$$

is the rate of relict photoionization from the level n, c is the speed of light, a_n is the cross section for ionization from level n, E_{ph} is the photon energy, $\rho_{ph}(E_{ph})$ is the spectral density of relict photons with temperature T, R_{cn} is the coefficient for recombination to the level n (taking into account transitions stimulated by the relict radiation), and $E(n)$ is the photoionization threshold for the level with principal quantum number n. Equations (4), (6), and (8) result from the principle of detailed equilibrium.

The quantities $L_i^{(0)}$ describe those processes that remove atoms from the ensemble and are precisely compensated by the addition of new atoms to the ensemble in a complete equilibrium, while Eq. (7) formally expresses the fact that the uncompensated outflow from the level $i = 1$ (i.e., $n = 2$) at the rate $\sigma L_1^{(1)} N_1 = \sigma N_1$ is the only origin of deviations from equilibrium.

If the two-photon transition $2 \Rightarrow 1$ were the sole process resulting in transitions between the ground state and excited levels, and the populations of sublevels with various angular momenta were proportional to the corresponding statistical weights, the value of σ could be easily computed in the explicit form $\sigma = g_{2\mathrm{S}} A_{2\mathrm{S}\Rightarrow 1\mathrm{S}}/(g_{2\mathrm{S}} + g_{2\mathrm{P}})$. Here, $g_{2\mathrm{S}} = 1$ and $g_{2\mathrm{P}} = 3$ are the statistical weights of the 2S and 2P states, and $A_{2\mathrm{S}\Rightarrow 1\mathrm{S}} = 8.23\ \mathrm{c}^{-1}$ is the rate of two-photon decays of the 2S state.

In reality, we must take into account other processes, namely the two-photon transitions $1\mathrm{S} \Rightarrow 2\mathrm{S}$, the spread of L_α photons beyond the line profile due to Doppler diffusion and the redshift, etc., as well as deviations of the population ratio for the 2P and 2S levels from equilibrium [5, 6]. As a result, σ depends on the parameters of the plasma, and computing σ is only one component of the computation of the recombination kinetics, making this expression for σ only a rough estimate.

4. SOLUTIONS OF STATIONARITY EQUATIONS

Matrix notation is more convenient for solving Eqs. (1). Let us introduce the $K \times 1$ matrices

$$\mathbf{N} = \begin{pmatrix} N_1 \\ \vdots \\ N_K \end{pmatrix}, \quad \mathbf{N}^{(0)} = \begin{pmatrix} N_1^{(0)} \\ \vdots \\ N_K^{(0)} \end{pmatrix}, \quad \mathbf{B} = \begin{pmatrix} B_1 \\ \vdots \\ B_K \end{pmatrix},$$

the $K \times K$ matrix

$$\mathbf{R} = \begin{pmatrix} R_{11} & \cdots & R_{1K} \\ \vdots & \ddots & \vdots \\ R_{K1} & \cdots & R_{KK} \end{pmatrix},$$

and the diagonal $K \times K$ matrices

$$\mathbf{L}^{(m)} = \begin{pmatrix} L_1^{(m)} & \cdots & 0 \\ \vdots & \ddots & \vdots \\ 0 & \cdots & L_K^{(m)} \end{pmatrix},$$

where $m = 0,\ 1$. With this notation, Eqs. (1) take the form

$$(\mathbf{Q} - \sigma \mathbf{L}^{(1)})\mathbf{N} + \mathbf{B} = 0, \qquad (10)$$

where $\mathbf{Q} = \mathbf{R}^\dagger - \mathbf{L}^0$ and $\mathbf{R}^\dagger$ denotes the transposition of the matrix $\mathbf{R}$. It can easily be shown that $\mathbf{Q} - \sigma \mathbf{L}^{(1)}$ is a nondegenerate matrix for any $\sigma \geq 0$, so that Eq. (10) has the unique solution

$$\mathbf{N}(\sigma) = -(\mathbf{Q} - \sigma \mathbf{L}^{(1)})^{-1}\mathbf{B}. \qquad (11)$$

After $\mathbf{N}(\sigma)$ is found, the rate of uncompensated radiative transitions Z_{ij} takes the form

$$Z_{ij} = N_i R_{ij}^r - N_j R_{ji}^r. \qquad (12)$$

Formally, (11) and (12) enable us to compute the rate of uncompensated radiative transitions for arbitrary plasma parameters, and thereby obtain a full solution of the problem in the framework of the approximation used. However, for realistic values of the parameters, due to the small relaxation time for the $n \geq 2$ levels, these levels differ only slightly from their equilibrium distribution; that is, $\mathbf{N} \approx \mathbf{N}^{(0)}$. Therefore, $N_i R_{ij}^r \approx N_j R_{ji}^r$, and there will be a subtraction of two close quantities in (12), resulting in a loss of accuracy in the numerical computations.

This situation is completely analogous to that encountered in computations of stellar atmospheres. At a sufficiently high optical depth, the atomic distribution is close to equilibrium, and the numbers of transitions in absorption and emission lines are almost equal, though it is precisely the small difference between them that is important in determining the interaction of the transition with the radiation field. The inaccuracy in calculating the rate of uncompensated transitions as the difference between the absorption and emission rates leads to instability in the computations.

To avoid this difficulty, the small deviations of the distribution from equilibrium and the small number of uncompensated transitions (compared to the total number of transitions in the line) are used as unknowns [10] instead of the distribution function and rates of absorption and emission.

This approach is applicable to the case at hand, and the problem is drastically simplified by the fact that the deviations from the equilibrium distribution depend on a single scalar parameter σ and the temperature of the equilibrium distribution is known *a priori*.

Let us first consider the case $\sigma = 0$. In the absence of an outflow from the $n = 2$ level, the atomic ensemble $2 \leq n \leq M$ interacts only with the plasma, relict radiation, and atomic ensemble $n > M$, which are equilibrium systems with the temperature T. Therefore, the populations of all levels are described by a Boltzmann distribution, and $\mathbf{N}(0) = \mathbf{N}^{(0)}$ is the solution of Eqs. (10),

$$\mathbf{Q}\mathbf{N}^{(0)} + \mathbf{B} = 0. \tag{13}$$

Let us now consider the case $\sigma > 0$. Denoting $\mathbf{N}^{(1)}(\sigma)$ to be a matrix of size $K \times 1$ with the elements $N_i^{(1)}(\sigma) = N_i(\sigma) - N_i^{(0)}$, we obtain using (11) and (13)

$$\mathbf{N}^{(1)}(\sigma) = \left(\left(\mathbf{I} - \sigma\mathbf{P}\mathbf{L}^{(1)}\right)^{-1} - \mathbf{I}\right)\mathbf{N}^{(0)}, \tag{14}$$

where $\mathbf{I}$ is the unit $K \times K$ matrix and $\mathbf{P} = \mathbf{Q}^{-1}$. We can reduce this expression to a numerically stable form in two ways. First, the right-hand side of (14) can be expanded in a series in the vicinity of $\sigma = 0$. Retaining the first nonzero term, we obtain approximately

$$\mathbf{N}^{(1)} \approx \sigma\mathbf{P}\mathbf{L}^{(1)}\mathbf{N}^{(0)}. \tag{15}$$

An advantage of this approach is its applicability to arbitrary matrices $\mathbf{L}^{(1)}$, which means it can be used when some other deviations from the equilibrium are taken into account in addition to those attributed to the outflow $2 \Rightarrow 1$. On the other hand, the accuracy of (15) decreases with increasing σ, and evaluation of the applicability of this approach with realistic parameters requires additional study. In the general case, the radius of convergence of the expansion used is $1/|\lambda_{\max}|$, where $\lambda_{\max}$ is the eigenvalue of the matrix $\mathbf{P}\mathbf{L}^{(1)}$ with the maximum modulus, with the applicability criterion for (15) taking the form of the inequality

$$\sigma|\lambda_{\max}| \ll 1. \tag{16}$$

In our approximation, when $L_1^{(1)}$ is the single nonzero element of the matrix $\mathbf{L}^{(1)}$, we can use an alternative approach that provides a numerically stable expression for $N_i^{(1)}$ that is accurate for arbitrary $\sigma > 0$. Making use of the relations

$$\mathbf{P}\mathbf{L}^{(1)} = \begin{pmatrix} P_{11} & 0 & \cdots \\ \vdots & \vdots & \vdots \\ P_{K1} & 0 & \cdots \end{pmatrix} = \begin{pmatrix} P_{11} \\ \vdots \\ P_{K1} \end{pmatrix} (1 \;\; 0 \;\; \cdots)$$

and transforming (14) using the formula for the changes in the reciprocal matrix produced by low-rank modifications of the initial matrix [11, chapter 0.7.4], we obtain

$$\mathbf{N}^{(1)} = \frac{\sigma}{1 - \sigma P_{11}}\mathbf{P}\mathbf{L}^{(1)}\mathbf{N}^{(0)}, \tag{17}$$

which coincides with (15) for $\sigma \ll 1/P_{11}$.

A nondimensional parameter characterizing deviations from the equilibrium population of level i is

$$d_i(\sigma) = \frac{N_i^{(1)}(\sigma)}{N_i^{(0)}}. \tag{18}$$

It follows from (12), (18), and the equality $N_i^{(0)}R_{ij}^r = N_j^{(0)}R_{ji}^r$ that

$$Z_{ij}(\sigma) = N_i^{(0)}R_{ij}^r(d_i(\sigma) - d_j(\sigma)). \tag{19}$$

When $|d_i|, |d_j| \ll 1$, the calculation of Z_{ij} using (19) results in a relative error that is approximately a factor of $1/\max(|d_i|, |d_j|)$ smaller than the error for the case of direct calculations using (12).

In approximate calculations of the spectral distortions, it is more convenient to use the quantities introduced in [7] instead of Z_{ij}:

$$\eta_{ij} = Z_{ij}/J, \tag{20}$$

where

$$J = \sigma N_1 \tag{21}$$

is the rate of uncompensated $2 \Rightarrow 1$ transitions. The η_{ij} are the average numbers of photons emitted per uncompensated recombination in the corresponding transition to the ground state. In general, η_{ij} depends on σ, but, when criterion (16) is fulfilled, we can approximate $N_1 \approx N_1^{(0)}$, so that $\eta_{ij}(\sigma) \approx \eta_{ij}(0)$, where $\eta_{ij}(0)$ is the limit of $\eta_{ij}(\sigma)$ as $\sigma \to 0$. In addition, the variations of η_{ij} due to changes in the plasma temperature and density are not very large within the range of cosmological parameters considered, and as a first approximation, we can assume η_{ij} to be constant for each transition.

5. NUMERICAL CALCULATIONS

We calculated η_{ij} for plasma temperatures and densities of the recombining plasma in intervals corresponding to periods from the start to the end of the epoch of hydrogen recombination, taking the Hubble constant to be $H_0 = 50$–100 km s^{-1}Mpc^{-1} and $X\Omega_m = 0.001$–1.0. Here, X is the percentage of hydrogen in the total mass of cold matter, $\Omega_m = \rho_m/\rho_{cr}$, ρ_m is the current density of cold matter, $\rho_{cr} = 3H_0^2/(8\pi G)$, and G is the gravitational constant. The start and end times were those when the ratio $N[\mathrm{HI}]/(N[\mathrm{HI}] + N[\mathrm{HII}])$ calculated using the Saha formula was equal to 0.005 and 0.995, respectively.

We calculated A_{ij}, $q_{ij}(T)$, and $a_n(E_{ph})$ using the approximations of [12], and calculated $\mathbf{N}^{(1)}$ using (15). We focused primarily on the transitions with $n_l < 30$ and low $n_u - n_l$, which are most important from the observational point of view.

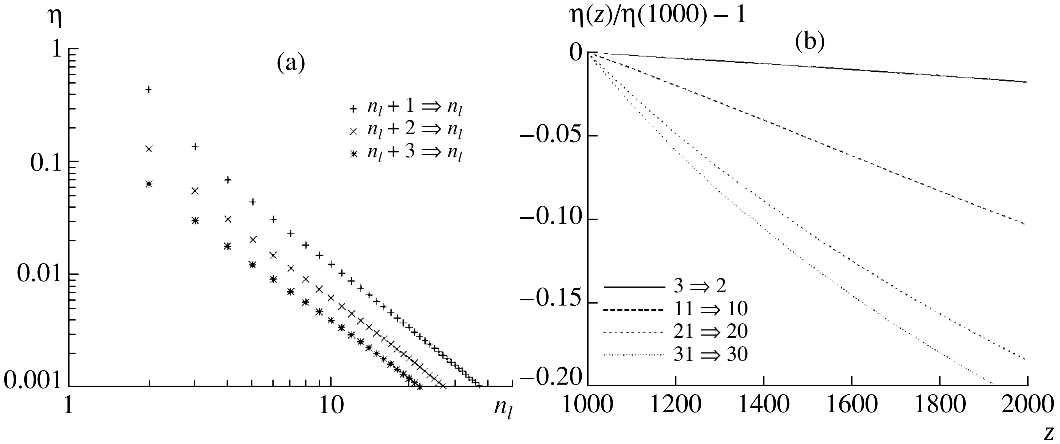

Fig. 1. (a) η as a function of the principal quantum number for the lower level of the transition, n_l, and of the difference between the principal quantum numbers of the upper and lower levels for a plasma with temperature $T = 3756$ K and density $N_e = 2.2 \times 10^2$ cm^{-3}. (b) Variations in η over the hydrogen-recombination time for a cosmological model with $H_0 = 65$ km s^{-1}Mpc^{-1} and $X\Omega_m = 0.03$.

5.1. Results of the Calculations

Figure 1a presents the dependence of η on the numbers of the upper and lower levels of the transition for the plasma parameters $T = 3756$ K and $N_e = 2.2 \times 10^2$ cm^{-3}, typical for the recombination zone. These parameters correspond to a cosmological model with $H_0 = 65$ km/s Mpc and $X\Omega_m = 0.03$, with the redshift being $z = 1374.8$. For this z, a maximum in the intensity of the excess emission in recombination lines is formed provided the recombination is quasi-stationary, that is, provided that, for all z in the range considered, the degree of ionization is close to that calculated via the Saha equation.

Figure 1b shows the behavior of η over the recombination time for a typical cosmological model. To first approximation, we can assume that η is constant. The time dependence of η must be taken into account only for high-accuracy calculations of perturbations of the spectrum of the relict radiation in the radio associated with transitions between high levels.

The parameter η depends not only on z, but also, through the electron density, on the parameters of the cosmological model, since the level populations are determined not only by radiative transitions, but also by inelastic electron collisions.

In the studied range of cosmological parameters, the maximum electron density $N_e = 6.9 \times 10^4$ cm^{-3} corresponds to the start of recombination at $z = 1828$ for the model with $H_0 = 100$ km s^{-1}Mpc^{-1} and $X\Omega_m = 1.0$. For these parameters, "switching off" electron collisions by substituting $R^e_{ji} = 0$ for (5) results in a relative error in $\eta_{30,29}$ that is smaller than 5%.

Electron densities corresponding to realistic cosmological models are more than an order of magnitude lower than the indicated maximum. In addition, the effect of electron collisions on the level populations decreases with decreasing principal quantum number. Thus, for cases of observational interest, the effect of electron collisions changes η by less than 0.5%, and we can neglect this and consider η_{ij} to depend only on temperature.

For plasma parameters typical of the recombination zone, $\sigma|\lambda_{\max}| \approx 3 \times 10^{-3}$, and the criterion (16) indicates a fairly high accuracy for the approximation (15) and the possibility of neglecting the dependence of η on σ. For small z, the accuracy of (15) falls off at the end of recombination, and the error of the approximation $\eta_{ij}(\sigma) \approx \eta_{ij}(0)$ can become significant. For instance, calculations for $H_0 = 50$ km s^{-1}Mpc^{-1}, $X\Omega_m = 0.001$, and $z = 1016$ yield $\sigma|\lambda_{\max}| \approx 0.17$. However, note that only a small amount of recombination occurs in those regions where (16) is violated and the loss of accuracy is significant. Therefore, when calculating the spectral distortions, the dependence of η on σ need only be taken into account either for high-accuracy calculations or for models in which the recombination differs considerably from the quasi-equilibrium case and the number of hydrogen atoms recombining at $z < 1000$ is not small.

5.2. Accuracy of the Calculations and Choice of M and M′

The solution of (10) depends not only on T and N_e, but also on the computational parameters M' and M. For $M, M' \to \infty$ and fixed i and j, $\eta_{ij}(M, M')$ tends to a finite limit. Here and below, $\eta_{ij}(M, M')$ denotes

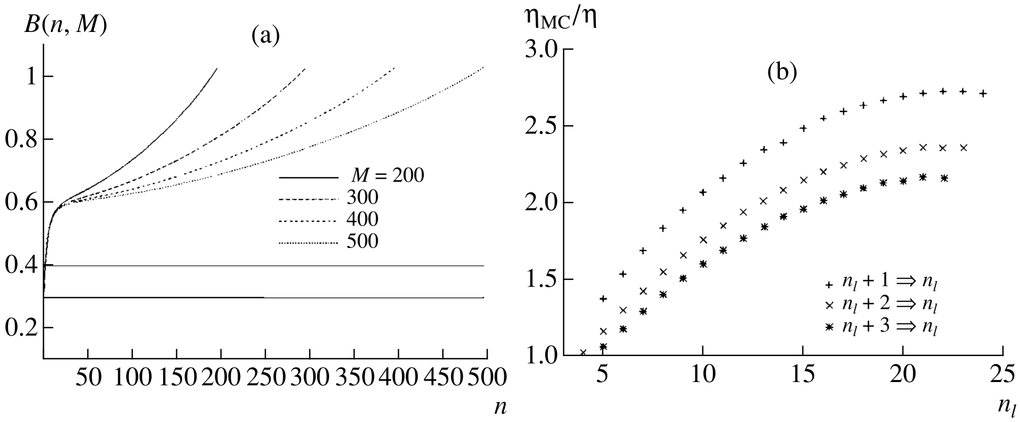

Fig. 2. (a) Comparison of the numerical calculations and the asymptotic solution of [8, 9]. The quantity $B(n, M)$ is defined in the text; the horizontal lines show the limits for B_∞ according to [9]. The calculations were performed for $T = 3756$ K. (b) Calculated values of η compared to the values $\eta_{\rm MC}$ obtained in [7] using Monte Carlo simulations.

the η_{ij} values obtained by solving (10) with the indicated M and M'. This limit should be considered the true solution of the equations describing the physical model used.

The quantity $\eta_{ij}(M', M)$ differs from the true η_{ij} because $M', M < \infty$ and also due to numerical errors arising primarily in the calculation of $\mathbf{P} = \mathbf{Q}^{-1}$. The error associated with the finite nature of M decreases with increasing M, while the error associated with the numerical inversion of $\mathbf{Q}$ increases.

To estimate the accuracy and determine the optimum M, we studied the influence of M and M' on the calculated values of η. For most of the calculations (including those presented in Fig. 1), we chose $M = M' = 300$. Since, for typical temperatures, $\eta_{30,29}(300, 300)/\eta_{30,29}(150, 300) - 1 \approx 0.02$ and $\eta_{30,29}(300, 600)/\eta_{30,29}(300, 300) - 1 \approx 0.01$, and the error decreases with decreasing n_l and n_u, the relative error associated with the finite values of M and M' does not exceed 3% for transitions that are observationally interesting.

The dependence of the number of conditions of the matrix $\mathbf{Q}$ on M, as well as test calculations for large M, show that numerical instability during the matrix inversion can be significant for $M > 350$–400.

The atom–plasma interaction merges and disrupts high levels, which must also be taken into account when choosing M and M'. According to [13], the probability that a level is disrupted in the hydrogen plasma becomes considerable when $n \gtrsim n^* = 1.2 \times 10^3 N_e^{-2/15}$. For plasma parameters typical for recombination, $n^* \approx 600$, and this effect can be neglected.

5.3. Comparison with Approximate Analytical Solution

In [8, 9], the distribution over levels with $n \gg 1$ is approximately described by a continuous distribution $N(\varepsilon)$, where the real variable ε is related to n by the expression $\varepsilon = 1/n^2$. For $\varepsilon \ll \theta$, where $\theta = kT/(1\text{Ry})$, the function $N(\varepsilon)$ approximately satisfies an integral equation with an explicit solution. This solution shows that

$$B(n) = -A_0 d(n) n \frac{\theta^{3/2}}{4J} \exp\left(-\frac{1}{4\theta}\right) \qquad (22)$$

is approximately constant for $n \gg 1$: $B(n) \approx B_\infty$. Here, $A_0 = 0.8 \times 10^{10}$ s^{-1} and J is determined in (21).

Since the equation describing $d(n)$ for $n \gg 1$ is homogeneous, it does not determine the quantity B_∞. In [8], this difficulty was overcome by joining the solution for $n \gg 1$ with another analytical solution describing the distribution for low n. In [9], the limit of $B(n)$ as $n \to \infty$ was estimated to be $B_\infty = 0.35$–0.4.

Figure 2a presents the calculations of $B(n, M)$, i.e., the right-hand side of (22) for $d(n)$ obtained by solving Eqs. (1) with $M' = M$. Since [8, 9] took into account only radiative transitions, our numerical calculations assumed $R^e_{ji} = 0$.

The limit of $B(n, M)$ as $M \to \infty$, i.e., $B(n, \infty)$, corresponds to $B(n)$ in the numerical calculations. Since the neglected levels with $n > M$ are closer to equilibrium with the plasma than levels with $n \le M$, an appropriate inclusion of all levels would decrease $d(n)$; that is, $B(n, M) > B(n, \infty)$. It is also evident that the convergence of $B(n, M)$ to $B(n, \infty)$ is rather slow.

Figure 2a shows that the results are compatible with the existence of a limit $B(n, \infty)$ as $n \to \infty$.

The corresponding estimate of this limit is $B_\infty \approx 0.6$, which exceeds the estimates presented in [9] by a factor of 1.5–1.7. This difference can be partially attributed to the fact that $B(n)$ approaches its asymptotics as $n \to \infty$ slowly, and $B(n)$ differs considerably from its limit in the region where the solutions for low and high n are joined. In [8], the joining was carried out at $\varepsilon/\theta = 0.5$–1.5, which corresponds to $n = 5$–9 for $T = 3756$ K. The numerical calculations for these n yield $B(n, \infty) = 0.41$–0.51, in better agreement with [9]. The residual difference may be associated with inaccuracy of the approximate analytical solution used in [8] for low n.

5.4. Comparison with Monte Carlo Calculations

The Monte Carlo technique developed in [7] considers random walks of electrons in excited levels, and the relevant calculations of η for cosmological plasmas were performed in [14]. The main qualitative conclusions of [7, 14] include a rapid decrease in η with increasing n_l and $\Delta n = n_u - n_l$, a weak dependence of η on temperature, and a weak effect of electron collisions. These conclusions are supported by the present work. However, a detailed comparison reveals some differences that clearly exceed the calculation errors (Fig. 2b).

One possible reason for these differences is that [7] assumes equal probabilities for mutually opposite cyclic transitions; i.e., for sequences of the type $n_1 \Rightarrow n_2 \Rightarrow \cdots \Rightarrow n_k$ and $n_k \Rightarrow \cdots \Rightarrow n_2 \Rightarrow n_1$. In other words, it was assumed that mutually opposite transitions in emission ($n_u \Rightarrow n_l$) and absorption ($n_l \Rightarrow n_u$) precisely compensate each other. This assumption drastically simplifies the Monte Carlo technique and increases the speed of the computations. However, there is not full compensation in the general case, and the error that is introduced by this assumption remains unknown.

The decrease in the differences between our results and those of [7] with decreasing n_l provides indirect support that the origin of these differences is inexactness of the above assumption. Since the background-photon filling numbers are small for energies corresponding to transitions to low levels, the rates of absorption transitions in the corresponding lines are also small. The probability of cyclic sequences involving low levels is therefore low, and the effect of the error introduced when calculating the small contribution of these sequences to the total radiation intensity can significantly affect the final result.

6. DISCUSSION

The method proposed here is based on a simple physical model, and can be used to calculate the emission coefficients of subordinate hydrogen lines with computational errors that do not exceed $\approx 3\%$. Further increase in the accuracy of the calculations is not justified at this time, since the calculation of η contributes additional errors to the computational errors.

The first of these is the error associated with the inexactness of the approximations used in [12] for the rates of radiative and collisional transitions. This error can reach several percent.

The incomplete correspondence between the physical model and the real situation represents another source of errors. The most necessary improvement of the model for the interaction of hydrogen atoms with radiation and plasma described in Section 2 is taking into account the dependence of the level populations on the angular quantum number l. A complete modeling of this effect requires M^2 balance equations, with $M \gtrsim 200$ being required to allow for the influence of high levels on transitions that are observationally interesting. Since it is not possible to solve such a large system of equations using the methods applied here, some decrease in the computational complexity is required. Some possibilities for this are briefly mentioned below.

The simplest option is to take into account the l dependence only for levels with n not exceeding a certain threshold $M'' \ll M$. For small M'', this problem can be solved using the methods described here, although choosing a threshold that is reasonable for the necessary accuracy requires preliminary calculations for larger M''.

The relationships between the elements of the matrix $\mathbf{R}$ that flow from the principle of detailed equilibrium make it possible to construct an explicit symmetrizing transformation for the matrix $\mathbf{Q}$ that reduces to using the unknowns $X_i = N_i/\sqrt{g_i \exp(E_i/kT)}$ in (1), where g_i and E_i are the statistical weight and photoionization threshold of the level. The transformed matrix is negative definite. Moreover, most elements of $\mathbf{Q}$ become identical to zero due to the l selection rules, and the block describing the transitions between levels $n \le M''$ can easily be reduced to a strip form. These properties of the transformed matrix $\mathbf{Q}$ enable us to use special inversion algorithms that are more efficient and stable than those used here for matrices of a general form.

We can use the explicit asymptotic solution of [8, 9] to describe the level populations for high n. Since the influence of levels with $n > M$ will then be taken into account more correctly than here, smaller M will be necessary for the required accuracy. The simplest version of such a numerical–analytical approach is a modification of Eqs. (1) corresponding to the assumption that $d(n) = d(M)M/n$ when $n > M$, which provides a correct asymptotic for $n \to \infty$ and continuous joining of the numerical solution with the analytical asymptotic at $n = M$.

Finally, we note that similar problems must be solved if we wish to study the cosmological recombination of HeII and HeIII, with the l dependence of the populations being taken into account from the very start of the computation of the HeII recombination spectrum.

7. ACKNOWLEDGMENTS

The author is grateful to N.S. Kardashev and V.G. Kurt for drawing his attention to the problem studied, to V.K. Dubrovich and V.L. Kauts for numerous discussions, to I.L. Beigman for indicating the inaccuracy of the approximations in [12] as a possible source of errors, and to V.O. Ponomarev for his assistance in removing errors from the initial version of the article. This work was supported by the Russian Foundation for Basic Research (project code 02-02-16535).

REFERENCES

1. V. K. Dubrovich, Pis'ma Astron. Zh. **1**, 3 (1975) [Sov. Astron. Lett. **1**, 196 (1975)].
2. V. K. Dubrovich and V. A. Stolyarov, Astron. Astrophys. **302**, 635 (1995).
3. Ya. B. Zel'dovich, V. G. Kurt, and R. A. Syunyaev, Zh. Éksp. Teor. Fiz. **55**, 278 (1968).
4. H. J. E. Peebles, Astrophys. J. **153**, 1 (1968).
5. S. I. Grachev and V. K. Dubrovich, Astrofizika **34**, 249 (1991).
6. V. V. Burdyuzha and A. N. Chekmezov, Astron. Zh. **71**, 341 (1994) [Astron. Rep. **38**, 297 (1994)].
7. I. N. Bernshtein, D. N. Bernshtein, and V. K. Dubrovich, Astron. Zh. **54**, 727 (1977) [Sov. Astron. **21**, 409 (1977)].
8. I. L. Beigman and R. A. Syunyaev, Preprint No. 164 (Lebedev Phys. Inst., Moscow, 1978).
9. I. I. Beigman, Astrophys. Space Sci. **11**, 1 (2001).
10. D. Michalas, *Stellar Atmospheres* (Freeman, San Francisco, 1978; Mir, Moscow, 1982).
11. R. Horn and Ch. Johnson, *Matrix Analyses* (Cambridge Univ. Press, Cambridge, England, 1985; Mir, Moscow, 1989).
12. L. C. Johnson, Astrophys. J. **174**, 227 (1972).
13. D. G. Hummer and D. Mihalas, Astrophys. J. **331**, 794 (1988).
14. V. K. Dubrovich and V. A. Stolyarov, Preprint No. 102 (Spec. Astrophys. Obs., Nizhniĭ Arkhyz, 1994).

Translated by V. Badin

Astronomy Reports, Vol. 47, No. 9, 2003, pp. 717–727. Translated from Astronomicheskiĭ Zhurnal, Vol. 80, No. 9, 2003, pp. 780–791.
Original Russian Text Copyright © 2003 by Zheleznyak, Sergeev, Burkhonov.

Optical Observations of the Gravitational Lens SBS1 520+530 at the Maĭdanak Observatory

A. P. Zheleznyak[1], **A. V. Sergeev**[1,2], **and O. A. Burkhonov**[3]

[1]*Institute of Astronomy, Karazin Kharkov State University, Kharkov, Ukraine*
[2]*Institute of Radio Astronomy, National Academy of Sciences of Ukraine,*
Krasnoznamennaya ul. 4, Kharkov, Ukraine
[3]*Institute of Astronomy, Tashkent, Uzbekistan*

Received December 6, 2002; in final form, March 14, 2003

Abstract—Observations of the gravitationally lensed quasar SBS 1520+530 obtained in 2000–2001 on the 1.5-m telescope of the Maĭdanak Observatory (Uzbekistan) are presented. The photometric algorithms used to observe the components of SBS 1520+530 are discussed. The images have a resolution of 0.5″–0.6″, enabling us to detect the lensing galaxy in the R and I bands and to measure its luminosity and coordinates. The results of photometric observations of components A and B of SBS 1520+530 are presented; the light curves show variability on various time scales from a few weeks to a year. A gravitational-lens model for SBS 1520+530 is constructed utilizing all currently available data. © *2003 MAIK "Nauka/Interperiodica".*

1. INTRODUCTION

General-relativity theory predicts the deflection of light rays by a gravitational field, resulting in gravitational lensing, which was detected observationally for the first time in 1979. About 60 gravitationally lensed systems have been identified, most of them being gravitationally lensed quasars. Long-term monitoring of these objects can be used to obtain information about both the cosmological parameters of the Universe (direct estimates of the Hubble constant) and the fine spatial structure of the lensed source, as well as characteristics of the stellar population in the lensing body [1].

The gravitationally lensed quasar SBS 1520+530 was discovered in 1996 at the Special Astrophysical Observatory of the Russian Academy of Sciences (SAO) during observations of a sample of blue objects from the Second Byurakan Survey [2]. The broad-absorption-line quasar SBS 1520+530 is composed of two components, located about 1.6″ from each other and possessing identical spectra with the redshift $z = 1.855$. In addition, two sets of absorption lines with redshifts $z = 0.815$ and $z = 0.716$ have been detected in the spectra of both components. Chavushyan *et al.* [2] suggested that these lines belong to the lensing galaxy that is responsible for the observed splitting of the quasar image. The presence of the lensing galaxy was later confirmed by direct observations of SBS 1520+530 in the infrared by the Canada–France–Hawaii Telescope (CFHT) [3]. The use of an adaptive-optics system and a bright star (12^m) close to SBS 1520+530 as a reference source provided an angular resolution of 0.15″, making it possible to detect the weak galaxy ($\sim 19^m$ in the H band), which is located 0.4″ to the northeast of component B. The detection of the lensing galaxy became a decisive argument in favor of the hypothesis that SBS 1520+530 A, B represents a gravitational lens. The mutual positions of the components of the gravitationally lensed quasar and the lensing galaxy obtained by the CFHT agree well with later observations by the Hubble Space Telescope (HST) [4]. The results of studies of the vicinity of SBS 1520+530 based on deep, multicolor CCD images obtained on the SAO 6-m telescope are presented in [5]. Although it was not possible to detect the lensing galaxy in these images, a weak galaxy 1.8″ to the northeast of component B was detected. Moreover, five other galaxies were detected within 10″ of SBS 1520+530 (this sample is complete to the limiting magnitude $R = 25^m$). Estimates of the brightnesses of components A and B during these observations were presented in [2, 4]; however, no data on variability of the components, associated with either variations in brightness of the lensed source or microlensing events, were published before the onset of our observations. Therefore, the primary aim of our work was detailed photometric monitoring to study possible time variations of the brightnesses of the components of this system.

1063-7729/03/4709-0717$24.00 © 2003 MAIK "Nauka/Interperiodica"

Table 1. Parameters of the CCD cameras

Camera	Format, pixels	Angular size of each pixel	Operational temperature, °C	Number of electrons per readout	Readout noise, electr.
ST-7	675 × 510	0.157″	−35	2.8	15
BroCam	2000 × 800	0.119	−100	1.16	5.5

Table 2. Observational material

Time period	Number of nights	Camera	Filter	Number of frames	FWHM
July 24–September 10, 2000	28	ST-7	R	255	0.8″–1.7″
			V	147	
March 29–September 5, 2001	37	BroCam	R	591	0.5–0.8
			I	202	

2. OBSERVATIONS AND DATA REDUCTION

2.1. Observational Material and Preliminary Data Reduction

SBS 1520+530 is a relatively weak, compact object composed of two sources (the quasar images), which can be considered to be pointlike. The angular distance between components A and B is comparable to the typical size of the atmospheric seeing circle in the focal plane of a large telescope. Therefore, detailed information about the structure and brightness variations of the components can be obtained using sufficiently large ground-based telescopes at sites with good seeing. Our observations were carried out on the 1.5-m telescope of the Maĭdanak Observatory (Maĭdanak Mountain, Uzbekistan). From the point of view of atmospheric characteristics, this observatory is one of the best sites in the Commonwealth of Independent States. According to recent studies [6], the annual-mean seeing reduced to the zenith direction is 0.68″ (over a three-year period), and the average amount of good observing time is about 60% (2000 hours/year). The observing complex, which includes the 1.5-m telescope with diffraction-limited optics and a tower with a forced ventilation system, was specially constructed for observations with high angular resolution.

We observed SBS 1520+530 together with other gravitationally lensed quasars from time to time at the Maĭdanak Observatory in 1998–1999 [7]. The aim of the present paper is to describe the results of observations of SBS 1520+530 carried out in two sessions in 2000–2001. During the 50 days of the first session (Summer and Fall 2000), SBS 1520+530 was observed in a continuous-monitoring regime (on each clear night) using an ST-7 CCD camera mounted at the short focus (1:7.7) of the 1.5-m telescope. In the second session (Spring and Summer 2001), the observations were carried out using the large-scale image system of the 1.5-m telescope (aperture ratio 1:17) and a new BroCam CCD camera, to obtain the maximum resolution possible. Both the ST-7 and BroCam CCDs were equipped with sets of glass filters. In combination with the CCD detector, these provided a photometric system close to the standard Johnson–Cousins $UBVRI$ system. The parameters of the CCD cameras are summarized in Table 1.

A series of ten to twelve R images of SBS 1520+530 with exposure times of 3–5 min was taken on each clear night. During our monitoring, the object was approaching the end of the season of its maximum visibility, and was observed at large zenith distances. The quality of most of the images, as reflected by the full width at half maximum (FWHM) of images of point sources, was about 1″, and reached 0.8″ in the best cases. The second series of observations was carried out from March–September, 2001 under more favorable conditions; the mean point-source FWHM was approximately 0.8″, reaching 0.55″ in some frames.

Three-color V, R, and I series of images composed of ten to fifteen frames with exposures of 5 min and good quality (FWHM $< 0.8''$) were taken on several successive nights (March 29–April 3, 2001), for use in searching for the lensing galaxy.

A summary of the observational material is presented in Table 2. To correct for the nonuniform sensitivity over the field of the CCD cameras, supplementary frames of a field uniformly illuminated by the

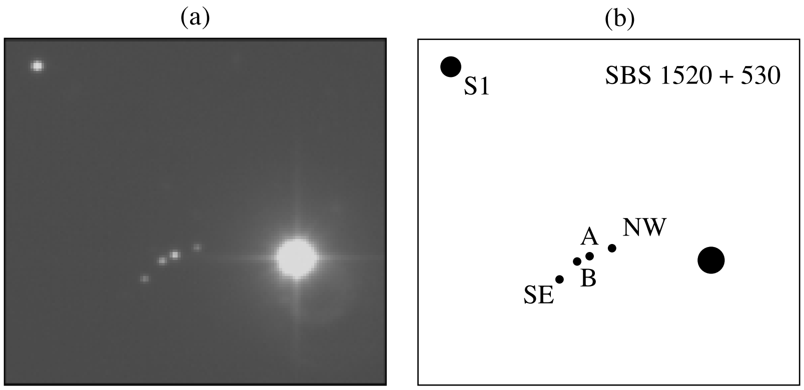

Fig. 1. (a) Image of the gravitationally lensed quasar SBS 1520+530 in the R filter obtained on the 1.5-m Maĭdanak telescope using the ST-7 CCD (North is at the top, East is to the left; the seeing (FWHM) is 0.60″). A halo, speckles, and diffraction rays from a nearby bright star are visible. (b) Designation of objects in the field of SBS 1520+530 (same scale as the left-hand image).

twilight sky (flat fields), as well as frames of the ST-7 dark current, were recorded on each observing night.

Figure 1a presents a fragment of one of the SBS 1520+530 images, and a schematic of the same region labeling various objects in accordance with [2] is shown in Fig. 1b. In addition to components A and B, this figure indicates stars SE and NW, which are close to the SBS 1520+530 system, and the reference star S1, located about 25″ to the northeast. All the photometric measurements were carried out relative to S1, since there are no other bright stars in the frame. (A star to the west of the system is too bright to be a reliable reference source.)

During the second observing session, we performed the absolute calibration of S1 with respect to $BVRI$ standards in Landolt's fields [8]. The brightness of the reference star S1 in these bands was $B = 17.80 \pm 0.03^m$, $V = 17.37^m \pm 0.02$, $R = 17.18 \pm 0.02^m$, and $I = 16.93 \pm 0.02^m$. Analysis of the entire set of observational data did not reveal any variability of S1 exceeding the measurement errors.

The preliminary reduction of the images included the following standard procedures:

—subtraction of the zero bias from the BroCam images;

—subtraction of the average dark-current frame from the ST-7 images;

—correction for the nonuniform sensitivities of both cameras (flat fielding).

After subtracting the mean dark-current frame, the ST-7 images were corrected for nonlinear effects. In the final stage of the preliminary reduction, the images were cleaned of impulsive noise associated with cosmic rays.

To obtain additional astrometric information about the components of the gravitationally lensed quasar SBS 1520+530, we used images from the HST archive obtained on July 20, 1998, using the NICMOS infrared camera [Proposal ID № 7887, Principle Investigator E.E. Falco].

2.2. Data-reduction Method

The intensity distribution in an image $I(x, y)$ formed in the focal plane of a telescope is usually represented by the convolution

$$I(x,y) = \iint f(u,v)g(u-x, v-y)dudv + N(x,y), \tag{1}$$

where $f(u, v)$ is the brightness distribution in the object, $g(u, v)$ is the point spread function (PSF), and $N(x, y)$ is additive noise. In the case of detection by a two-dimensional panoramic receiver, the image $I(x, y)$ is read out by integrating over the area of a photosensitive element of the receiver (a pixel) with a specified sampling step w over the coordinates i and j. The intensity distribution in the image is represented by a two-dimensional readout array $I(i, j)$ on the integer coordinate grid i, j. The PSF is assumed to be zero beyond the region $-m \le x \le m$, $-n \le y \le n$. Consequently, the integral (1) can be represented by the sum

$$I(i,j) = \sum_{k=i-m}^{i+m} \sum_{l=j-n}^{j+n} f(k,l)g(i-k, j-l) + N(i,j), \tag{2}$$

where the two-dimensional PSF $g(i, j)$ is an array of dimension $(2m + 1) \times (2n + 1)$, with m usually taken to be equal to n.

If the object is represented by a set of point sources (δ functions) with various intensities, an image recorded in accordance with (2) will correspond to a set of PSFs, whose integrated intensities will be proportional to the intensities of the sources. Therefore, we can compare the brightnesses of point sources with various intensities by choosing a normalization factor for the PSF. This is the basic principle behind photometry of stellar images using the method of PDF fitting.

The two-dimensional intensity distribution ("shape") of the PSF for a particular image is determined by the sum of distortions of the initial wave front along its entire path from the source to the focal plane. In the case of ground-based observations with perfect telescope optics, the intensity distribution of the PSF is determined by atmospheric inhomogeneities. In general, the form of the PSF $g(u, v)$ depends not only on the difference of the coordinates $u - x$ and $v - y$, but also on the coordinates x and y of a point in the telescope focal plane. In this case, expressions (1) and (2) are applicable only within the so-called isoplanar subregion of the image.

In a real image, the PSF $g(i, j)$ is extracted from the intensity distribution of the recorded stellar image, i.e., from the readouts of the intensity on the discrete coordinate grid. The corresponding intensity maximum (center of the distribution) is located arbitrarily with respect to the center of a pixel (a node of the coordinate grid). The shape of the recorded two-dimensional distribution can be appreciably non-centrally-symmetric.

We processed the images using a numerical PSF whose interpolation errors can be ignored due to the sufficiently detailed spatial frequency of the sample (Table 1). This PSF directly reproduces any real intensity distribution in a stellar image.

We constructed the numerical PSF using the star S1, which is quite close to the components of SBS 1520+530, so that the isoplanar condition is satisfied. The dimension of the PSF array $g(i, j)$ was specified by a synthesized aperture with radius ImaRad, centered on the maximum of the intensity distribution of the stellar image. The aperture radius ImaRad was determined by the "total" size of the stellar image, including the extended outer wings, where the counts almost disappear in the fluctuations of the background-sky counts. Typical values of ImaRad were 4–5 FWHM, depending on the seeing. As is known from works on CCD photometry (for example, [9]), the central, brightest part of a stellar image (with the maximum signal-to-noise ratio) contains nearly all the astrometric and a considerable fraction of the photometric information. Therefore, to center and scale the PSF (which we will call "PSF fitting"), we used the counts inside a synthetic aperture with fitting radius FitRad centered on the maximum of the source intensity distribution. The value of FitRad was usually taken to be about equal to the FWHM of the image.

To construct the numerical PSF, we must first estimate and subtract the mean intensity of the local sky background from the intensity distribution of the star. The intensity of the sky background is derived from a histogram of the background counts in a ring aperture with inner radius ImaRad covering the stellar image. Next, using the pixels within a synthesized aperture with radius FitRad, we determine the coordinates of the center (maximum) of the intensity distribution. Several methods for determining the centers of intensity distributions in CCD images of stars have been suggested [9]; we used least-squares fitting of a two-dimensional Gaussian function. The counts of the stellar intensity within the aperture of radius ImaRad are reduced to the center of the pixel nearest to the maximum (the nearest node of the coordinate grid) via a two-dimensional interpolation, normalized, and stored in a special array. The image-processing algorithms discussed below used the numerical PSF constructed in this way.

2.3. The Galaxy Lensing SBS 1520+530

The large-scale V, R, and I images obtained on the 1.5-m telescope from March 29–April 2, 2001 were used to search for the lensing galaxy. After a preliminary selection, we formed series of 35–40 frames with FWHM $< 0.65''$ in each of the V, R, and I filters. Assuming that the brightness of the components did not vary appreciably during the five days (as is confirmed by a linear regression fit to the photometric results for individual frames), the images in each filter were centered and averaged to get the maximum signal-to-noise ratio. The centering was carried out with respect to the star S1, and the images were reduced to a common coordinate system via a two-dimensional spline interpolation.

Since the expected brightness of the galaxy lensing SBS 1520+530 in the V, R, and I bands is below $20{-}21^m$, the subtraction of the PSF components must be carried out very carefully. Along with the superposition of the PSF wings of components A and B and the neighboring stars NW and SE, another obstacle is the presence of a very bright (12^m) star near SBS 1520+530. As we can see in Fig. 1a, a diffraction ray from the vertical braces of the secondary Cassegrain mirror is superimposed on the images of components A and B. Moreover, the bright star is responsible for a substantial gradient of the background sky brightness in the vicinity of the components of SBS 1520+530. Therefore, the diffraction ray and halo of the bright star near SBS 1520+530 were removed from each of the averaged images before the fitting and subtraction of the component

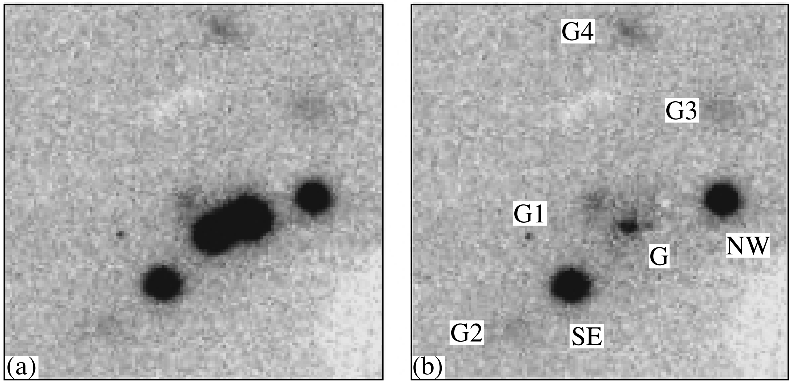

Fig. 2. (a) Mean image of components A and B of the quasar SBS 1520+530 and the stars NW and SE in the *I* filter (negative). The background gradient and a diffraction ray from a neighboring bright star have been removed. The seeing is 0.65″. The range of gradation of the images was chosen to optimize the representation of small intensity variations at the level of the background sky. (b) Same image after subtraction of the numerical PSFs corresponding to components A and B. The lensing galaxy (G) and neighboring background galaxies (G1–G4) are marked.

PSFs. The subtraction algorithm is based on the known central symmetry of the diffraction pattern. Estimates of the subtracted brightness distribution can be obtained in both analytic (approximating the observed brightness distributions by a suitable set of functions) and numerical (interpolating values at the corresponding centrally symmetric points) forms. Applying these two approaches to the real data, we concluded that the second method is preferable due to its simplicity and the lower residual deviations it yielded. A fragment of the *I* image of SBS 1520+530 after subtraction of the diffraction ray and halo of the bright star is presented in Fig. 2a.

The subsequent processing was carried out using the method of iterative PSF subtraction, described in detail in [10]. This method was developed for photometry of several point sources located close to each other (so that the wings of their PSFs overlap). The point sources can be located against a nonuniform background, for example, formed by extended sources. In principle, this method can yield nearly unbiased estimates of the coordinates and brightnesses of the point sources, as well as the intensity distribution of extended background sources. In our implementation of the iterative PSF subtraction method, the unknown variables were the coordinates and normalization factors of the PSFs of each of objects A, B, SE, and NW. The algorithm includes the following sequence of operations:

(1) Constructing the numerical PSF using the image of the star S1.

(2) Specifying the initial size $2q$ of the median window filter ($\sim$ 3–4 FWHM). (The median filter smooths the initial image by computing the median value of a sample of counts within the window $\{-q + i_0 < i < q + i_0, -q + j_0 < j < q + j_0\}$ for each pixel with the coordinates i_0, j_0.)

(3) Estimating the coordinates and normalization factors for each of the objects A, B, NW, and SE (starting with the brightest) via PSF fitting.

(4) Subtracting the array representing the normalized numerical PSFs of A, B, NW, and SE from the image using the current approximation of the coordinates and normalization factors.

(5) Smoothing the residual intensity distribution using the median filter and subtracting the resulting intensity distribution from the initial image.

(6) Repeating step (3) for the finite-difference image and refining the values of the objects' coordinates and normalization factors.

(7) Decreasing the size of the median window filter $2q$ and repeating step (4).

(8) Terminating the iterative process when the size of the median window filter $2q$ becomes comparable to the FWHM of the image.

Table 3. Photometry of the components of SBS 1520+530 (March 29–April 3, 2001)

Object	*R*	*I*	*R–I*
A	18.39 ± 0.02	17.92 ± 0.02	0.47
B	18.92 ± 0.02	18.54 ± 0.02	0.38
NW	19.53 ± 0.03	19.15 ± 0.03	0.38
SE	20.15 ± 0.05	19.06 ± 0.03	1.09
G	21.87 ± 0.30	20.61 ± 0.20	1.26
G1	22.31 ± 0.30	21.29 ± 0.30	1.02

Table 4. Coordinates of the components of SBS 1520+530

Object	CFHT		HST		1.5-m Maĭdanak	
	$\Delta\alpha$	$\Delta\delta$	$\Delta\alpha$	$\Delta\delta$	$\Delta\alpha$	$\Delta\delta$
B	1.427″	−0.652″	1.429″	−0.652″	1.428″	−0.652″
NW	−2.520	0.870	−2.535	0.868	−2.567	0.850
SE	3.401	−2.691	3.400	−2.700	3.433	−2.734
G	1.131	−0.384	1.141	−0.395	1.132	−0.341

Applying this algorithm to the mean I and R images enabled us to detect the lensing galaxy in the residual images. An example of a residual I image depicting the lensing galaxy (after the PSFs of components A and B are subtracted) is shown in Fig. 2b. The residual intensity fluctuations in the locations of A and B do not display systematic deviations and are comparable to the expected photon noise, demonstrating the satisfactory quality of the PSF fitting. The lensing galaxy, which is closer to the residual of component B, is marked by a G. In addition to the galaxy G, Fig. 2b also includes the background galaxies G1–G4, which were described in the earlier papers [2, 4].

The intensity distribution in the image of galaxy G differs substantially from the PSF intensity distributions in both the R and I filters, as was confirmed by PSF fitting followed by subtraction and analysis of the residuals. To determine the coordinates of G and G1, the intensity distributions in the corresponding images were approximated by two-dimensional Gaussians whose parameters were obtained via a least-squares fit. The brightnesses of G and G1 were estimated by integrating the intensities within apertures of diameter 2.1″ centered on the center of the galaxy determined by fitting the two-dimensional Gaussian. Table 3 presents the photometric results in these two filters for components A and B of SBS 1520+530, the galaxies G and G1, and stars SE and NW.

It is also interesting to compare the coordinates of the objects derived via the iterative PSF subtraction with previously published coordinates. The coordinates of component B of the quasar SBS 1520+530, the lensing galaxy G, and stars SE and NW determined relative to component A are presented in Table 4. These data were derived from the average I image, which possesses the maximum signal-to-noise ratio.

For comparison, the relative coordinates of the same objects derived from infrared observations by the CFHT [3] and from HST observations [4] are given in the same table. The formal error in the coordinates of point sources, estimated by the convergence of our frame measurements, is ±0.02″ for A, B, and star NW and ±0.05″ for star SE. The data in Table 4 show good agreement of the relative coordinates of all the pointlike objects with the data obtained in other studies. The agreement between the coordinates of the lensing galaxy can also be considered satisfactory, since the signal-to-noise ratio in the galaxy image was relatively low (~ 40).

Comparing the brightnesses of the lensing galaxy G in the H band [3] with our measurements in the R band, we were able to estimate the color index $R - H \cong 2.6$. This value supports the conjecture [3] that the galaxy lensing SBS 1520+530 is spiral.

Our attempts to identify the lensing galaxy in the V band using this same method failed. This was due to both the relatively low sensitivity of the CCD camera at blue–green wavelengths and the lower intensity of the lensing galaxy, whose V brightness for seeing of $\sim 0.7''$ was below 23.5–24.0^m in an aperture with diameter 2.1″.

We processed the HST images using the numerical PSF generated by the original software package TINYTIM [11]. Four NICMOS images were reduced to Gaussian PSFs, centered, and averaged. The high angular resolution in the resulting image provided additional information about the structures of galaxies G and G1. The galaxies were approximated by anisotropic two-dimensional Gaussian functions, whose parameters were the coordinates of the center, the axis ratio, and the position angle of the major axis. The axis ratio for the lensing galaxy G was $e = 0.50 \pm 0.01$, and its position angle $61° \pm 5°$. The semi-axes of the galaxy G1 differed by less than 5%.

2.4. Photometry of the Components of SBS 1520+530

The available optical observations of several gravitationally lensed quasars demonstrate variability of the brightness of their components, due to both variability of the source itself and microlensing during the passage of the light through the lensing galaxy. In the case of the gravitationally lensed quasar Q0957+561, which was observed in detail for almost 20 years, the variability of the components occurred with the characteristic scale of about 0.01^m/d [12]. Studying the brightnesses of the components of SBS 1520+530 on short time intervals was the main aim of our 50-day monitoring in 2000.

We used a modified version of the well-known algorithm of PSF fitting [13] to carry out photometric observations of the components. A model composed of four PSFs (for components A and B and stars SE and NW) was fitted to each image corrected for the halo of the nearby bright star using the method described above. The fitting procedure is based on minimizing the functional

$$F(A_1, \dots A_4, x_1, y_1 \dots x_4, y_4) = \sum_{i,j} \left\{ \sum_{s=1}^{4} A_s g(i - x_s, j - y_s) - [I(i,j) - B(i,j)] \right\}^2, \tag{3}$$

where $g(i,j)$ is the two-dimensional array representing the numerical PSF, $I(i,j)$ and $B(i,j)$ are the two-dimensional arrays representing the image and background, and A_s, x_s, and y_s are the PSF normalization factors and coordinates of the centers of each object, which are unknowns in the fitting. The minimization of the functional F reduces to solving a set of equations using the least-squares method. Only pixels inside the synthesized aperture with radius FitRad were used to construct the initial set of equations for each object. The value of the fitting radius FitRad was chosen to be comparable to the FWHM of the image, three to five pixels. As follows from the ratio of the R brightnesses of component B and of the lensing galaxy G (Table 3) and the characteristics of our series of images, the influence of G on the fitting for component B is negligible. Therefore, we did not introduce additional parameters describing this galaxy into (3). The quality of the fitting of the above model was estimated by analyzing the residual image obtained by subtracting the numerical PSFs of all four objects from the initial image using the coordinates and normalization factors obtained in the fitting.

Since the total time interval for the recording of a series of images on a specified night did not exceed one hour, the results of the frame-by-frame photometry for each date were averaged using the ensemble normalization procedure of [14], yielding the brightnesses of the components and error estimates. The corresponding light curves for components A and B and star NE are presented in Fig. 3a. Short-term variations in the component brightnesses that significantly exceeded the errors were observed during the entire monitoring period. The characteristic amplitude of the variability of component A was 0.03–0.05^m over intervals of about 10 days, while the brightness of B changed very smoothly and only slightly during the entire monitoring period.

The images obtained in the second observation session (2001) were processed in the same way. All our photometric data, including those published earlier, were used to construct master light curves for the components of SBS 1520+530, which are presented in Fig. 3b. Although the points show scatter due to differences in the CCD detectors, filters, and photometry methods used, we can note long-term variations in the brightnesses of components A and B from season to season. In particular, the data for 2001 are characterized by decreasing brightnesses of both components compared to 2000, especially for B component (its brightness fell by approximately 0.15^m in two months). The amplitude of the variability of components A and B during 1998–2001 is 0.2–0.25^m.

3. MODELING

The observed structure of the gravitationally lensed quasar depends both on the spatial mass distribution inside the lensing galaxy and on the mutual positions of the quasar, gravitational lens, and observer (Fig. 4).

The gravitational focusing equation can be written in angular coordinates [15–17]

$$\mathbf{\Psi}_S = \mathbf{\Psi} + \frac{\tilde{D}}{D_d} \times \mathbf{\Theta}(\mathbf{\Psi}), \tag{4}$$

where $\mathbf{\Psi}$ and $\mathbf{\Psi}_S$ are the angles of the observed and true positions of the point source S, respectively; $\tilde{D} = \frac{D_{ds} D_d}{D_s}$ is the reduced distance; D_d, D_{ds}, and D_s are the distances from the observer to the lens, from the lens to the source, and from the observer to the source, respectively; and $\mathbf{\Theta}(\mathbf{\Psi})$ is the angle of deflection of the ray in the plane of the gravitational lens. This deflection angle is determined by the distribution of the surface mass density of the gravitational lens $\sigma(\psi)$ [15]:

$$\mathbf{\Theta}(\mathbf{\Psi}) = -\frac{4G}{c^2} \int\limits_{\Sigma} \frac{\mathbf{\Psi} - \mathbf{\Psi}'}{(\mathbf{\Psi} - \mathbf{\Psi}')^2} \sigma(\mathbf{\Psi}') d\mathbf{\Psi}'. \tag{5}$$

Here, c is the speed of light, G is the gravitational constant, and the integration is carried out over the surface of the gravitational lens Σ projected onto the celestial sphere. On the other hand, the deflection angle $\mathbf{\Theta}(\mathbf{\Psi})$ can be written as the gradient of the

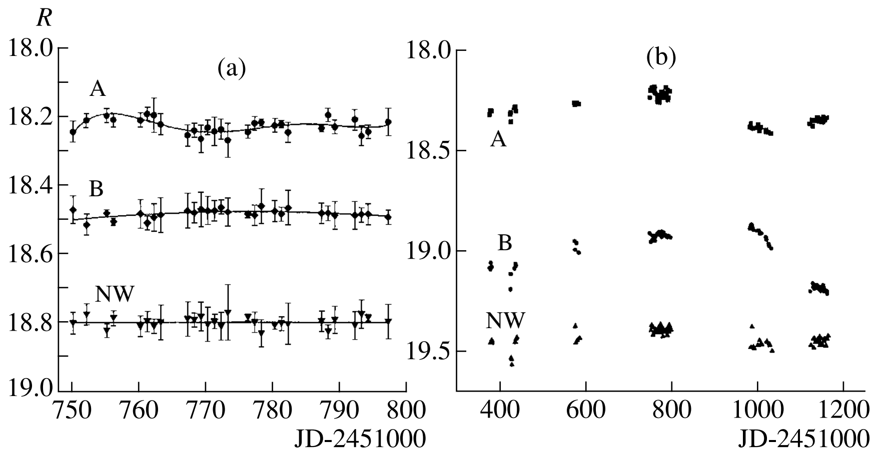

Fig. 3. (a) R light curves of components A and B of the quasar SBS 1520+530 and of star NE obtained during the monitoring in July–September 2000. For comparison, the light curves of component B and the star NW are shifted along the vertical axis by 0.45^m and 0.6^m, respectively. (b) Master light curves of components A and B and the star NE, including all data obtained at the Maĭdanak Observatory.

eikonal $L(\Psi)$ $(\Theta(\Psi) = \nabla L(\Psi))$, which is related to the surface mass density of the gravitational lens by a formula similar to (5) [15]:

$$L(\mathbf{\Psi}) = -\frac{4G}{c^2}\int\limits_{\Sigma} \ln|\mathbf{\Psi} - \mathbf{\Psi}'|\sigma(\mathbf{\Psi}')d\mathbf{\Psi}'. \qquad (6)$$

The number of observed images N and their locations near the gravitational lens are determined for each position of the source Ψ_S by calculating the real roots $\mathbf{\Psi} = \mathbf{\Psi}_m(\mathbf{\Psi}_S)$ $(m = 1, 2 \ldots N)$ of the lens equation (4). The coefficient of amplification of the image brightness q is determined by the Jacobian of the transformation:

$$q_m = \left|\frac{\partial(\Psi_{Sx}, \Psi_{Sy})}{\partial(\Psi_x, \Psi_y)}\right|^{-1}_{\mathbf{\Psi}=\mathbf{\Psi}_m}. \qquad (7)$$

If the intrinsic brightness of the source varies in time, then the relative delay Δt_{mj} between the mth and jth images can also be used as an initial parameter in solving the inverse problem [18]:

$$c\Delta t_{mj} = (1 + z_d)D_d\left\{\frac{D_d}{2\tilde{D}}[(\mathbf{\Psi}_m - \mathbf{\Psi}_s)^2 - (\mathbf{\Psi}_j - \mathbf{\Psi}_s)^2] + L(\mathbf{\Psi}_m) - L(\mathbf{\Psi}_j)\right\}, \qquad (8)$$

where z_d is the lens redshift.

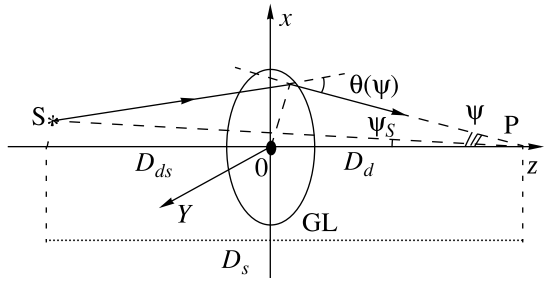

Fig. 4. Mutual positions of the source S, macrolensing galaxy GL, and observer P.

Formulas (4)–(8) are the basic equations for solving the inverse problem of reconstructing the lens and source parameters. Since we have only a limited set of data (the mutual positions of two images of the quasar, the position and shape of the lensing galaxy, and the difference of the image brightnesses), the inverse problem can be solved only using a specified model for the gravitational lens. The number of parameters characterizing the gravitational lens must correspond to the available observational data. Therefore, all subsequent calculations will be carried out in an Einstein–de Sitter model with cosmological parameters $\Omega = 1$, $\Lambda = 0$, and the Hubble constant $H = 75$ km s^{-1}Mpc^{-1}.

3.1. Quadrupole Lens Model

If only the apparent positions of components A and B are used in solving the inverse problem, there are only four knowns (the projections of $\mathbf{\Psi}_{\mathrm{A,\,B}}$ onto the axes of the specified coordinate system). Consequently, we must construct a gravitational-lens model involving four or fewer parameters if we wish to obtain a unique solution.

To consider the focusing of SBS 1520+530, we will use a Cartesian coordinate system whose origin coincides with the apparent center of brightness of the lensing galaxy, with the OX and OY axes directed along the corresponding Galactic axes (Fig. 5). The angular positions of the images will be specified by the polar coordinates $\mathbf{\Psi} = (\Psi, \varphi)$, where Ψ is the magnitude and φ is the azimuthal angle measured from the OX axis. For images observed far from the gravitating mass, the eikonal (6) can be conveniently represented as a series of zonal harmonics [15, 19]. As a result, neglecting an arbitrary constant, we obtain

$$L(\Psi, \varphi) = -\frac{2r_g}{D_d} \ln \frac{\Psi}{\Psi_0} + \sum_{m=1}^{\infty} \frac{A_m}{\Psi^m} \cos(m\varphi - \varphi_m). \tag{9}$$

Here, $r_g = 2GM/c^2$ is the gravitational radius of the lens, M is the total mass of the lensing galaxy, and φ_m and A_m are the expansion coefficients, which are determined by the specified mass distribution $\sigma(\Psi)$. The quantity Ψ_0 corresponds to an arbitrary (normalization) angle, which is usually chosen to be the angular radius of the Einstein ring corresponding to the total mass of the galaxy.

Let us assume that the observed brightness maximum for the gravitational lens coincides with its center of mass. In this case, the $m = 1$ term will be absent from the expansion (9). Further, since the terms of this series decrease quite rapidly with increasing distance from the center of the gravitational lens, we can take into consideration only the first nonzero term of the sum ($m = 2$). The first term of expansion (9) will then correspond to the pointlike component of the gravitational lens, and the second term to its quadrupole component (this model will be called a "quadrupole lens," L&Q). To simplify the modeling, we will further assume that the lensing galaxy G possesses elliptical symmetry with outer radius R and eccentricity e_c (Fig. 5). It is easy to prove that $\varphi_2 \equiv 0$ and $A_2 = r_g\rho_e^2/D_d^3$, where $\rho_e = Re_c$ [15]. The corresponding eikonal (9), deflection angle $\mathbf{\Theta}(\mathbf{\Psi}) = \nabla L(\mathbf{\Psi})$, and lens equation (4) can be written in the Cartesian coordinates $\mathbf{\Psi} = (\Psi_x, \Psi_y)$

$$L(\mathbf{\Psi}) = -\frac{2r_g}{D_d} \ln\left(\frac{\Psi}{\Psi_0}\right) + \frac{r_g\rho_e^2(\Psi_x^2 - \Psi_y^2)}{D_d^2\Psi^4}, \tag{10}$$

$$\begin{aligned} \mathbf{\Theta}(\mathbf{\Psi}) = &-\frac{2r_g\rho_e^2(\Psi_x^3 - 3\Psi_x\Psi_y^2)}{\Psi^6 D_d^3}\mathbf{e}_x \\ &- \frac{2r_g\rho_e^2(3\Psi_y\Psi_x^2 - \Psi_y^3)}{\Psi^6 D_d^3}\mathbf{e}_y, \end{aligned} \tag{11}$$

$$\begin{aligned} \Psi_{Sx} &= \Psi_x - \frac{\tilde{D}}{D_d}\left(\frac{2r_g\Psi_x}{\Psi^2 D_d} + \frac{2r_g\rho_e^2(\Psi_x^3 - 3\Psi_x\Psi_y^2)}{\Psi^6 D_d^3}\right), \\ \Psi_{Sy} &= \Psi_y - \frac{\tilde{D}}{D_d}\left(\frac{2r_g\Psi_y}{\Psi^2 D_d} + \frac{2r_g\rho_e^2(3\Psi_y\Psi_x^2 - \Psi_y^3)}{\Psi^6 D_d^3}\right). \end{aligned} \tag{12}$$

Here, $\Psi = \sqrt{\Psi_x^2 + \Psi_y^2}$, and $\mathbf{e}_x$ and $\mathbf{e}_y$ are the basis vectors of the Cartesian coordinate system.

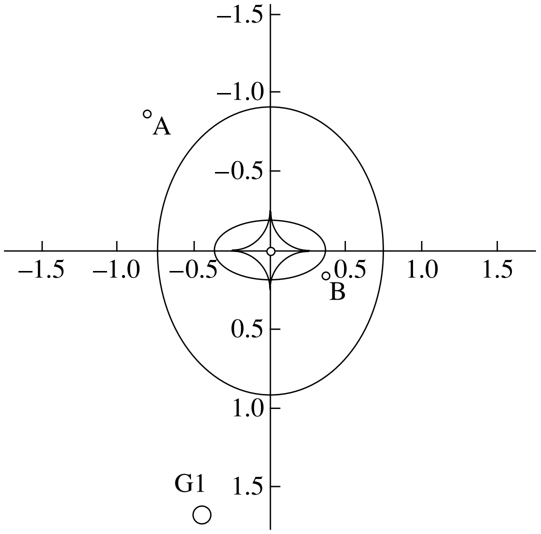

Fig. 5. Configuration of SBS 1520+530 in a coordinate system coincident with the lens symmetry axes. The large ellipse represents the critical curve, and the asteroid corresponds to a caustic in the lens plane.

Substituting the coordinates of images A and B from Table 4 into (12), we obtain four equations in four unknowns (r_g, ρ_e, Ψ_{Sx}, and Ψ_{Sy}), whose solution is presented in Table 5. Next, the obtained parameters of the lens can be used to estimate the signal delay between the images using (8) (Table 5).

3.2. Model with an Isothermal Sphere with Outer Shear

Along with the above model, we computed the parameters of another well-known model that has been widely used in studying gravitational lenses: an isothermal sphere with outer shear, SIS+γ. The corresponding lens equation in coordinates normalized to the angular radius of the Einstein ring, $\mathbf{v}_s = \mathbf{\Psi}_s/\Psi_0$ and $\mathbf{v} = \mathbf{\Psi}/\Psi_0$, has the form [17]

$$\mathbf{v}_s = \begin{pmatrix} 1 - \gamma\cos(2\varphi) & -\gamma\sin(2\varphi) \\ -\gamma\sin(2\varphi) & 1 + \gamma\cos(2\varphi) \end{pmatrix} \mathbf{v} + v^{\beta-1}\frac{\mathbf{v}}{v}. \tag{13}$$

When the exponent characterizing the power law of the mass distribution is $\beta = 1$, we obtain the equation for an isothermal sphere with outer shear (γ). To

Table 5. Parameters of the SBS 1520+530 system obtained from the modeling

Model	Mass of G, $10^{11} M_\odot$	ρ_c, γ	Ψ_{Sx}	Ψ_{Sy}	Δt, d
L&Q	1.57	$0.273''$	$-0.615''$	$-0.639''$	97
L&Q+G1	0.79	0.513	−0.434	−0.700	–
SIS+γ	2.15*	0.103	−0.343	−0.188	99

* Mass within the Einstein radius, equal to $0.815''$.

find the delay time, we use the formula derived in [20]:

$$\Delta t_{i,j} = \frac{\tilde{D}}{2c}(1+z_d)\{(v_j^2 - v_i^2) + \gamma[v_j^2 \cos 2\varphi_j - v_i^2 \cos 2\varphi_i]\}, \quad (14)$$

where v and φ are the polar coordinates of the components relative to the lens center. The results of these calculations are presented in Table 5.

4. CONCLUSION

High-resolution images obtained at the Maĭdanak Observatory and processed using modern methods have enabled us to detect the lensing galaxy in the SBS 1520+530 system and to determine its brightness in the R and I filters.

The observational data for 1998–2001 demonstrate variability of the brightnesses of components A and B with maximum amplitudes of 0.2^m and 0.25^m, respectively, on time scales of about a few months. In addition, significant (compared to the errors) variations in the brightnesses of the lensed components of the quasar (by about 0.04^m) were detected on time scales from a week to a month during monitoring carried out in 2000. The brightness variations of the components of SBS 1520+530 make this gravitationally lensed quasar a promising target for detailed monitoring aimed at determining the delay time Δt between the corresponding variations in the images, which can be used to estimate the Hubble constant.

The different models we have considered for the gravitational lens yield approximately the same mass estimates for the lensing galaxy, but there are some differences in the true position of the source. In principle, these models can be tested using the observed differences in the image brightnesses, which we have not yet utilized. As can easily be shown, this difference is determined by the relative amplification coefficient $q_{\rm A}/q_{\rm B}$. Unfortunately, the amplification coefficients $q_{\rm A}$ and $q_{\rm B}$ calculated using (7) yield ratios $q_{\rm A}/q_{\rm B}$ that differ appreciably from the observed values. This may be due both to inconsistencies in the chosen model and to factors that have not been taken into account, such as the influence of other galaxies in the vicinity of SBS 1520+530, absorption of the radiation of component B by the lensing galaxy, and microlensing. Including only the nearest galaxy G1 in the quadrupole-lens model affects the relative amplification coefficient very little. A relative amplification coefficient that is in agreement with the observed values can be achieved for an SIS+γ model with a mass for G1 of about 1.5 times the mass of G; however, such a model is not applicable to images located at considerable distances from the center of the gravitational lens, since the value of the shear does not decrease with increasing Ψ. In principle, the distribution of matter in the lensing galaxy can be changed by appropriate choice of the parameter β. The corresponding calculations show that the relative amplification coefficient $q_{\rm A}/q_{\rm B}$ is equal to the required value $\sim 0.7^m$ when $\beta \approx 1.4$.

Numerical modeling of the SBS 1520+530 system gives a value for Δt of about 100 days.

The model estimate of the mass of the lensing galaxy and the measured color index $R-H$ enable us to conclude that the lensing galaxy in the SBS 1520+530 system is spiral.

ACKNOWLEDGMENTS

We are grateful to Profs. A.A. Minakov, V.N. Dudinov, and S.N. Nuritdinov, as well as to the staff of the Department of Image Processing of the Institute of Astronomy of Kharkov State University, for their assistance, valuable advice, and comments during the course of our work.

REFERENCES

1. J. Wambsganss, *Gravitational Lensing in Astronomy* (Max-Planck-Institut, 1998).
2. V. N. Chavushyan, V. V. Vlasyuk, J. A. Stepanian, *et al.,* Astron. Astrophys. **318**, 60 (1997).
3. D. Crampton, P. L. Schechter, and J. L. Beuzit, Astron. J. **115**, 1383 (1998).
4. J. A. Muñoz, E. E. Falco, C. S. Kochanek, *et al., Proceedings of the III Scientific Meeting of the Spanish Astronomical Society,* Astrophys. Space Sci. (1999).
5. V. V. Vlasjuk and V. N. Chavushyan, Bull. Spec. Astrophys. Obs. **46**, 18 (1998).

6. Sh. Ehgamberdiev, A. Bayjumanov, S. Ilyasov, *et al.,* Astron. Astrophys., Suppl. Ser. **145**, 293 (2000).
7. V. Dudinov, P. Bliokch, B. Paczynski, *et al., Kinematics and Physics of Celestial Bodies,* Special Issue, 170 (2001).
8. A. U. Landolt, Astron. J. **88**, 439 (1983).
9. P. B. Stetson, Publ. Astron. Soc. Pac. **99**, 191 (1987).
10. H. K. C. Yee, Astron. J. **95,** 1331 (1988).
11. J. Krist and R. Hook, http://scivax.stsci.edu/∼krist/tinytim.html.
12. W. N. Colley and R. E. Schild, Astrophys. J. **540**, 104 (2000).
13. I. Burud, R. Stabell, P. Magain, *et al.*, Astron. Astrophys. **339**, 701 (1998).
14. R. K. Honecutt, Publ. Astron. Soc. Pac. **104**, 435 (1992).
15. P. V. Bliokh and A. A. Minakov, *Gravitational Lenses* [in Russian] (Naukova Dumka, Kiev, 1989).
16. A. F. Zakharov, *Gravitational Lenses and Microlenses* [in Russian] (Yanus-K, Moscow, 1997).
17. P. Schneider, J. Ehlers, and E. E. Falco, *Gravitational Lenses* (Springer, New York, 1992).
18. E. Falco, M. Gorenstein, and J. Shapiro, *IAU Symp. No. 129: The Impact of VLBI on Astrophysics and Geophysics* (Kluwer, Cambridge, 1987), p. 11.
19. J. Jackson, *Classical Electrodynamics* (New York, 1962; Mir, Moscow, 1965).
20. H. J. Witt, S. Mao, and C. R. Keeton, Astrophys. J. **544** (2003, in press).

Translated by Yu. Dumin

Astronomy Reports, Vol. 47, No. 9, 2003, pp. 728–732. Translated from Astronomicheskiĭ Zhurnal, Vol. 80, No. 9, 2003, pp. 792–797.
Original Russian Text Copyright © 2003 by Dolgachev, Domozhilova, Chernin.

The Zero-Acceleration Surface Around the Local Group of Galaxies

V. P. Dolgachev[1], L. M. Domozhilova[1], and A. D. Chernin[1,2]

[1]Sternberg Astronomical Institute, Universitetskiĭ pr. 13, Moscow, 119992 Russia
[2]Tuorla Observatory, University of Turku, Väisäläntie 20, FIN-21500 Piikkiö, Finland

Received May 15, 2002; in final form, March 14, 2003

Abstract—Recent observational data on the density of the cosmic vacuum are used to obtain an exact solution for the zero-acceleration surface around the Local Group of galaxies. This surface separates the inner region, in which the gravitation of the galaxies dominates, from the outer region, in which the antigravitation of the cosmic vacuum dominates. The zero-acceleration surface is close to a sphere of radius $\simeq 2$ Mpc. The size and shape of the surface have remained nearly constant during the lifetime of the Local Group as a distinct system of galaxies. © *2003 MAIK "Nauka/Interperiodica"*.

1. INTRODUCTION

Recent cosmological discoveries suggest that the vacuum dominates in the present-day Universe, with the energy density of the vacuum exceeding the total energy density of all "normal" forms of cosmic matter [1, 2] (see also the reviews [3–5]). The dynamics of the Universe are controlled by antigravity. The Universe is undergoing an accelerated expansion, while four-dimensional space–time becomes virtually static. It is important that this is a direct consequence of reliable observational data, rather than a theoretical prediction or hypothesis that remains to be tested.

It was believed previously that the entire history of the cosmological expansion consisted of a decelerating expansion after the initial push due to the Big Bang. However, it is now becoming clear that the dynamics of the expansion have changed from deceleration to a new stage of acceleration precisely at the current epoch. This possibility was originally suggested as a particular case in the cosmological theory of Friedmann. The theory also describes the subsequent stages of the cosmological expansion, when the vacuum dominates the dynamics. The formal prerequisite for this scenario is the presence of a nonzero Einstein cosmological constant in the general solution found by Friedmann; this constant can give rise to antigravity (or, more precisely, can represent it in the solution), which results in an acceleration of the expansion.

The discovery of the cosmic vacuum raises a number of new problems in cosmology, physics, and astronomy (see, e.g., [5, 6]). One is the dynamical role of the vacuum for our immediate neighborhood in the Universe, within a radius of 5–10 Mpc around the Local Group of galaxies. It was noted shortly after the discovery of the cosmic vacuum [7] that the vacuum dominates dynamically not only in the Universe as a whole, but also in an extended spherical layer around the Local Group. The inner radius of this layer is crudely estimated to be 3 Mpc, while the outer radius reaches 7–8 Mpc, which approximately corresponds to half the distance to the center of the Virgo cluster.

We report here the results of more accurate calculations of the dynamical background of the Local Group of galaxies, which is controlled by both the mass of the group itself and the cosmic vacuum; specifically, we compute the surface where the gravity of the Local Group is balanced by the antigravity of the cosmic vacuum (Section 3). We also present the required information on the cosmic vacuum and the Local Group of galaxies (Section 2) and briefly discuss the properties of the solution and its applicability to the physics of the nearby Universe (Section 4).

2. VACUUM AND THE LOCAL GROUP OF GALAXIES

Observational data [1, 2] indicate that the energy density of the vacuum exceeds the total density of all other forms of cosmic energy. The densities can be conveniently expressed in units of the critical density $\rho_c = \dfrac{3}{8\pi G}H^2 = (0.7 \pm 0.1) \times 10^{-29}$ g/cm^3, where $H = 65 \pm 15$ km/s/Mpc is the Hubble constant.

The density of the vacuum is

$$\Omega_V = \rho_V/\rho_c = 0.7 \pm 0.1. \qquad (1)$$

This value of the vacuum density was obtained from observations of high-redshift supernova and is verified by the entire collection of available data on the age of the Universe, the formation of large-scale structure in the Universe, and, especially, the anisotropy of the microwave background, together with data on the dynamics of rich clusters of galaxies [3, 4].

The density of hidden matter, often called dark matter in the literature, is only slightly lower than that of the vacuum and, averaged over the Universe, is

$$\Omega_D = \rho_D/\rho_c = 0.3 \pm 0.1. \tag{2}$$

The dark-matter density is followed by the baryonic density:

$$\Omega_B = \rho_B/\rho_c = 0.002 \pm 0.001. \tag{3}$$

Finally, the fourth component of the cosmological medium is radiation, or relativistic energy, with the density

$$\Omega_R = \rho_R/\rho_c = 0.6 \times 10^{-4}\alpha, \tag{4}$$

where the constant factor α ($1 < \alpha < 30$–100) takes into account the contribution of possible ultrarelativistic particles and fields, which is added to the contribution of the microwave background.

Recall that the vacuum has not only a certain energy density, but also a certain pressure. The relationship between the pressure and density, i.e., the equation of state, has the form $p_V = -\rho_V$ for the vacuum. (We use here the system of units in which $c = 1$.) Only this equation is compatible with the definition of the vacuum as an energy whose density is everywhere constant at all times. According to Friedmann theory, gravitation is produced by both the density and pressure of the medium, in the combination $\rho + 3p$. The vacuum produces antigravitation because its effective gravitating energy $\rho_G = \rho_V + 3p_V = -2\rho_V$ is negative.

(We note parenthetically that some investigators prefer to assume that the cosmological acceleration is produced by a presently unknown, completely hypothetical medium called quintessence, rather than by the vacuum. Quintessence is a special form of energy that obeys the equation of state $p = w\rho$, where w is a constant lying in the range $-1 < w < 1/3$ [9, 10]. It can readily be seen that the effective gravitational density is negative for this sort of energy. Thus, although quintessence is not vacuum, it can also produce antigravity and, therefore, acceleration of the cosmological expansion. The compatibility of this hypothesis with the entire collection of cosmological information is discussed in [11]. We will not consider the hypothesis of quintessence further here.)

The vacuum density is strictly constant, so that the vacuum is present everywhere and at all times without condensations or rarefactions, with exactly the same amount in any cubic centimeter of space. In particular, it is obviously present in the local volume of the Universe. In contrast, dark matter and baryons are distributed highly nonuniformly in the nearby Universe: within distances of 7–8 Mpc, the overwhelming majority of the nonvacuum mass is concentrated in the Local Group; this is essentially the total baryonic mass of our Galaxy and Andromeda, plus the energy of the extended, massive halos of these two galaxies, which is much larger (by a factor of 10–20). The total nonvacuum mass in the Local Group is $M_{LG} \simeq (1$–$3) \times 10^{12} M_\odot$ [12, 13] and is concentrated in a region about 1 Mpc in size. Within distances of 7–8 Mpc, other masses (as well as radiation) can be neglected.

To evaluate the dynamical situation on scales from 1 to 7–8 Mpc, we compare two quantities—the repulsive force produced by the vacuum at some distance R from the barycenter of the Local Group and the attractive force produced at the same distance by the total mass of the Local Group. The repulsion is

$$F_V = -GM_V/R^2 = (4\pi/3)G2\rho_V R. \tag{5}$$

Here, M_V is the total effective mass of the vacuum contained in a sphere of radius R, which is equal to the effective gravitating density of the vacuum multiplied by the volume of the sphere. This force is calculated here per unit mass, so that we are considering the acceleration.

To crudely estimate the attractive force produced by the mass of the Local Group, we neglect the departure of the mass distribution from spherical symmetry. In fact, the mass distribution corresponds to a barbell rather than a spherical shape, but, as we will see in Section 3, the difference in the two corresponding estimates is small for the distances we will obtain. In this first, spherical, approximation,

$$F_M = -GM_{LG}/R^2. \tag{6}$$

These two forces are equal in magnitude at $R \simeq 3$ Mpc; at larger distances, the antigravity of the vacuum dominates. This estimate is somewhat crude but is straightforward and basically trustworthy (see Section 3).

In the regular acceleration field at distances of 3–4 Mpc and more, we also expect to observe regular motions of test bodies, for which we can use low-mass galaxies within the local volume. This is indeed the case: the observed Hubble flow is highly regular starting from distances as small as 1.5–2 Mpc [14–16]. In the neighborhood of the Local Group, the galaxies partaking in the Hubble flow (mainly dwarf galaxies) move as test particles against the perfectly regular background of the vacuum.

3. THE ZERO-RADIAL-ACCELERATION SURFACE

We now accurately calculate the distances at which the gravity of the Local Group is balanced by the antigravity of the cosmic vacuum.

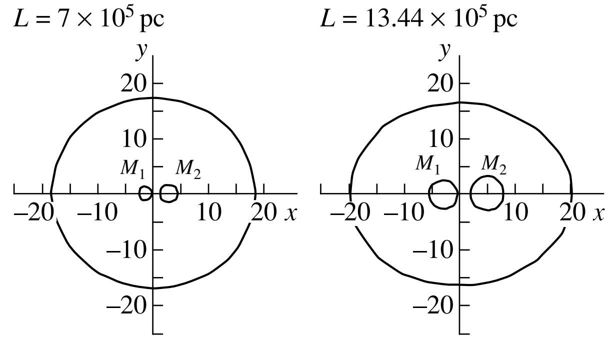

Intersection of the zero-radial-acceleration surfaces with the symmetry plane xOy. Distances along the axes are in units of 10^5 pc.

3.1. Equations of Motion. Properties of Motion

Let Oxy be a stationary barycentric Cartesian coordinate system. We consider the motion of a test body (dwarf galaxy) in the force field of the Local Group taking into account the potential of the vacuum. The pattern of the dynamics on the scale of the Local Group (1–10 Mpc) is described by two quantities—the repulsive force produced by the vacuum at some distance r from the center of the Local Group and the attractive force produced by the total mass of the Local Group at the same distance.

Let M_1 be the mass of galaxy M31, M_2 the mass of our Galaxy, and the repulsive force produced by the vacuum at a distance r from the center of mass of the Local Group be given by (5).

As usual, we write the Newtonian attractive forces due to the masses M_1 and M_2 in the form

$$F_i = G\frac{M_i}{{r_i}^2}, \qquad (i = 1, 2), \tag{7}$$

where $r_1^2 = (x - x_1)^2 + y^2$, $r_2^2 = (x - x_2)^2 + y^2$, x_1 and x_2 are the barycentric coordinates of the bodies M_1 and M_2, respectively, and G is the gravitational constant. Then, the force field of the Local Group $F(x, y)$ is

$$F(x, y) = G\left(\frac{M_1}{r_1^2} + \frac{M_2}{r_2^2} + \frac{8}{3}\pi\rho r\right). \tag{8}$$

This field has the force function

$$U(x, y) = G\left(\frac{M_1}{r_1} + \frac{M_2}{r_2} + \frac{4}{3}\pi\rho r^2\right). \tag{9}$$

The equations of motion of a dwarf galaxy in the gravitational field (8) are

$$\left.\begin{aligned} \frac{d^2x}{dt^2} &= \frac{\partial U}{\partial x} \\ \frac{d^2y}{dt^2} &= \frac{\partial U}{\partial y} \end{aligned}\right\}. \tag{10}$$

In the case $x_1, x_2 = \text{const}$, these equations have a first integral.

We multiply the first equation of (10) by $2\frac{dx}{dt}$, the second by $2\frac{dy}{dt}$, add them, and integrate to obtain the first integral of the system (10) in the form

$$V^2 = 2U + C, \tag{11}$$

where $V^2 = \left(\frac{dx}{dt}\right)^2 + \left(\frac{dy}{dt}\right)^2$, and C is the integration constant. The motion described by (10) is possible if $V^2 \geq 0$. Let us consider the family of curves compatible with the equation $2U + C = 0$. These curves are qualitatively similar to the Hill curves of the Jacobi integral for the restricted three-body problem with rotating axes [17]. However, we are dealing with a rectilinear, restricted three-body problem (the Galaxy and M31 move in a straight line) in a stationary barycentric coordinate system.

The analogue of the Hill curves has singular points (points where the curves are in contact) that can be determined by solving the system of equations

$$\left.\begin{aligned} \frac{\partial U}{\partial x} &= 0 \\ \frac{\partial U}{\partial y} &= 0 \end{aligned}\right\}. \tag{12}$$

Calculation of these partial derivatives yields expressions for the right-hand sides of (10). After some manipulation and cancellation of the factor G, system (12) becomes

$$\left.\begin{aligned} x\left(\tfrac{8}{3}\pi\rho - \tfrac{M_1}{r_1^3} - \tfrac{M_2}{r_2^3}\right) + \tfrac{M_1x_1}{r_1^3} + \tfrac{M_2x_2}{r_2^3} = 0 \\ y\left(\tfrac{8}{3}\pi\rho - \tfrac{M_1}{r_1^3} - \tfrac{M_2}{r_2^3}\right) = 0 \end{aligned}\right\}. \tag{13}$$

Solving this system of two nonlinear equations with two unknowns yields the coordinates $(x_i,\, y_i)$ of the points where the sum of the forces of the field considered is zero. Let us consider the second equation in (13), which is satisfied if

(a) $y = 0$ or

(b) $\frac{8}{3}\pi\rho - \frac{M_1}{r_1^3} - \frac{M_2}{r_2^3} = 0.$

Upon substituting $y = 0$ into the first equation of (13), we obtain a seventh-degree algebraic equation with three real roots. Thus, as in analyses of zero-relative-velocity curves (Hill curves) in the classical, restricted three-body problem, we have here three partial solutions for (13).

Substitution of expression (b) into the first equation of (13) yields

$$\frac{M_1x_1}{r_1^3} + \frac{M_2x_2}{r_2^3} = 0. \tag{14}$$

Since the barycentric coordinates x_1 and x_2 of the bodies M_1 and M_2 are coupled by the known relationship $x_1M_1 + x_2M_2 = 0$, equation (14) assumes the form

$$M_2x_2\left(\frac{1}{r_2^3} - \frac{1}{r_1^3}\right) = 0,$$

from which we find $r_1 = r_2$. To compute the numerical value of r_1, we substitute $r_2 = r_1$ into expression (b), obtaining

$$r_1 = \left(\frac{3}{8}\frac{M_1 + M_2}{\pi\rho}\right)^{1/3}. \tag{15}$$

Thus, we have an analogue of the known Laplacian triangular solutions.

Let us consider some numerical results for the Local Group. We take the mass of the Galaxy to be $M_2 = 10^{12}M_\odot$, the mass of M31 to be $M_1 = 1.5\ M_2$, and $\rho = 4 \times 10^{-30}$ g/cm^3. We then obtain $r_1 = r_2 = 1.77 \times 10^6$ pc, in accordance with (15). Since the distance between M_1 and M_2 is estimated to be $L = 7 \times 10^5$ pc, we have a Lagrangian triangular solution representing an isosceles triangle. The second triangular solution is the same isosceles triangle symmetric about the Ox axis.

To determine the boundaries of the regions in the Oxy plane with various dynamical properties of the motion, we obtain the equation for the zero-radial-acceleration curve in the field considered. In other words, we must obtain an equation for the locus of points where the dot product of the acceleration vector and the position vector of a test body is zero. If the coordinates of the acceleration vector are $\left\{\frac{d^2x}{dt^2}, \frac{d^2y}{dt^2}\right\}$ and the coordinates of the position vector are $\{x, y\}$, the dot product assumes the form

$$x\frac{d^2x}{dt^2} + y\frac{d^2y}{dt^2} = 0. \tag{16}$$

We note that the expressions for $\frac{d^2x}{dt^2}$ and $\frac{d^2y}{dt^2}$ in (16) are the right-hand sides of (10). Thus, the problem reduces to determining the roots of the equation

$$F(x, y) = x\frac{\partial U}{\partial x} + y\frac{\partial U}{\partial y} = 0 \tag{17}$$

using known numerical techniques.

Two families of curves obtained by numerically solving (17) are shown in the figure. The left-hand family was computed for the Local Group with the parameters of the system presented above and for the current epoch. The right-hand family was found using $L = 13.44 \times 10^5$ pc and $t = -12.5$ Gyr. These values were obtained as follows. Let us assume that the Galaxy and M31 are currently approaching each other at a velocity of 120 km/s and that $L = 7 \times 10^5$ pc. Then, solving the two-body problem, we find that these two bodies had zero relative velocity 12.5 Gyr ago, when the distance between M_1 and M_2 was 13.44×10^5 pc.

A numerical analysis of the behavior of the sign of the function $F(x, y)$ in the neighborhood of the curves shown in the figure indicates that, inside and outside the small ovals but inside the large ovals, the attraction produced by the masses M_1 and M_2 dominates over the repulsion produced by the vacuum. The situation is opposite outside the large ovals: the repulsion due to the vacuum dominates over the attraction due to the masses M_1 and M_2.

4. CONCLUSION

We can seen from the figure that the zero-radial-acceleration surface is appreciably non-spherical, especially at the initial state of the Local Group. The intersection of this surface with the symmetry plane (as in our figure) is represented by a slightly asymmetric oval that can lie between two circles, of radii 1.4 and 1.8 Mpc at the current epoch and of radii 2 and 1.7 Mpc at the initial epoch. Thus, the radial distances corresponding to this surface have never exceeded 2 Mpc.

The crude estimate in Section 2 yielded 3 Mpc instead of 2 Mpc. This difference is significant, especially in view of the substantially increased accuracy of the most recent observational studies of the kinematics of galaxies around the Local Group [14–16]; for example, the accuracy of distance determinations within 3 Mpc reaches 7% (see, e.g., [15], where data of the Special Astrophysical Observatory's 6-m telescope and the HST were used). If distances are determined with such high accuracies, theoretical models describing the pattern of the dynamics with accuracies worse than 30% (as in our tentative estimate) are no longer acceptable. It is this circumstance that prompted us to find an accurate solution for the zero-acceleration surface in the nearby Universe.

It is striking that the characteristic surface of the Local Group has not changed significantly over more than 12 Myr of evolution. Our solution has enabled us to identify and quantitatively estimate this almost perfectly static behavior (see above). This result, together with that fact that the cosmic vacuum is ideally static, implies that the dynamical background against which the observationally studied kinematics have developed in the vicinity of the Local Group has undergone virtually no changes during the entire lifetime of the Local Group (i.e., three-quarters of the lifetime of the Universe). It may be this stability of the Local-Group dynamics that leads to the observed (enigmatic, according to Sandage [14]) regularity in the kinematics of the local Hubble flow.

To avoid confusion, recall that no cosmological expansion has occurred for the past 12 Myr or is occurring presently within the volume of the Local Group. On the contrary, our Galaxy and the Andromeda galaxy have been moving toward each other since the time of formation of the Local Group (12 Myr ago). Such systems (as well as compact groups and galactic clusters in general) formed and became distinct from the cosmological expansion at redshifts of $z = 3$–10, i.e., long before the epoch of predominance of the vacuum, which began at $z = 0.7$. There could be no other possibilities, since the predominance of the vacuum with its antigravity quenches the development of cosmological perturbations (see, e.g., the exact solution [23], which describes the cessation of the growth of perturbations in the standard cosmological model in the presence of a dominating vacuum).

The system of equations (10) describing the motion of a test body in the Local Group has five partial solutions, three of which are aligned with the Ox axis; the other two (by analogy with the so-called triangular solutions) are situated in the yOz plane along a circle whose radius is equal to the height of the isosceles triangle mentioned in Section 3.

At these five singular points, $\frac{\partial U}{\partial x} = \frac{\partial U}{\partial y} = 0$; i.e., the sum of the field forces acting on the test body is zero, so that condensations of intergalactic matter can be present near these points.

The questions considered in this paper are also touched upon, in one form or another, in [18–20].

The problem of the zero-acceleration surface is closely related to some classical problems of celestial mechanics (Section 3), although classical problems have never dealt with the vacuum (to say nothing of an antigravitational vacuum). The consideration of an antigravitational vacuum substantially enriches the situation, adding qualitatively new elements. A zero-acceleration surface separating regions of gravity and antigravity is now appearing in such problems, and probably in astronomy in general, for the first time. Its existence imparts a number of new features to dynamical models of the near Universe, which require multifaceted studies, such as investigations of the dynamical instability of the motions of test bodies (dwarf galaxies, clouds of intergalactic gas). This instability is present even without the vacuum [21, 22], but its development should be especially interesting near the zero-acceleration surface. This complex problem requires separate, detailed studies.

REFERENCES

1. A. G. Riess, A. V. Filippenko, P. Challis, *et al.,* Astron. J. **116**, 1009 (1998).
2. S. Perlmutter, G. Aldering, G. Goldhaber, *et al.,* Astrophys. J. **517**, 565 (1999).
3. S.Carol, astro-ph/0004075 (2000).
4. L. Wang, R. R. Caldwell, J. P. Ostriker, and P. J. Steinhardt, Astrophys. J. **530**, 17 (2000).
5. A. D. Chernin, Usp. Fiz. Nauk **171**, 1153 (2001).
6. V. L. Ginzburg, Usp. Fiz. Nauk **172**, 213 (2002).
7. A. D. Chernin, P. Teerikorpi, and Yu. V. Baryshev, astro-ph/0011528.
8. Yu. V. Baryshev, A. D. Chernin, and P. Teerikorpi, Astron. Astrophys. **378**, 729 (2001).
9. R. R. Caldwell and P. J. Steinhardt, Phys. Rev. D **57**, 6057 (1998).
10. S. Weinberg, astro-ph/0005265.
11. V. Sahni and A. Starobinsky, Int. J. Theor. Phys. **9**, 373 (2000).
12. P. J. E. Peebles, *Principles of Physical Cosmology* (Princeton Univ., Princeton, 1993).
13. P. Teerikorpi, M. Hanski, G. Theureau, *et al.,* Astron. Astrophys. **334**, 395 (1998).
14. A. Sandage, Astrophys. J. **527**, 479 (1999).
15. I. D. Karachentsev, Usp. Fiz. Nauk **171**, 860 (2001).
16. I. D. Karachentsev and D. I. Makarov, Astrofizika **44**, 5 (2001).
17. V. Szebehely, *Theory of Orbits. The Restricted Problem of Three Bodies* (Academic, New York, 1967; Nauka, Moscow, 1982).
18. F. A. Tsitsin, Astron. Tsirk. **878**, 3 (1975).
19. V. V. Radzievskiĭ, Astron. Zh. **31**, 436 (1954).
20. V. V. Radzievskiĭ, Probl. Issled. Vselennoĭ **7**, 418 (1978).
21. V. P. Dolgachev, Astron. Zh. **74**, 315 (1997) [Astron. Rep. **41**, 274 (1997)].
22. V. P. Dolgachev, E. P. Kalinina, and A. D. Chernin, Astron. Astrophys. Trans. **15**, 31 (1998).
23. A. D. Chernin, D. I. Nagirner, and S. V. Starikova, Astron. Astrophys. **19**, 399 (2003).

Translated by A. Getling

Astronomy Reports, Vol. 47, No. 9, 2003, pp. 733–739. Translated from Astronomicheskiĭ Zhurnal, Vol. 80, No. 9, 2003, pp. 798–804.

Influence of Accretion-Disk Models on the Structure of the Iron K_α Line

A. F. Zakharov[1,2,3] **and S. V. Repin**[4]

[1] *National Observatory of the Chinese Academy of Sciences, Beijing, China*
[2] *Institute for Theoretical and Experimental Physics, Moscow, Russia*
[3] *Astro Space Center, Lebedev Physical Institute, Moscow, Russia*
[4] *Space Research Institute, Moscow, Russia*

Received January 30, 2003; in final form, March 14, 2003

Abstract—Broad iron K_α emission with a characteristic two-peaked profile is observed in most Seyfert galaxies in the X-ray. We have calculated the profiles of such lines emitted by an accretion disk in a Schwartzschild metric. The dependence of the temperature distribution in the disk on the line shape is demonstrated. All the calculations include general relativistic effects. The disk material is assumed to move in circular geodesics in the equatorial plane. The line profile is extremely complex, even in a traditional model for the radial temperature distribution, complicating interpretation of the observational data. © *2003 MAIK "Nauka/Interperiodica"*.

1. INTRODUCTION

A number of space projects enabling the acquisition of X-ray spectra of the nuclei of Seyfert galaxies have been realized in recent years. Such projects include ASCA, RXTE, Chandra, Newton, and others.

The spectra of most Seyfert galaxies display broad iron K_α ($\sim$6.4 keV) emission [1–8] and weaker lines of other elements at 1–4 keV. In observations with good spectral resolution, the K_α line has a characteristic two-peaked profile [2, 9] with a well defined, high "blue" peak, a much weaker "red" peak, and a long red tail that gradually drops to the background level. Unfortunately, lines of other elements are too weak to reliably measure their profiles. In many cases, the Doppler width of the iron K_α line corresponds to velocities of tens of thousands of kilometers per second. The maximum measured velocity, $v \approx 80\,000–100\,000$ km/s [2], was found for the galaxy MCG-6-30-15, for which the line profiles are also relatively well defined. The velocity $v \approx 48\,000$ km/s has been obtained for MCG-5-23-17 [10]. The typical velocities for a number of other galaxies are $v \approx 15\,000–25\,000$ km/s. Rapid variations of the K_α profile of NGC 7314 have been detected [11], as well as strong X-ray variability [12, 13], quasi-periodic oscillations in GRC 1915+105 [14], and other manifestations of nonstationarity.

Such high velocities can probably occur only in jets or in the inner regions of an accretion disk. This makes it natural to suppose that this is the region where the K_α line is emitted. Additional support for this hypothesis is provided by estimates of the temperature of the disk in this region. In the traditional model of Shakura and Sunyaev [15] (see also [16–18]), the temperature of the inner disk is $T \sim 10^7–10^8$ K, which corresponds to the total ionization of iron and excitation of the K_α line. Modeling the processes occurring in such strong gravitational fields not only provides opportunities for testing general-relativity theory but also enables studies of various manifestations of the extreme conditions encountered there, such as the formation of jets [19, 20], lensing, and the emission of gravitational radiation.

Numerical modeling of various observational properties associated with the shape of the K_α taking into account general-relativistic effects have been carried out, for example, in [21–27]. MHD modeling of nonstationary processes in accretion disks was performed in [28].

In the current paper, we use an approach based on numerical modeling of the motion of photons radiated by an individual hot spot moving along a circular geodesic in the equatorial plane. The disk spectrum is obtained by integrating over the radius, taking into account the model dependence of the temperature on the radius. This method was used earlier to model the spectra and variability of hot spots in an accretion disk including the effects of general relativity [29–34]. This approach was also used in [35] to investigate the possibility of estimating the magnetic-field strength based on an analysis of features in the blue peak of the iron K_α line.

1063-7729/03/4709-0733$24.00 © 2003 MAIK "Nauka/Interperiodica"

2. EQUATIONS OF MOTION

Stationary black holes are described by a Kerr metric, which in geometric units ($G = c = 1$) and Boyer–Lindquist coordinates (t, r, θ, ϕ) has the form [36, 37]

$$ds^2 = -\frac{\Delta}{\rho^2}\left(dt - a\sin^2\theta d\phi\right)^2 + \frac{\sin^2\theta}{\rho^2} \tag{1}$$

$$\times\left[\left(r^2+a^2\right)d\phi - adt\right]^2 + \frac{\rho^2}{\Delta}dr^2 + \rho^2 d\theta^2,$$

where

$$\rho^2 = r^2 + a^2\cos^2\theta, \quad \Delta = r^2 - 2Mr + a^2,$$

the constants M and a determine the mass, and $a = S/M$ is the specific angular momentum of the black hole.

The equations of motion of a particle in a Kerr field can be obtained in accordance with [38] (and [36, 37]) via separation of variables in the Hamilton–Jacobi equation

$$g^{ik}\frac{\partial S}{\partial x^i}\frac{\partial S}{\partial x^k} - m^2 = 0.$$

As is shown in [30, 32], in this case, the equations of motion of a photon ($m = 0$) reduce to a system of six ordinary, first-order, differential equations with no singularities. In dimensionless variables, this system of equations has the form

$$\frac{dt'}{d\sigma} = -\hat{a}\left(\hat{a}\sin^2\theta - \xi\right) + \frac{\hat{r}^2+\hat{a}^2}{\hat{\Delta}}\left(\hat{r}^2+\hat{a}^2-\xi\hat{a}\right), \tag{2}$$

$$\frac{d\hat{r}}{d\sigma} = r_1, \tag{3}$$

$$\frac{dr_1}{d\sigma} = 2\hat{r}^3 + \left(\hat{a}^2 - \xi^2 - \eta\right)\hat{r} + (\hat{a}-\xi)^2 + \eta, \tag{4}$$

$$\frac{d\theta}{d\sigma} = \theta_1, \tag{5}$$

$$\frac{d\theta_1}{d\sigma} = \cos\theta\left(\frac{\xi^2}{\sin^3\theta} - \hat{a}^2\sin\theta\right), \tag{6}$$

$$\frac{d\phi}{d\sigma} = -\left(\hat{a} - \frac{\xi}{\sin^2\theta}\right) + \frac{\hat{a}}{\hat{\Delta}}\left(\hat{r}^2+\hat{a}^2-\xi\hat{a}\right), \tag{7}$$

where

$$\epsilon_1 \equiv r_1^2 - \hat{r}^4 - \left(\hat{a}^2-\xi^2-\eta\right)\hat{r}^2 \tag{8}$$

$$-2\left[(\hat{a}-\xi)^2+\eta\right]\hat{r} + \hat{a}^2\eta = 0,$$

$$\epsilon_2 \equiv \theta_1^2 - \eta - \cos^2\theta\left(\hat{a}^2 - \frac{\xi^2}{\sin^2\theta}\right) = 0, \tag{9}$$

are first integrals and $\eta = Q/M^2E^2$ and $\xi = L_z/ME$ are the Chandrasekhar constants [39]. This reduced system does not have any singularities, in contrast to the traditional means of writing the equations of motion [36, 37] in the form of four equations, one for each coordinate.

The equation of motion of photons in a centrally symmetric Schwartzschild metric,

$$ds^2 = \left(1-\frac{r_g}{r}\right)dt^2 - r^2\left(\sin^2\theta d\phi^2 + d\theta^2\right) \tag{10}$$

$$-\left(1-\frac{r_g}{r}\right)^{-1}dr^2,$$

can be obtained in quadratures in the same way [37]; however, in the interest of generality, it is much simpler to solve the system of equations (2)–(7) in this case as well, setting a equal to some small quantity, for example, $a = 0.01$. From the point of view of a distant observer, this field will be virtually indistinguishable from a Schwartzschild field. Of course, a rigorous proof of this statement would require computation of the components of the curvature tensor R_{iklm} in order to show that they differ only slightly for the cases $a = 0$ and $a = 0.01$ when $r > 3r_g$. However, this result is evident *a priori*, since the components of the Kerr metric become equal to the components of the Schwartzschild metric when $a \to 0$.

The qualitative analysis carried out in [40, 41] shows that the type of motion of photons (whether they are captured or scattered in the near vicinity of the black hole) can change fundamentally in the presence of fairly small variations in the initial data. In the same way, in such cases, the standard approach of analyzing geodesics by computing elliptical integrals can lead to large numerical errors, especially near singular points of the integral. The results of numerical integration of such geodesics in a Kerr metric and their very complex appearance in the vicinity of the horizon are presented in [42].

Solving the system (2)–(7) for photons radiated by a hot spot moving along a geodesic in the equatorial plane, we can obtain the spectrum of the spot that will be observed by a distant observer as a function of his position, i.e., for various values of the angle θ. It is convenient to carry out the numerical integration using a combination of the methods of Gear [43] and Adams, which are realized in [44–46]. The disk spectrum is obtained by integrating over the radial coordinate.

3. MODEL FOR THE DISK RADIATION

We must adopt some model for the disk if we wish to model the spectra. We will suppose that the disk lies in the equatorial plane of a Kerr black hole. However, we will assume that we are dealing with a metric that differs only slightly from a Schwartzschild metric when $a = 0.01$. In particular, the marginally stable orbit lies at $r_{ms} = 2.9836r_g$, which differs only slightly from $3r_g$. We will also assume that the disk has no physical thickness, i.e., that it is infinitely thin. In addition, we will assume that the disk is optically thick, which should correctly reflect the physics of the situation, since, in this case, a distant observer located on one side of the disk cannot detect photons radiated by its opposite surface.

To simplify the computations, we will take the spectral line under study to be monochromatic in its own locally inertial rest frame. This is justified by the fact that, even when $T = 10^8$ K, the relative Doppler width of the line,

$$\frac{\delta f}{f} \sim \frac{v}{c} \sim \frac{1}{c}\sqrt{\frac{kT}{m_{\mathrm{Fe}}}} \approx 10^{-3},$$

is much smaller than the characteristic observed line widths.

We will determine the dependence of the disk temperature on the radial coordinate from the standard α-disk model of Shakura and Sunyaev [15], which is also considered in [16, 18]. The intensity of the radiation is proportional to T^4 as usual.

In the Schwartzschild metric, the surface area of a radiating ring with width dr differs from the classical expression $dS = 2\pi r dr$, which must be replaced by [33]

$$dS = \frac{2\pi r dr}{\sqrt{1 - \frac{r_g}{r}}}. \tag{11}$$

The intensity of the radiation at a radius r is proportional to the area of this ring.

Thus, the total number of photons radiated by the disk in a line at frequencies from ν to $\nu + d\nu$ is proportional to the integral

$$I_\nu = \int\limits_{r_{in}}^{r_{out}} I_\nu(r)\,[T(r)]^4\,dS, \tag{12}$$

where $I(r)$ is obtained from the solution of (2)–(7), $T(r)$ from the corresponding dependence for an α disk, and dS from (11).

As is known, an α disk consists of three regions, with the innermost and middle regions dominated by radiation and gas pressure, respectively. The boundary between these regions r_{ab} is derived from the equation

$$\frac{r_{ab}/(3r_g)}{\left(1 - \sqrt{3r_g/r_{ab}}\right)^{16/21}} = 150\,(\alpha m)^{2/21}\dot{m}^{16/21}, \tag{13}$$

which is usually solved iteratively. In (13), $m = M/M_\odot$ and $\dot{m} = \dot{M}/\dot{M}_{cr}$ (where $\dot{M}_{cr} = 3 \times 10^{-8}(M/M_\odot)M_\odot/\mathrm{yr}$). For example, for $\alpha = 0.2$, $m = 10^8$, and $\dot{m} = 0.1$, we obtain from (13) $r_{ab} \approx 360r_g$. In our modeling, we will take the radiating region to lie entirely in the innermost region of the α disk (in so-called zone a). If this is not the case, the line profile becomes very complex, and it is difficult to avoid ambiguity in the interpretation of the results. Therefore, we will assume that the line radiation arises at radii from $r_{out} = 10r_g$ to $r_{in} = 3r_g$ and that this radiation is monochromatic in its own locally inertial rest frame. We will arbitrarily take the frequency of the radiation to be unity. The inner boundary of the radiating region corresponds to the last stable orbit in the Schwartzschild metric, which has been replaced in the equations for the Kerr metric with the value $a = 0.01$ in the interest of generality.

4. MODELING RESULTS

Figure 1 shows the modeling results for $\alpha = 0.2$, $m = 10^8$, $\dot{m} = 0.1$ in the form of the line profile as a function of the location of a distant observer. Figure 2 shows the dependence of the line profile on the position of the outer boundary of the radiating region.

We can see from Fig. 1 that the dependence of the line profile on the location of the observer is very complex. For example, the line has one maximum and a quite smooth profile when $0° < \theta < 23°$. The line acquires a second maximum when $\theta \approx 25°$, but there is no hope of detecting this second maximum. The classical line profile with two maxima first appears when $\theta \approx 30°$; however, at such angles, the ratio of the heights of the two maxima is close to unity. The blue peak is quite broad, and its center is slightly shifted toward lower frequencies from the laboratory frequency, $\nu = 0.95\nu_{lab}$. The width of the red maximum is difficult to estimate, since it is less well defined. As the angle of the line of sight is further increased, the line acquires the classical shape with two maxima with different heights. The height ratio of the maxima already exceeds two at $\theta = 40°$, and the blue peak is becoming narrower. It is interesting that, at this viewing angle, the frequency of the blue maximum is slightly higher than the laboratory frequency, $\nu = 1.07\nu_{lab}$. A precise coincidence in frequency, $\nu = \nu_{lab}$, is achieved when $\theta = 33°$. If the angle is further increased, the height ratio of the maxima reaches its largest value of about 4.5 when $\theta \approx 50°$, after which it decreases only slightly. The blue maximum itself becomes extremely narrow, and its shape resembles the spectrum of a rotating hot spot [32] more than the spectrum of an accretion disk. This is not true, however, for the red maximum. The peak in the spectrum is at a frequency slightly higher than the laboratory frequency, $1.13\nu_{lab}$). When $\theta = 60°$, the blue maximum again begins to broaden, and its position shifts even further toward higher energies. As the angle is

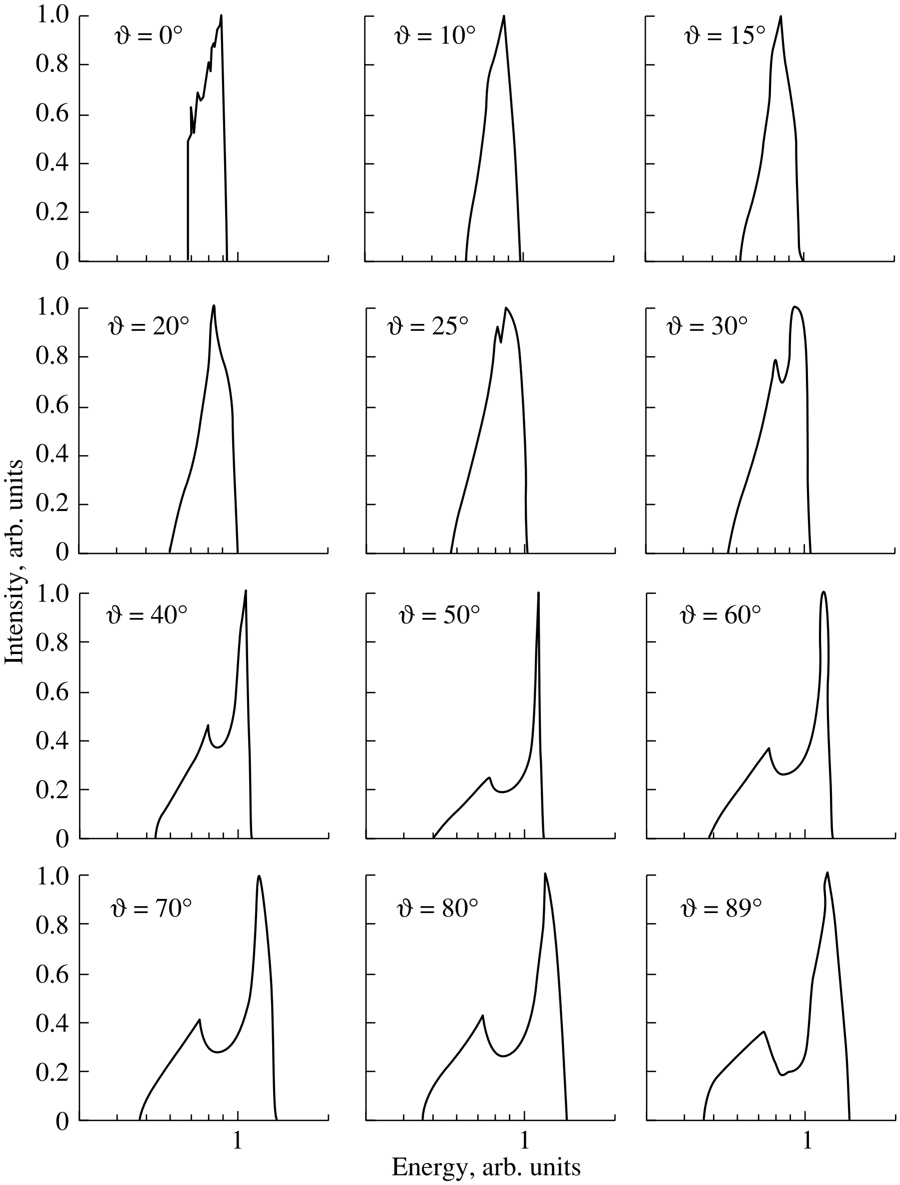

Fig. 1. Observed line spectrum radiated by an α accretion disk in the region $r = (3–10)r_g$ in the centrally symmetric field of a black hole for various locations of a distant observer. The reduced smoothness of the spectrum at $\theta = 0°$ (relatively few photons emerge near the polar axis) and $\theta \geq 80°$ has a purely statistical nature, and is not associated with real physical effects.

increased even further, beginning with $\theta \approx 70°$, the blue maximum acquires a characteristic asymmetric shape in which the right-hand (high-frequency) side falls off appreciably more slowly than the left-hand (low-frequency) side.

We can also see that, as the angle θ is increased, the ratio of the intensity of the red maximum to the intensity between the maxima increases. This ratio is close to unity when $\theta = 30°$ and grows to 1.6 when $\theta = 80°$.

Note also that additional features appear in the spectrum when $\theta > 85°$, which seem at first to be purely statistical but are in fact associated with physical effects. We will not analyze the origin of these effects here, since the probability of viewing a disk at such a large angle is very small.

Figure 2 shows the dependence of the spectrum on the width of the radiating region for $\theta = 30°$, $r_{in} = 3r_g$ (and one panel in Fig. 1 for $r_{out} = 10r_g$). The sequence of spectra shows how the profile shape changes as the outer boundary of the radiating region is varied. We can see that the line width remains nearly constant, since it is determined primarily by inner regions of the disk, which are always present and are most strongly subject to the

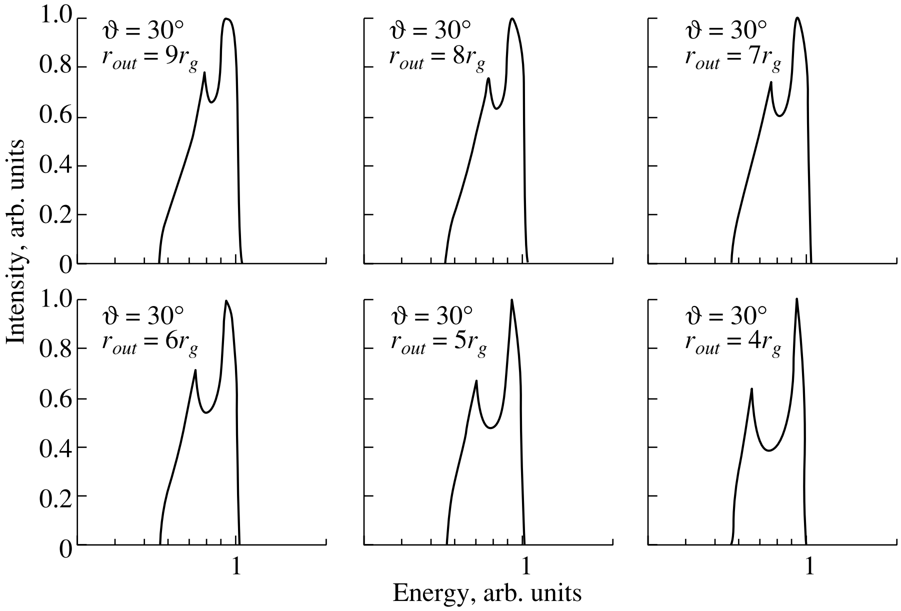

Fig. 2. Line spectrum radiated by an α accretion disk in the centrally symmetric field of a black hole for $\theta = 30°$, $r_{in} = 3r_g$ and various values of r_{out}. The line profile is as it would be seen by a distant observer.

Doppler effect. The wider the radiating region, the less clearly the line separates into two maximum, and the closer the maxima approach each other. The position of the blue maximum remains nearly constant, shifting only slightly from $\nu = 0.95\nu_{lab}$ for $r_{out} = 10r_g$ to $\nu = 0.93\nu_{lab}$ for $r_{out} = 4r_g$. The position of the red maximum varies much more strongly: from $\nu = 0.66\nu_{lab}$ for $r_{out} = 10r_g$ to $\nu = 0.82\nu_{lab}$ for $r_{out} = 4r_g$. The situation is opposite for the shapes of the peaks: the red maximum remains narrow, while the shape of the blue maximum changes, becoming very smoothed when the radiating region is wide. The depth of the minimum between the peaks is likewise variable, and the minimum itself becomes less distinct when the radiating region is wide. For example, the ratio of the intensity of the blue maximum to that of the minimum is 0.69 when $r_{out} = 10r_g$ but has decreased to 0.38 when $r_{out} = 4r_g$. The ratio of the intensities of the red and blue maxima for these same values of r_{out} are 0.78 and 0.63, respectively.

5. DISCUSSION

The results presented in Figs. 1 and 2 represent the combination of several effects, each of which is difficult to study analytically.

First, the disk temperature increases as the radius decreases, and the radiation grows as T^4. Second, the surface area of a radiating ring with width dr decreases in accordance with (11), but the first effect dominates right up to the marginally stable orbit in the Schwartzschild field. In addition, the radiation of each ring experiences a gravitational redshift, and the frequencies of both maxima depend on the inclination of the disk to the line of sight to the observer. When superimposed, these effects can produce both broad lines and features that could be interpreted as narrow spectral lines. For example, the blue maximum is broad when $\theta = 30°$, but narrow when $\theta = 50°$. In the latter case, all the various effects are superimposed in such a way that each narrow ring radiates its blue maximum at approximately the same frequency, with regions with smaller radii being brighter and making the largest contribution to the overall intensity. In the case of the red maximum, the Doppler effect and the gravitational redshift act in the same sense, so that this peak becomes very broadened. This broadening is also affected by the fact that the red maxima for rings in inner regions of the disk are poorly defined and resemble a slowly diminishing wing more than a maximum as such.

This should increase the intensity at low energies but should not lead to the appearance of a high maximum in the red part of the line. When $\theta = 50°$, the maximum radiation in the blue peak occurs at $\nu = 1.13\nu_{lab}$, while the photon with the highest energy has frequency $\nu < 1.15\nu_{lab}$. The situation for the red maximum is completely different: the maximum radiation occurs at $\nu_1 = 0.77\nu_{lab}$, while the photon with the lowest energy has $\nu_2 = 0.51\nu_{lab}$ ($\nu_1/\nu_2 = 1.51$). In addition, the red maximum is very poorly defined. Using a normalization in which the height of the blue maximum is equal to unity, the height of the red maximum is 0.25, and the minimum intensity between the two maxima is 0.18. This type of line profile is difficult to detect observationally, since the unavoidable presence of the continuum hinders detailed studies of the line profile near the red maximum. This type of profile would likely be erroneously be interpreted as a narrow Fe K_α line shifted toward the blue, while the indistinct, weak red maximum at a frequency a factor of 1.5 lower would go undetected.

Given the modest spectral accuracy of modern X-ray observations, it would seem that observations of the K_α line in Seyfert galaxies with $\theta \approx 50^\circ$ would be the most promising. However, this is not the case, since modern models of Seyfert galaxies suppose the presence of a dusty torus that blocks radiation emitted at large angles θ. It is more likely that we would detect radiation emitted at $\theta < 40^\circ$, where the blue peak is broader, and, consequently, less bright. Indeed, most observations of Seyfert galaxies suggest angles θ close to 30°.

The above considerations are fairly general, and can be used to infer observational manifestations of black holes with various masses. We note here that there does exist the possibility of observing the disk radiation emitted at large values of θ, but in binary systems rather than Seyfert galaxies. The dusty torus that feeds the disk in a Seyfert galaxy is absent in this case, and material arrives at the disk through the only Lagrange point. Therefore, it is possible for an external observer to view the accretion disk edge-on or at a fairly large angle θ. In this case, the compact component is situated closer to the observer than the giant star feeding the disk. In this configuration, in spite of the complex character of the flow of material, we have the opportunity to observe radiation from the accretion disk emitted at $\theta > 70^\circ$, when the blue maximum acquires its characteristic asymmetric shape, which should be detectable in observations with sufficiently good spectral resolution.

6. ACKNOWLEDGMENTS

One of the authors (AFZ) thanks E.F. Zakharova for attention and support that were necessary for this work. This research was supported by the National Science Foundation of China (grant 10233050). SVR thanks Prof. E.V. Starostenko, Dr. A.M. Salpagarov, Dr. O.N. Sumenkova, and L.V. Bankalyuk for the opportunity to work intensively on this problem. This work was also supported by the Russian Foundation for Basic Research (project code 00-02-16108).

REFERENCES

1. A. C. Fabian, K. Nandra, C. S. Reynolds, *et al.*, Mon. Not. R. Astron. Soc. **277**, L11 (1995).
2. Y. Tanaka, K. Nandra, A. C. Fabian, *et al.*, Nature **375**, 659 (1995).
3. K. Nandra, I. M. George, R. F. Mushotzky, *et al.*, Astrophys. J. **476**, 70 (1997).
4. K. Nandra, I. M. George, R. F. Mushotzky, *et al.*, Astrophys. J. **477**, 602 (1997).
5. A. Malizia, L. Bassani, J. B. Stephen, *et al.*, Astrophys. J., Suppl. Ser. **113**, 311 (1997).
6. R. M. Sambruna, I. M. George, R. F. Mushotsky, *et al.*, Astrophys. J. **495**, 749 (1998).
7. T. Yaqoob, I. M. George, K. Nandra, *et al.*, Astrophys. J. **546**, 759 (2001).
8. P. M. Ogle, H. L. Marshall, J. C. Lee, *et al.*, Astrophys. J. **545**, L81 (2000).
9. T. Yaqoob, B. McKernan, A. Ptak, *et al.*, Astrophys. J. **490**, L25 (1997).
10. K. A. Weawer, J. H. Krolik, and E. A. Pier, Astrophys. J. **498**, 213 (1998); astro-ph/9712035.
11. T. Yaqoob, P. J. Serlemitsos, T. J. Turner, *et al.*, Astrophys. J. **470**, L27 (1996).
12. J. W. Sulentic, P. Marziani, and M. Calvani, Astrophys. J. **497**, L65 (1998).
13. J. X. Wang, Y. Y. Zhou, H. G. Xu, *et al.*, Astrophys. J. **516**, L65 (1999).
14. B. Paul, P. C. Agrawal, A. R. Rao, *et al.*, Astrophys. J. **492**, L63 (1998).
15. N. I. Shakura and R. A. Sunyaev, Astron. Astrophys. **24**, 337 (1973).
16. N. I. Shakura, Astron. Zh. **49**, 921 (1972) [Sov. Astron. **16**, 756 (1972)].
17. I. D. Novikov and K. S. Thorne, in *Black Holes*, Eds. by C. De Witt and B. S. De Witt (Gordon & Breach, New York, 1973), p. 334.
18. G. V. Lipunova and N. I. Shakura, Astron. Rep. **46**, 366 (2002).
19. R. V. E. Lovelace, W. I. Newman, and M. M. Romanova, Astrophys. J. **484**, 628 (1997).
20. M. M. Romanova, G. V. Ustyugova, A. V. Koldoba, *et al.*, Astrophys. J. **500**, 703 (1998).
21. J. W. Sulentic, P. Marziani, T. Zwitter, *et al.*, Astrophys. J. **501**, 54 (1998).
22. G. Matt, G. C. Perova, L. Piro, and L. Stella, Astron. Astrophys. **257**, 63 (1992).
23. B. C. Bromley, K. Chen, and W. A. Miller, Astrophys. J. **475**, 57 (1997).
24. W. Cui, S. N. Zhang, and W. Chen, Astrophys. J. **492**, L53 (1998).
25. V. I. Pariev and B. C. Bromley, in *Proceedings of the 8th Annual October Astrophysics Conference in Maryland* (1997); astro-ph/9711214.
26. V. I. Pariev and B. C. Bromley, Astrophys. J. **508**, 590 (1998).
27. B. C. Bromley, W. A. Miller, and V. I. Pariev, Nature **391**, 54 (1998).
28. R. Keppens, F. Casse, and J. P. Goedbloed, Astrophys. J. **569**, L121 (2002).
29. A. F. Zakharov, Preprint MPA No. 755 (1993).
30. A. F. Zakharov, Mon. Not. R. Astron. Soc. **269**, 283 (1994).

31. A. F. Zakharov, in *17th Texas Symposium on Relativistic Astropysics, Annals of the The New York Academy of Sciences* **759**, 550 (1995).
32. A. F. Zakharov and S. V. Repin, Astron. Zh. **76**, 803 (1999) [Astron. Rep. **43**, 705 (1999)].
33. A. F. Zakharov and S. V. Repin, Astron. Rep. **46**, 360 (2002).
34. A. F. Zakharov and S. V. Repin, Adv. Space Res. (2003, in press).
35. A. F. Zakharov, N. S. Kardashev, V. N. Lukash, and S. V. Repin, Mon. Not. R. Astron. Soc. (2003, in press); astro-ph/0212008.
36. C. W. Misner, K. S. Thorne, and J. A. Wheeler, *Gravitation* (Freeman, San Francisco, 1973).
37. L. D. Landau and E. M. Lifshits, *Field Theory* (Nauka, Moscow, 1998).
38. B. Carter, Phys. Rev. D **174**, 1559 (1968).
39. S. Chandrasekhar, *Mathematical Theory of Black Holes* (Clarendon Press, Oxford, 1983).
40. A. F. Zakharov, Zh. Éksp. Teor. Fiz. **91**, 3 (1986) [Sov. Phys. JETP **64**, 1 (1986)].
41. A. F. Zakharov, Zh. Éksp. Teor. Fiz. **95**, 385 (1989) [Sov. Phys. JETP **68**, 217 (1989)].
42. A. F. Zakharov, Astron. Zh. **68**, 58 (1991) [Sov. Astron. **35**, 30 (1991)].
43. C. W. Gear, *Numerical Initial Value Problems in Ordinary Differential Equations* (Prentice Hall, Englewood Cliffs, New York, 1971).
44. K. L. Hiebert and L. F. Shampine, *Implicitly Defined Output Points for Solutions of ODE-s* (Sandia report sand80-0180, February, 1980).
45. A. C. Hindmarsh, *ODEpack, a Systematized Collection of ODE Solvers In Scientific Computing*, Ed. by R. S. Stepleman *et al.* (North-Holland, Amsterdam, 1983), p. 55.
46. L. R. Petzold, SIAM J. Sci. Stat. Comput. **4**, 136 (1983).

Translated by D. Gabuzda

Astronomy Reports, Vol. 47, No. 9, 2003, pp. 740–749. Translated from Astronomicheskiĭ Zhurnal, Vol. 80, No. 9, 2003, pp. 805–815.
Original Russian Text Copyright © 2003 by Goranskij, Barsukova, Burenkov.

Photometry and Spectroscopy of the System V4641 Sagittarii in Quiescence

V. P. Goranskij[1], **E. A. Barsukova**[2], and **A. N. Burenkov**[2]

[1]*Sternberg Astronomical Institute, Universitetskiĭ pr. 13, Moscow, 119992 Russia*
[2]*Special Astrophysical Observatory, Russian Academy of Sciences, Nizhniĭ Arkhyz, Karachai-Cherkessian Republic, 357147 Russia*

Received November 18, 2002; in final form, March 14, 2003

Abstract—We present the results of our CCD photometric and moderate-dispersion spectroscopic observations of the binary system V4641 Sgr, which contains a black hole of mass $\approx 9.5\,M_\odot$ and a normal B9III star. The photometric light curve reveals an ellipticity effect with very high amplitudes in V and R, 0.40^m and 0.37^m, and the color curve shows that the surface temperature is nonuniform. All this testifies to tidal distortion of the normal star's surface due to the massive companion and to a high inclination of the orbit to the line of sight. In June and July 2002, during quiescence, we obtained data during three flares with amplitudes up to 0.26^m. In particular, spectroscopic observations were acquired near the time of the black hole's inferior conjunction. One hour before conjunction, a depression by EW = 0.5 Å was observed in the red wing of the Hα absorption line, interpreted as absorption by gas flowing in the direction from the observer toward the normal star. This flow is apparently associated with a rarefied gas disk around the black hole, and the conjunction grazes the stellar surface if the orbital inclination is close to 70.7°. The maximum velocity along a circular Keplerian orbit is 650 km/s at a distance of $R = 0.15$–$0.20a$ from the black hole (where a is the component separation). Thus, we find the mass of the black hole to be $M_{BH} = 7.1$–$9.5\,M_\odot$, confirming the model of Orosz *et al.* (2001). © *2003 MAIK "Nauka/Interperiodica".*

1. INTRODUCTION

V4641 Sgr (GSC 6848.3786; $18^h19^m21.64^s$, $-25°24'25''.7$, 2000) was discovered by Goranskij [1] during an outburst in June 1978. At that time, the star brightened to 12.4^m in the B band, two magnitudes above its mean quiescent level, 14.2^m. This was the only outburst in the large series of 345 photographic plates of the Sternberg Astronomical Institute (SAI) obtained in 1960–1990. In the fourth edition of the General Catalogue of Variable Stars, the new variable was erroneously identified with GM Sgr (discovered earlier by Luyten) and classified as a nova-like variable. Later, Goranskij [2] established that the star was a binary of spectral type A, with a possible orbital period of 0.7365^d. No ultraviolet excess, characteristic of nova-like variables, was observed. An outburst as strong as that observed in 1978 is a very extraordinary event for such a system. The question of the star's identification was finally solved in 2000, when Luyten's discovery photographic plate showing GM Sgr (HV 4048) was located [3]. After that, Goranskij's star was named V4641 Sgr. It turned out to be 1′ to the north of Luyten's variable, GM Sgr. A finding chart for both objects was published in [4].

On February 20–22, 1999, V4641 Sgr was detected as a faint, variable X-ray source [5, 6], which was designated SAX J1819.3–2525 and XTE J1819–254. Another strong outburst of the star detected in the optical, X-ray, and radio occurred later, in September 1999, 21 years after the earlier outburst in 1978. The outburst of September 15, 1999 proceeded as follows. Six days before the outburst peak, the star's brightness increased to 11–$12^m V$ and demonstrated fluctuations with a 2.5-day period [7, 8]. At epoch 1999 September 15.395 UT, Stubbings [9] observed the outburst's maximum brightness, 8.8^m vis. After the maximum, the brightness fell to its quiescent level within two days. Unusually strong and broad Balmer emission lines were observed during the outburst, with HeII λ4686 and 5410 Å and HeI λ5876 Å emission also seen [10, 11]. The half-width of the Hα line reached 2700 km/s, and the emission line's wings reached ±6000 km/s. The full width of the HeI and Brγ emission in the infrared reached 5900 km/s [12]. Spectral changes during the outburst's decline were detected in [13]: the emission decreased most slowly in the Hα line, whereas the other Balmer lines immediately went into absorption.

During the brightness decline after the maximum of the optical outburst, the X-ray flux from V4641 Sgr increased [14, 15]. The flux at 2–12 keV increased from 0.2 to 12 Crab in 8 hours, then dropped abruptly to the detection limit. The hardness of the X-ray spectrum decreased as the flux grew. An X-ray pre-outburst half a day before the optical maximum was also found in the RXTE and CGRO data. The X-ray flux varied strongly during the outburst: by a factor of four on a time scale of seconds and by a factor of 500 on a time scale of minutes [16]. Such X-ray variability is typical of accretion onto black holes. The RXTE data showed that the X-ray source was faint at 2–60 keV and displayed irregular variability during the 7 months before the outburst on September 15, 1999 [17]. The object is visible in X-ray images of the Galactic center [18].

After the outburst of September 15, 1999, a declining radio source was observed during 12 days at 1.4–8.4 GHz. This source had a flux density of 400 mJy at 8.4 GHz and was optically thick at the outburst maximum, but soon became optically thin in the radio. It was resolved in VLA observations obtained on September 16, forming a jet-like extension 0.25″ long with an axis ratio of 10 : 1. The jet was undetectable in the radio two days later [14]. The September 15, 1999, outburst of V4641 Sgr can be interpreted as an event associated with super-Eddington accretion onto a black hole [19, 20]. During the outburst, an optically thick outflow (or envelope) with properties resembling those of the outflow from SS 433 was formed around the black hole.

A third outburst of V4641 Sgr was detected by R. Stubbings on May 19, 2002, 2.7 years after the second outburst. The peak brightness reached 10.5^m R. Rapid variability with an amplitude as high as 1.5^m and a time scale from minutes to hours was observed. The results of intense photometric monitoring of this outburst are presented in [21]. Repeated brightenings and large-amplitude brightness variability persisted until May 25. However, occasional flares with durations of several minutes and amplitudes up to 1^m continued to be observed much later, in early July (see the VSNET data at http://kusastro. kyoto-u.ac.jp/vsnet). V4641 Sgr is the only object for which many observers have been able to note flickering optical brightness of a black-hole system visually with their telescopes (cf. VSNET). The rapid brightness fluctuations on the shortest time scales of seconds had amplitudes up to 0.2^m in the B band. The star also became detectable again in the radio and X-ray [22–24]. Unlike in September 1999, the radio source was not extended, and flared on time scales from minutes to hours with an amplitude of 30% but did not fluctuate on time scales of seconds. This behavior differed from that observed in September 1999, when the optically thin radio emission declined over more than a week. The radio source was optically thick in July 2002 and appeared and disappeared abruptly and unexpectedly [22, VSNET]. The last date when the radio source was detected was July 12, 2002.

Special observations were organized to measure the star's X-ray and radio fluxes in quiescence. The source was not detected in Chandra observations with an exposure time of 72 min obtained on August 5, 2002; the upper limit for the flux density was 1.3×10^{-14} erg cm^{-2}s^{-1} at 0.5–7 keV. VLA observations obtained on August 1–13, 2002 showed the radio flux to be below 0.07–0.1 mJy [25]. However, the source was detectable in the radio at the 1.6 and 1.1 mJy levels on July 17 and 18, 2000, during a long period of quiescence [26].

The orbital period of the V4641 Sgr system, 2.81730 ±0.00001 days, was determined in [27] using radial-velocity measurements and our brightness estimates obtained using the SAI's plate archives. According to [27], the V4641 Sgr system contains a black hole with a mass of 8.7–11.7 $M_\odot$. Thus, the unusual behavior displayed in the optical and at other wavelengths is associated with the accreting black hole in the system. The mass of the normal B9III star is 5.5–8.1 $M_\odot$.

The 2.817-day orbital period was also detected in X-ray observations obtained on March 13–August 20, 1999, when the star was a weak X-ray source [20]. The variability amplitudes were, on average, 36 and 25% at 1.5–3.0 keV and 3–5 keV, respectively. The maximum flux occurs near the phase of the black hole's inferior conjunction. The variability with the orbital period can be explained as being due to extinction along the line of sight, near the optical star [20]. No X-ray eclipses have been observed [17].

Distance estimates for V4641 Sgr vary widely, from 0.5 kpc [14] to 9.6 kpc [27].

This paper presents the results of precision CCD photometry of V4641 Sgr in quiescence, outside large outbursts, together with the results of spectroscopic observations obtained using the 6-m telescope of the Special Astrophysical Observatory (SAO) at orbital phases close to the black hole's inferior conjunction. The results of our observations were briefly reported in [28]. Here, we present them in detail, with additional new results of photometry carried out in 2002.

2. PHOTOMETRY

Our photometric observations of V4641 Sgr were acquired on July 24–August 21, 2000, May 14–27, 2001, and June 28–July 20, 2002 in photometric bands close to V and R_J with the 38 cm reflector of the Crimean Astrophysical Observatory (CrAO) and the 60 cm Zeiss telescope of the SAI's Crimean Station, using SBIG ST-7 and ST-8 CCDs. On July 6–8, 2002, we obtained observations in the V and R_C

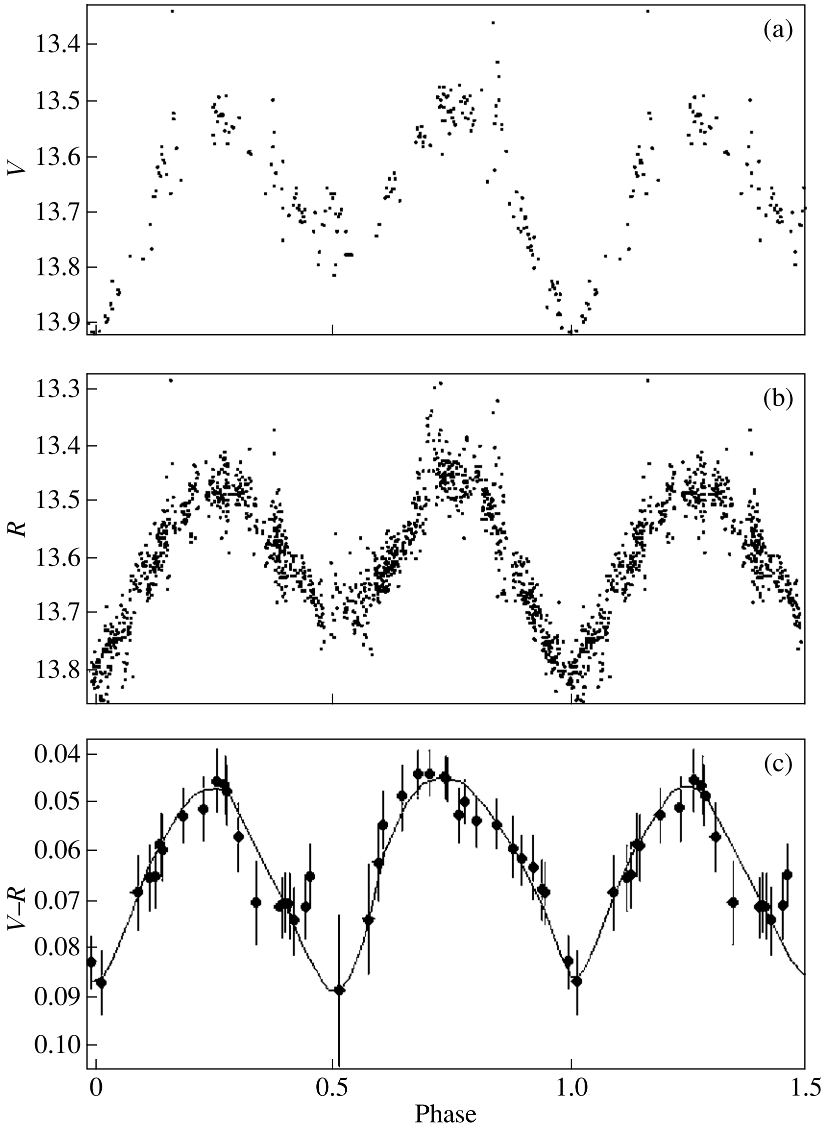

Fig. 1. (a) V-band and (b) R-band light curves and (c) the mean $V-R$ color curve.

bands with the 1 m Zeiss reflector of the SAO using a K-585 CCD chip. The object has a large negative declination (−25.4°) and is observed at air masses of 2.9 or more, making the conditions for photometry unfavorable even for our Southern observatories. The V observations in 2000 were carried out only very near the sky meridian, and the measurements for each night were averaged. In the R band, where the atmospheric extinction coefficients are lower than in the V band, we were able to organize long-time monitoring of the object in sessions lasting 4–5 hours. The exposure times were 2–5 minutes.

The observations were reduced under Windows NT using photometric code written by V.P. Goranskij. We used one comparison star and several control stars in the immediate vicinity of V4641 Sgr.

The V-band comparison star was star "e" [2]; its magnitude, $V = 13.38^m$, was derived using the photoelectric standard GSC 6848.3438 (star "a"). Henden [29] gives $V = 13.433^m$, $B - V = 1.182$, $U - B = 1.011$, $V - R_C = 0.689$, $R_C - I_C = 0.592$ for this star, in reasonable agreement with our data. To calibrate our observations in the R_J band, we adopted the magnitude 12.47^m for the comparison star, computed from its magnitude in the R_C band [29]. Some of our observations were published in [30]. In our analysis of the light curve, we included photoelectric observations obtained by V.P. Goranskij on two nights before the 1999 outburst (JD 2449578 and 2449599) with the 1 m Zeiss reflector of the Tien Shan Astronomical Observatory in Kazakhstan, as well as a single observation (on JD 2446708)

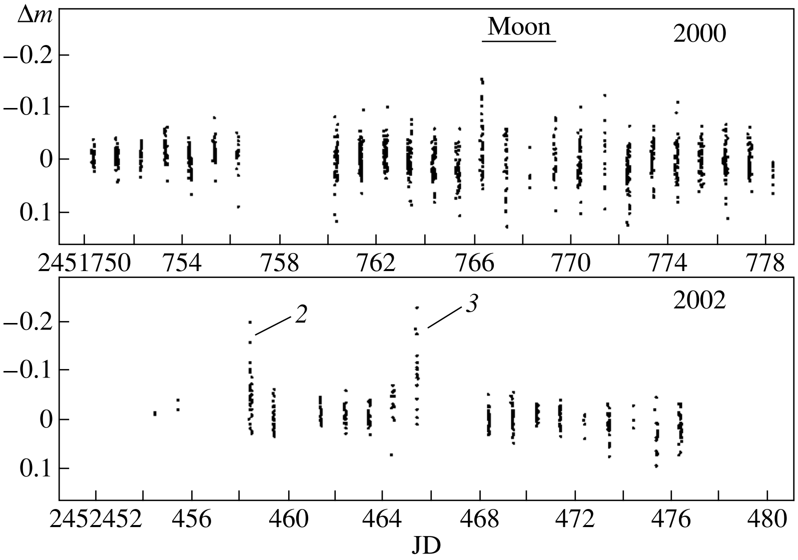

Fig. 2. Deviations from the mean orbital light curve of V4641 Sgr for the 2000 and 2002 observing seasons. The arrows mark individual episodes of flaring activity.

obtained with the 1-m reflector at Mt. Sanglok, Tajikistan. We also used the V monitoring data of [31], which systematically deviate from our data by -0.25^m.

We acquired a total of 204 V and 1248 R observations.

3. LIGHT CURVES

Figures 1a, 1b present the V and R light curves of V4641 Sgr. We used the light-curve elements of [30], derived from old photographic and photoelectric observations:

$$\text{Min I} = \text{JD } 2451764.298 + 2.81728(\pm 1)^{\text{d}} E. \quad (*)$$

The new 2002 observations demonstrated that a small correction to the time of minimum ($+0.0056^{\text{d}}$) was needed, and we accordingly applied the more accurate value Min I = 2451764.3036. The value of the period did not require improvement. According to the radial velocity curve of [27, Fig. 2], the highest radial velocity of the normal component occurs at phase 0.75 for our elements, so that the black hole is at inferior conjunction at Min I. Thanks to the increased transparency of the atmosphere in the red, we were able to obtain complete orbital-phase coverage of the light curve in R. The mean uncertainty of our observations was 0.02–0.03^m. There was no obvious correlation between deviations from the mean light curve and the corresponding air masses. The distribution of the deviations is close to normal.

The light curves show that the ellipsoidal light curve of V4641 Sgr is a double wave whose minima have unequal depths: Min I $= 13.92^m$ and Min II $= 13.72^m$ in V, Min I $= 13.82^m$ and Min II $= 13.70^m$ in R. The difference in the depths of the minima, 0.12–0.20^m, is unusually large for ellipsoidal variability. The 1994 Tien Shan observations at the phases of the primary and secondary minima demonstrate that the brightness ratio for the primary and secondary minima was the same before and after the 1999 outburst. The individual data points deviating upwards from the light curve reflect the star's activity. Excluding these points, the estimated brightnesses at maximum are $V = 13.52^m$ and $R = 13.45^m$. The total amplitudes of the ellipsoidal variability are $\Delta V = 0.40^m$ and $\Delta R = 0.37^m$, which are the largest recorded to date for binaries with compact components. They are also the highest amplitudes in theoretical models for the optical components in the absence of eclipses in the system [32].

The light curve derived from our observations was comparatively stable, and we observed no evidence for significant changes of the brightness level of the light curve such as those suspected earlier based on photographic observations [2]. Only small and rare upwards deviations of the data points are present, which we subjected to a detailed analysis.

The large amplitude of the ellipsoidal variability testifies to strong tidal distortion of the secondary by the massive black hole and a large inclination of the orbit to the line of sight. It is clear that the contribution of the normal component to the light curve in quiescence is 100%. The upper limit for the orbital inclination, $i \leq 70.7°$ [27], can be derived from the component mass ratio, $q = M_x/M = 1.5$, and from the observation that no X-ray eclipses occur in the system. The shape of the normal component's surface appears to be strongly elongated toward the black hole and less elongated in the opposite direction. Parts of the stellar surface at larger distances from the central source are less heated by this source and thus emit less light and have lower surface temperatures. This effect is taken into account when modeling accretion disks (for example, cf. [33]).

We made a special analysis of the temperature variations with the orbital phase for the $V-R$ color index. The color indices, calculated as differences between V and R magnitudes measured at nearby times, show a large scatter, and the effect of the temperature variations is almost indistinguishable. We estimated its amplitude by calculating a sliding average of the color curve; the result is presented in Fig. 1c. The amplitude of the double wave in the color indices is $\Delta(V-R)=0.04^m$, corresponding to a temperature difference in excess of 1600 K, with the mean temperature being 10 000 K. However, color differences are not detectable in the minima due to insufficient accuracy of the observations.

Heating of the normal component's surface by X-rays from the compact component could also lead to unequal minima, as is often observed for X-ray binaries. In this case, the brightness in the minimum corresponding to the inferior conjunction of the compact component should be higher than the brightness at the superior conjunction. No such effect is observed for V4641 Sgr, even during outbursts, when the star is a strong X-ray source. The local brightness maxima of the 1999 [7] and 2002 [21] outburst light curves are not associated with the zero phase of the photometric elements. In particular, a wave with a period of 2.5 days and an amplitude of about 1^m was detected during two variability cycles during the 1999 outburst [7]. The orbital period, equal to 2.817 days, is now well established, and we can confirm that the observations of [7] are not in contradiction with this orbital period, with the light-curve minimum corresponding to phase 0.25 of the elements (*). Thus, the shape of the light curve during the outburst was not due to the effects of heating. Our observations of V4641 Sgr in quiescence show a primary, deeper minimum at phase 0.00 (the inferior conjunction of the compact component), testifying to a complete absence of effects due to heating of the normal star. In [27], a partial eclipse by the accretion disk was suggested as one origin of the unequal minima of V4641 Sgr.

PROPERTY OF PHOTOMETRIC ACTIVITY OUTSIDE THE OUTBURSTS

Usually, photometric activity of an X-ray system is manifest as an excess brightness over the quiescent level of the orbital variability. Examples are given by the systems V1357 Cyg (Cyg X-1) [34] and V1341 Cyg (Cyg X-2) [35]. Figure 2 plots deviations from the mean light curve of V4641 Sgr for the best-covered monitoring intervals in 2000 and 2002. This figure combines the deviations for both V and R to improve the time resolution of the light curve (measurements in these filters were often made in alternating observations). The deviations are concentrated near zero for most nights, and we can conclude that the object was mostly observed in its quiescent state.

During the 2000 observing run, increased scatter and upward deviations of data points were observed on the single night of JD 2451766, but the reality of these variations is doubtful: the light of the full Moon fell on the telescope, and the field of the CCD chip was illuminated nonuniformly (the object is in the ecliptic). This could introduce systematic errors in these observations. Observations with the SAO 1 m Zeiss telescope on the night of JD 2452432, 12 days after the end of the large outburst in May 2002 (event 1 in Fig. 3; this event is not shown in Fig. 2) showed the object's brightness to be clearly higher by $\Delta m=0.26^m$, after which the brightness declined over 0.02 days. Two additional episodes of activity were recorded in July 2002, on JD 2452458 (event 2) and JD 2452465 (event 3) (Fig. 2 and, in more detail, Fig. 3). All three events were observed in both V and R during good weather, making their reality beyond doubt. The variability amplitude reached 0.2^m, and the time scale was generally shorter than the exposure time, making our estimates of the amplitude too small.

Our observations during July 2002 also demonstrated a gradual, low-amplitude decline of the mean brightness level, by on average 0.04^m, as is apparent in Fig. 2 (bottom panel).

T. Kato reported an episode of flaring activity of V4641 Sgr on July 7–8, 2002 (JD 2452462–2452463) in the VSNET circulars. A 1^m flare was recorded on July 7, with the rise to maximum lasting only 30 s (the star's CCD image during this flare is shown on the VSNET web page). The e-folding decay time for the flare was several minutes. Numerous rapid flares with amplitudes up to 0.3^m were observed, and were confirmed by independent series of CCD observations in Japan. It is striking that the observations from the longitude of Crimea on the same dates revealed V4641 Sgr in an absolutely quiescent phase (Fig. 2). According to the VSNET information, the flare activity was over on July 11 and 12 (JD 2452466 and 2452467). Our data show the last episode of activity, event 3, which occurred on July 10 (JD 2452465).

The radio flux observed with the VLA from June 16 until June 29, 2002 (JD 2452442–2452455) varied

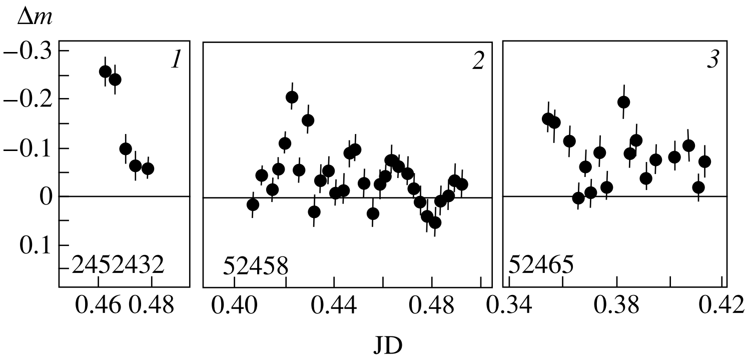

Fig. 3. The light curves for the three episodes of flaring activity.

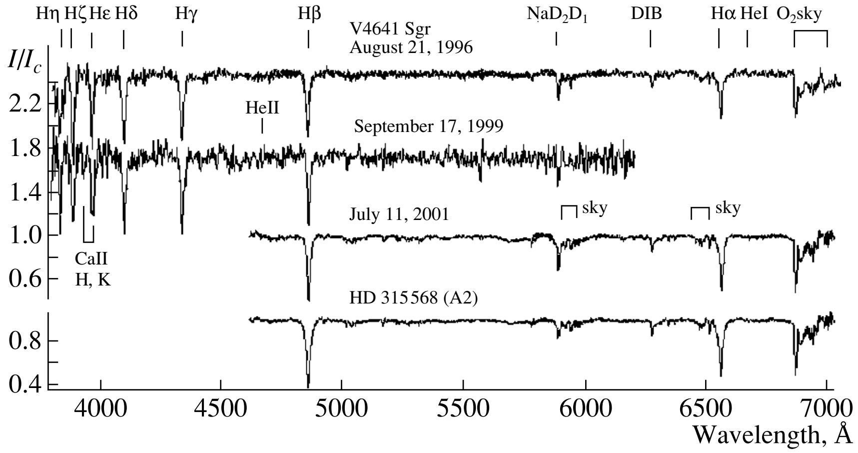

Fig. 4. Spectra of V4641 Sgr. For comparison, the spectrum of the control star HD 315568 (A2) is shown in the bottom.

within 0.44–2.38 mJy [36]. The object remained active, with mini-flares occurring every day, and appeared for several minutes from time to time. Our set of observations coincides with radio data for only one date, June 29, 2002 (JD 2452455), when we have two observations in V and R. The object was observed to be in its quiescent state.

Based on all the optical and radio observations, we can conclude that the object's residual activity after its large outburst in May 2002 lasted for two more months. During this period, the object appeared in the radio from time to time, several times each day, and its optical brightness increased over the brightness level of the normal star exhibiting ellipsoidal variations.

4. SPECTROSCOPIC OBSERVATIONS

Our spectroscopic observations were acquired in July 2001 using the SAO 6-m telescope and the UAGS spectrograph at phases near the black hole's inferior conjunction, in order to see the contents of the Roche lobe and the immediate vicinity of the black hole against the background of the normal star. In addition, we obtained similar spectra for the 8^m A2 control star HD 315568, which is near V4641 Sgr in the sky.

We also analyzed spectra of V4641 Sgr obtained on the 6-m telescope in 1996 and 1999 using the SP-124 spectrograph. A blue spectrum containing the Hβ line was taken on September 17, 1999, only two days after the peak of the outburst on September 15. Information about the spectra, including the wavelength range they cover and their resolution, is given in the Table. The observations were reduced by E.A. Barsukova using standard techniques in the MIDAS package. Further, all the spectra obtained on a given night in a particular wavelength range were summed. The normalized spectra for V4641 Sgr and the A2 control star HD 315568 are shown in Fig. 4, and profiles of the Hα and Hβ lines in Figs. 5 and 6.

The orbital elements were not known in 1996 and 1999, so that the observations were obtained at arbitrary phases (0.37 and 0.60). The 1996 spectra are visually indistinguishable from those of a normal, single, late B to early A star. In addition to the broad Balmer absorption lines, we can identify the

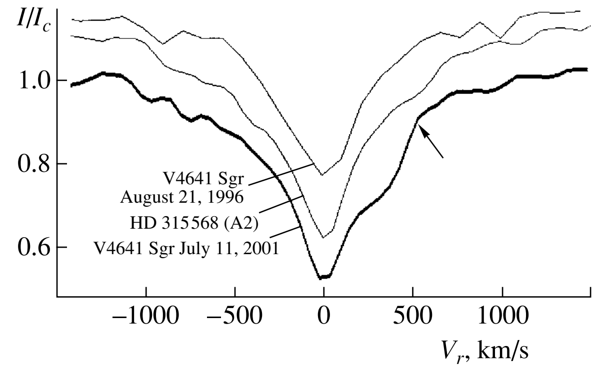

Fig. 5. Profiles of the Hα line in the spectra of V4641 Sgr, compared to the A2 star HD 315568. The line profile near the inferior conjunction of the black hole is shown as a thick curve. The arrow marks the highest velocity of the depression, 534 km/s.

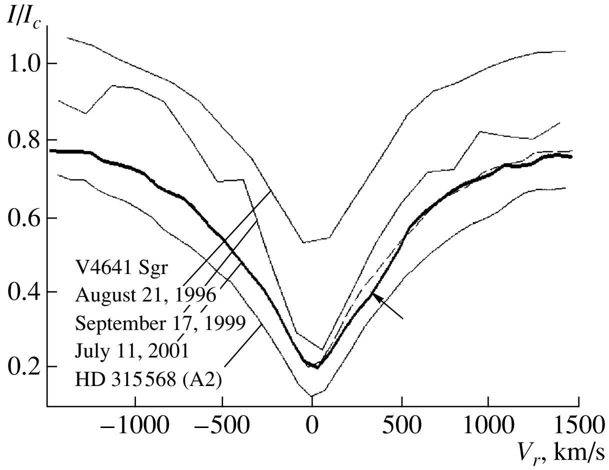

Fig. 6. Profiles of the Hβ line in the spectra of V4641 Sgr compared to the A2 star HD 315568. The line profile for the inferior conjunction of the black hole is shown by the thick curve. We have superimposed a mirror reflection of the blue wing of this profile over the red wing. The arrow marks the deficit of light in the red wing.

H and K Ca II and D_1 and D_2 Na I doublets, both at the resolution limit. The absorption line profiles are symmetrical and show no evidence for emission components from the accretion disk. Overall, the quiescent spectra suggest that V4641 Sgr is a system without active mass exchange. Figure 4 shows that the Balmer absorption lines are broader and stronger for HD 315568 than for V4641 Sgr. This is due to Stark broadening at higher pressure, confirming the conclusion of [27] that the normal component of V4641 Sgr has an enhanced luminosity.

The spectra at λ3800–6200 Å taken on September 17, 1999, only two days after the maximum of the large optical and X-ray outburst, also show absorption features, though Hα emission was still observed at that time [13] (outside the range of our spectra). No HeII λ4686 Å emission is visible. Because of the low signal-to-noise ratio of the spectra (≈ 10), we are able to note only the asymmetry of the Balmer absorption profile. In particular, excess emission is clearly visible in the blue wing of the Hβ line in Fig. 6, making the profile very asymmetrical.

We organized observations of V4641 Sgr on the 6-m telescope on July 11, 2001, near the inferior conjunction of the black hole, in order to view its surroundings against the stellar disk of the normal component. These observations were approximately two years after the 1999 outburst, during a long period of quiescence. We obtained two spectra in the red containing the Hα absorption line, and two spectra in the blue containing the Hβ line. Recall that V4641 Sgr has a low declination and was observed through about three air masses. The conditions during these observations were favorable: the seeing was $\approx 2''$, and the sky had cleared after several days of rain and fog. For this reason, we observed a neighboring control star of the same spectral type. Weak atmospheric water absorption lines at zero velocity are seen in the spectra of V4641 Sgr and the control star. The spectra have a high signal-to-noise ratio of about 200, and a spectroscopic resolution of 3.6 Å.

Figures 5 and 6 demonstrate profiles of the Hα and Hβ absorption lines obtained on July 11, 2001 (thick curves). For comparison, the thin curves show the profiles of V4641 Sgr obtained in 1996 and 1999 and the profiles for the control star, HD 315568. All the profiles are shown on the same scale but are plotted with arbitrary shifts along the intensity axis for ease of comparison. The profiles are also combined along the radial-velocity axis. A depression with equivalent width EW = 0.5 Å is observed in the red wing of the July 11 Hα profile in Fig. 5 (for comparison, the total equivalent width of the Hα line is 9.5 Å). This depression is equally obvious in two individual spectra, and the profile in Fig. 5 is a combination of both. The spectra were taken one hour before the black hole's inferior conjunction, at mean orbital phase 0.9867. The depression is due to gas flowing from the observer toward the normal star being seen against the stellar disk.

S.N. Fabrika (SAO) has suggested that this gas flow could be part of a rarefied gaseous disk around the black hole, in the system's orbital plane. This gas is transparent in the continuum and is opaque only in the Balmer lines. The highest heliocentric velocity of the depression projected onto the line of sight, derived from the line profile, is 642($\pm$10) km/s, and the heliocentric velocity of the system's center of mass, which follows directly from our observations, is

Spectroscopic observations of V4641 Sgr with the 6 m telescope

JD hel. 24...	Date	Orbital phase	λ, Å	Dispersion, Å per pixel	S/N
50317.2535	August 21, 1996	$0\overset{\text{p}}{.}36$	4730–7200	2.4	50
50317.2642	″		″	2.4	50
50317.2812	″	0.38	3700–6100	2.4	50
50317.2854	″		″	2.4	50
51439.1807	September 17, 1999	0.60	3800–6200	2.4	10
51439.1889	″		″	2.4	10
52102.3325	July 11, 2001	0.9841	5800–7100	1.2	120
52102.3471	″	0.9893	″	1.2	180
52102.3643	″	0.9954	4630–5880	1.2	120
52102.3790	″	0.0006	″	1.2	120

$\gamma = 108 \pm 3$ km/s. This latter value coincides with the value 107.4 ± 2.9 km/s found in [27] within the errors. The line profiles in Figs. 5 and 6 were combined according to their centers of symmetry, and the arrow in Fig. 5 shows the edge of the depression with the highest velocity in the system of the center of mass, 534 km/s.

We analyzed various possible origins of line-profile distortion due to the Earth's atmosphere. No similar depression is observed for the nearby control star, making atmospheric absorption improbable. In contrast to the control star, narrow sky emission lines appear in the Hα profile of V4641 Sgr due to the longer exposure time. We checked pixel-by-pixel the action of the MIDAS code when subtracting sky lines, in order to be sure that the observed depression was not due to incomplete or excessive subtraction of sky emission lines. In addition, no sky emission lines were found in the part of the profile where the depression is observed. Thus, we have every reason to believe that this feature is real.

The presence of the observed depression implies that the conjunction of the black hole in the system of V4641 Sgr grazes the limb of the normal star and that the orbital inclination is equal to the extreme value of 70.7°.

It is important that the blue wing of the Hα profile shows no trace of the absorption that is expected in the presence of an accretion gas flow from the secondary through the Lagrangian point L_1. This may mean that V4641 Sgr is a detached system and that the normal star does not fill its Roche lobe.

The spectra in the blue taken on the same night at orbital phase 0.9980, much closer to the phase of inferior conjunction, do not show such a depression in the Hβ absorption profile, which is more symmetrical than the Hα profiles. However, a slight depression in the red wing of the line becomes visible if we superimpose the mirror reflection of the blue wing over the red wing, as in Fig. 6 (dashed curve). The depression is revealed as a significant asymmetry in the profile's shape. Such large differences between the Hα and Hβ profiles are striking, and must be explained. Since the probability for a photon to be absorbed by a hydrogen atom is the same for both these Balmer lines (in both cases, the absorption implies capture of a photon by an electron in the second level), effects observed in the Hα and Hβ lines should be equal. We explain the lack of a deep depression in the Hβ line by the fact that a distant part of the gaseous disk is projected onto the star's disk at this phase, and the projection of its circular velocity onto the line of sight is much smaller, so that the line absorption pattern is more symmetrical about the line center. In this case, it is natural to expect that, after the conjunction, a depression should be observed in the blue wing of the line, this time from a gas flow directed *toward the observer*. Of course, we assume here that the gaseous disk is in the orbital plane. On the other hand, for a system without flow through the Lagrangian point L_1, the gaseous disk could be tilted. The rarefied gas could reach the vicinity of the black hole by flowing along magnetic field lines. However, photometric observations to date have not shown any evidence for magnetic activity in the form of spots on the normal star. In any case, it would be interesting to follow spectroscopic changes during the passage of the black hole near its inferior conjunction for a wider range of orbital phases.

5. MASS OF THE BLACK HOLE IN THE V4641 Sgr SYSTEM

We attempted to estimate the mass of the black hole from the velocity and the radius of the orbit where

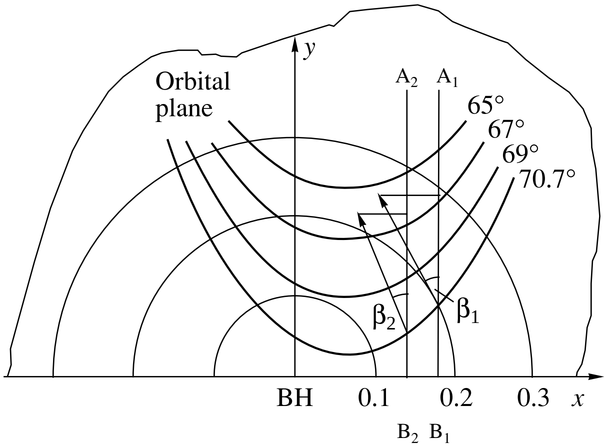

Fig. 7. Geometry of the star's eclipse by accretion-disk flows. The definition of the angle β between the flow direction and the projection of the line of sight onto the orbital plane at the star's limb is shown. See text for details.

the surrounding matter is moving. Since the flows in the accretion disk projected on the stellar disk move at different angles, sometimes even perpendicular to the line of sight, and move along different orbits, computation of the depression in the profile is a difficult task. It is much easier to estimate the orbital radius for the flow projected onto the stellar disk that has the highest velocity.

Knowing the velocity of an object in a Keplerian circular orbit and the orbit's radius, we can infer the mass of the central body. Equating the centripetal force for the circular motion and the gravitational force, we have

$$mv^2/R = GmM_{BH}/R^2,$$

where m and M_{BH} are the masses of the body in the circular orbit and of the central body, R is the distance between them, and G is the gravitational constant. It follows that

$$M_{BH} = v^2R/G.$$

However, the observations do not give the highest flow velocity but instead its projection onto the line of sight. To determine the velocity of the circular motion from this projection ($v_{proj} = 534$ km/s), we must take into account the orbital inclination ($i = 70.7°$) and the angle β between the direction of the orbital motion and the projection of the line of sight onto the orbital plane for the flow having the highest velocity. To find the angle β, we created a model of the system with $q = M_x/M_* = 1.5$ [27] and with a Roche lobe filling coefficient $\mu = 0.98$ for the phase when the red spectrum was obtained, 0.9867. Figure 7 plots intersections of the orbital plane by the line of sight passing by the star's limb (fragments of ellipses) for several values of the orbital inclination in the range $i = 65°{-}70.7°$. We also plot circular orbits with the increment $\Delta R = 0.1a$, where a is the distance between the black hole and the center of the normal star. We can see that the highest velocities for a given phase are observed at two points at the star's limb, at distances $R = 0.15{-}0.20a$ from the central body. Here, the angles between the direction of the circular motion and the projected line of sight (A_1B_1 or A_2B_2) are near $\beta = 30°{-}36°$. The radius of the gas-flow orbit determined from the model does not depend strongly on the component mass ratio but does depend on the orbital phase of the observation, which is known. The solution also depends on the orbital inclination. The angle β grows with decreasing inclination, so that the derived circular velocity increases, and the black hole's mass grows as the square of the velocity. We now determine the circular velocity from its projected value for the orbital inclination $i = 70.7°$: $v_{circ} = v_{proj}/(\sin i \cos\beta) = 650$ km/s. Adopting the value $a = 21.33\ R_\odot$ from [27], we find the black-hole mass to be $7.1\ M_\odot \le M_{BH} \le 9.5\ M_\odot$. These limits for the mass overlap considerably with the range $8.7\ M_\odot \le M_{BH} \le 11.7\ M_\odot$ from [27]. Even higher mass estimates can be obtained if the orbital inclination i is decreased. Thus, we have demonstrated that the measured velocity of the matter at the estimated distance corresponds to the velocity computed in the model with a massive black hole, confirming the mass estimate obtained in [27].

6. CONCLUSIONS

CCD photometry of V4641 Sgr reveals periodic brightness variations with an ellipsoidal nature, with two unequal minima during the 2.81728-day period and an amplitude of 0.4^m in the V band. The shape of the light curve is due to tidal distortion of the normal B9III star by its invisible massive companion. We have detected orbital color changes due to the nonuniform surface temperature of the normal star due to its elongated shape and nonuniform heating by the central energy source.

During a quiescent period following the May 2002 outburst of the star, we found photometric manifestations of activity: flares with amplitudes up to 0.26^m and a low-amplitude decrease of the brightness level. Residual signatures of activity after the outburst continued for two more months.

Our spectroscopic observations of V4641 Sgr with the SAO 6 m telescope at a phase near the inferior conjunction of the black hole provides evidence for a rarefied accretion disk surrounding the star, which absorbs the star's light in the hydrogen lines. Thus, the passage of the black hole grazes the limb of the star.

Based on the velocity of the disk material moving around the black hole and the orbital radius of the highest-velocity flow in the disk, we estimate the mass of the black hole to be $7.1\ M_{\odot} \leq M_{BH} \leq 9.5\ M_{\odot}$, confirming the model of [27].

ACKNOWLEDGMENTS

We are grateful to S.Yu. Shugarov (Sternberg Astronomical Institute, Moscow State University) for kindly providing his CCD observations made at our request and to D.N. Monin (Special Astrophysical Observatory) for his active participation in the 1996 and 1999 observations with the 6-m telescope. We also thank Prof. S.N. Fabrika (SAO) for helpful discussions and criticism.

REFERENCES

1. V. P. Goranskij, Astron. Tsirk., No. 1024, 3 (1978).
2. V. P. Goranskij, Inform. Bull. Var. Stars, No. 3464 (1990).
3. M. L. Hazen, D. Hoffleit, B. L. Welther, and D. B. Williams, AAVSO J. **28**, 99 (2000).
4. J. Orosz, Inform. Bull. Var. Stars, No. 4921 (2000).
5. J. in't Zand, J. Heize, A. Bazzano, *et al.*, IAU Circ. No. 7119 (1999).
6. C. B. Markwardt, J. H. Swank, and F. E. Marshall, IAU Circ. No. 7120 (1999).
7. T. Kato, M. Uemura, R. Stubbings, *et al.*, Inform. Bull. Var. Stars, No. 4777 (1999).
8. M. Uemura, T. Kato, T. Watanabe, *et al.*, Publ. Astron. Soc. Jpn. **54**, 95 (2002).
9. R. Stubbings, IAU Circ. No. 7253 (1999).
10. K. Ayani, T. C. Peiris, and A. C. Clarke, IAU Circ. No. 7254 (1999).
11. S. G. Djorgovski, R. R. Gal, A. Mahabal, *et al.*, ATEL No. 44 (1999).
12. P. A. Charles, T. Shahbaz, and T. Geballe, IAU Circ. No. 7267 (1999).
13. S. Chaty, I. F. Mirabel, J. Marti, and L. F. Rodriguez, Astrophys. Space Sci. **276**, 153 (2001), astro-ph/0102105.
14. R. M. Hjellming, M. P. Rupen, R. W. Hunstead, *et al.*, Astrophys. J. **544**, 977 (2000).
15. D. A. Smith, A. M. Levine, and E. H. Morgan, IAU Circ. No. 7253 (1999).
16. R. Wijnands and M. van der Klis, Astrophys. J. **528**, L93 (2000).
17. J. J. M. int'Zand, E. Kuulkers, A. Bazzano, *et al.*, Astron. Astrophys. **357**, 520 (2000).
18. M. G. Revnivtsev and R. A. Syunyaev, Pis'ma Astron. Zh. **28**, 83 (2002) [Astron. Lett. **28**, 69 (2002)].
19. M. Revnivtsev, R. Sunyaev, M. Gilfanov, and E. Churazov, Astron. Astrophys. **385**, 904 (2002).
20. M. Revnivtsev, M. Gilfanov, E. Churazov, and R. Sunyaev, Astron. Astrophys. **391**, 1013 (2002).
21. M. Uemura, T. Kato, R. Ishioka, *et al.*, Publ. Astron. Soc. Jpn. (in press, 2002); astro-ph/0208146.
22. M. Rupen, V. Dhavan, and A. Mioduszewski, IAU Circ. No. 7928 (2002).
23. D. Campbell-Wilson and R. W. Hunstead, IAU Circ. No. 7908 (2002).
24. C. B. Markwardt and J. H. Swank, IAU Circ. No. 7906 (2002).
25. J. A. Tomsick, M. P. Rupen, S. Corbel, *et al.*, ATEL No. 105 (2002).
26. R. M. Hjellming, ATEL No. 62 (2000).
27. J. Orosz, E. Kuulkers, M. van der Klis, *et al.*, Astrophys. J. **555**, 489 (2001).
28. V. P. Goranskij, E. A. Barsukova, A. H. Burenkov, and D. N. Monin, in *New Views on Microquasars,* Ed. by Ph. Durouchoux, V. Fuchs, and J. Rodrigues (Center for Space Physics, Kolkata, 2002, in press); astro-ph/0209592.
29. A. Henden, vsnet-campaign-v4641sgr. No. 133 (VSNET, 2002).
30. V. P. Goranskij, Inform. Bull. Variable Stars, No. 5068 (2001).
31. J. Marti, R. Zamanov, J. M. Paredes, and M. Ribo, Inform. Bull. Var. Stars, No. 5036 (2001).
32. E. A. Karitskaya, Candidate's Dissertation in Mathematical Physics (Moscow, Sternberg Astron. Inst., 1982).
33. A. V. Goncharskij, S. Yu. Romanov, and A. M. Cherepachshuk, *Astrophysic Finite-Parametric Inverse Problems* (Mos. Gos. Univ., Moscow, 1991), p. 77.
34. E. A. Karitskaya, I. B. Voloshina, V. P. Goranskij, *et al.,* Astron. Zh. **78**, 408 (2001) [Astron. Rep. **45**, 350 (2001)].
35. V. P. Goranskij and V. M. Lyuty, Astron. Zh. **65**, 381 (1988) [Sov. Astron. **32**, 193 (1988)].
36. M. Rupen, vsnet-campaign-v4641sgr No. 104 (VSNET, 2002).

Translated by N. Samus'

Astronomy Reports, Vol. 47, No. 9, 2003, pp. 750–762. Translated from Astronomicheskiĭ Zhurnal, Vol. 80, No. 9, 2003, pp. 816–829.
Original Russian Text Copyright © 2003 by Shimansky, Bikmaev, Galeev, Shimanskaya, Ivanova, Sakhibullin, Musaev, Galazutdinov.

Observational Constraints on Potassium Synthesis During the Formation of Stars of the Galactic Disk

V. V. Shimansky[1], **I. F. Bikmaev**[1], **A. I. Galeev**[1,2], **N. N. Shimanskaya**[1,3],
D. V. Ivanova[1], **N. A. Sakhibullin**[1], **F. A. Musaev**[4], **and G. A. Galazutdinov**[4]

[1]*Kazan State University, Kazan, Russia*
[2]*Kazan State Pedagogical University, Kazan, Russia*
[3]*Kazan State University of Energetics, Kazan, Russia*
[4]*Special Astrophysical Observatory, Russian Academy of Sciences, Nizhniĭ Arkhyz, Russia*

Received January 10, 2003; in final form, March 14, 2003

Abstract—The non-LTE potassium abundances in the atmospheres of 33 Galactic-disk stars are derived and the parameters of the atmospheres of 23 of the stars are determined. Neglecting departures from LTE results in a systematic overestimation of the potassium abundances and an increase in their dispersion, even for differential analyses relative to the Sun. The non-LTE corrections are significant ((−0.2)–(−0.6) dex) and depend on the surface gravities and effective temperatures of the stars. The mean potassium abundance for a sample of ten stars with [Fe/H] ~ 0.0 is in agreement with the solar and meteoritic abundances ($\log \varepsilon_{\odot}(\mathrm{K}) = 5.12$). As the stellar metallicity increases from [Fe/H] = (−1.0) to (0.2) dex, the [K/Fe] ratio decreases systematically from 0.3 dex to −0.1 dex. The derived dependence [K/Fe]–[Fe/H] is in agreement with the results of published model calculations of the chemical evolution of the Galaxy. This indicates the dominance of explosive oxygen burning in massive type II supernovae during the synthesis of potassium in the Galactic disk. *© 2003 MAIK "Nauka/Interperiodica"*.

1. INTRODUCTION

For a long time, the determination of potassium abundances in the atmospheres of late-type stars remained beyond analyses of the chemical evolution of the Galaxy. The main obstacle to such studies was the absence of measurable and unblended KI lines in the optical. The only lines available for quantitative analyses were the $\lambda\lambda$7665, 7699 Å resonance doublet, which lies in the infrared, where the efficiency of traditional photographic detectors was very low. Therefore, the possibility of analyzing potassium abundances $\log \varepsilon(\mathrm{K})$ for large samples of stars arose only after the implementation of RETICON and CCD detectors in astrophysical observations. The first study of this kind was carried out by Gratton and Sneden [1, 2], who derived the [K/Fe]–[Fe/H] dependence for 23 dwarfs and giants of various spectral classes based on LTE analyses of their spectra. Though the deviations from this dependence were appreciable for some stars (up to Δ[K/Fe] = 0.5 dex), overall, the [K/Fe] ratio decreased with increasing metallicity. A similar result was obtained by Chen *et al.* [3], who carried out an LTE analysis of the chemical compositions of 90 dwarfs in the Galactic disk, and showed that the ratio [K/Fe] decreases steadily from [K/Fe] = 0.4 for [Fe/H] = −1.00 to [K/Fe] = 0.07 for [Fe/H] = 0.00. At about the same, Tomkin *et al.* [4] study of the potassium abundances of eight stars with $0.05 < [\mathrm{Fe/H}] < 0.25$ indicated that the same dependence is obeyed by stars with overabundances of metals. Thus, LTE analyses of existing observational data provided evidence for a systematic decrease in the rate of synthesis of potassium during the formation of stars of the Galactic disk. The overabundance of potassium in solar-metallicity stars was worthy of special attention in theoretical modeling of the chemical evolution of the Galaxy.

At the same time, most theoretical studies of the synthesis of chemical elements [5–7] have predicted complex behavior for the [K/Fe]–[Fe/H] dependence, with a definite increase in [K/Fe] in the transition to stars of the thin Galactic disk (dashed curve in Fig. 5). It is known that ^{39}K, which is an odd element, is produced mainly during oxygen burning type II supernovae. Timmes *et al.* [5] showed that, in a model with oxygen burning under hydrostatic equilibrium conditions, the abundance of potassium in disk stars should increase from [K/Fe] = −0.40 to [K/Fe] = 0.00 for metallicities $-0.80 < [\mathrm{Fe/H}] < 0.00$, i.e., in the opposite sense shown by the observational data! Later, using more complete models, Alibes *et al.* [6] and Goswami and Prantzos [7] confirmed the main results of Timmes *et al.* [5], stressing that the synthesis of potassium occurs during oxygen burning under the conditions of hydrostatic equilibrium. At the same time, Samland [8] considered an alternative model for the synthesis of potassium in explosive oxygen burning in type II supernovae, which yielded a [K/Fe]–[Fe/H] dependence in qualitative agreement with the data of Gratton and Sneden [1].

To resolve these contradictions, it was suggested [3, 5] that there are departures from LTE in the level populations of KI that can substantially change the potassium abundances derived assuming LTE. Preliminary non-LTE computations of the equilibrium states of the KI atom carried out for the conditions in the solar atmosphere [9, 10] have shown that these assumptions are justified. One main factor leading to substantial differences in the derived non-LTE and LTE abundances is the strong "over-recombination" of atoms in the atmospheres of late-type stars. The effects of over-recombination, which were studied in detail in [9, 11], are determined primarily by the interaction of two factors: the low efficiency of the ionization of atoms from the $4s$ ground state and the presence of intense spontaneous transitions in infrared resonance and subordinate lines. As a result, theoretical non-LTE KI lines are always enhanced, and the derived non-LTE abundances are reduced compared to the LTE case. The behavior of the corresponding non-LTE correction to the abundance,

$$\Delta_{NLTE} = \log \varepsilon_{NLTE} - \log \varepsilon_{LTE} \qquad (1)$$

is explored in detail in [11] for a broad range of stellar temperatures ($T_{eff} = 4000$–$10\,000$ K), surface gravities ($\log g = 0.0$–4.5), and metallicities ([M/H] $= -2.0$–0.0). The non-LTE abundance correction Δ_{NLTE} determined from the KI λ7699 Å resonance line is appreciable ($|\Delta_{NLTE}| > 0.2$ dex) for all stars of spectral types from A to K, including the Sun. At the same time, a considerable (by a factor of 2.5) increase of $|\Delta_{NLTE}|$ is observed with increasing stellar luminosity, and this quantity also changes rapidly with increasing effective temperature. Therefore, even differential methods for analyzing the LTE potassium abundances within a narrow range of spectral types do not ensure the absence of errors of up to 0.2 dex or more.

The discovery of strong non-LTE effects for the KI atom has suggested the necessity of reanalyzing the potassium abundances in the atmospheres of late-type stars without assuming LTE. Such an analysis was carried out by Takeda *et al.* [12] for some stars from the Chen *et al.* [3] and Gratton and Sneden [2] samples. Overall, the derived [K/Fe] ratios were in agreement with the theoretical predictions of [8], providing evidence in favor of the hypothesis that the potassium was synthesized during explosive oxygen burning. However, individual values of [K/Fe] for some disk stars show substantial deviations from the general dependence, Δ[K/Fe] ~ 0.15 dex, reaching Δ[K/Fe] ~ 0.3 dex for halo stars. These deviations could be explained in several ways.

(1) The observational data used were obtained on different detectors: RETICON arrays [2] and CCD detectors [3]. Bikmaev *et al.* [13] have shown that the impossibility of correctly taking into account the scattering of light in classical spectrographs with RETICON arrays results in the systematic underestimation of line equivalent widths, reaching 10% in some cases.

(2) Another factor is the possible neglect of telluric lines in the reduction of the spectra. Telluric lines of O_2 in the interval λ7695–7704 Å can have equivalent widths up to $W_\lambda = 10$ mÅ , and their intensities in halo stars are comparable to the intensity of the line under investigation, KI λ7699 Å. Therefore, the important problem of correctly removing O_2 lines from the observed spectra arises during analyses of potassium abundances; we describe a procedure for this below.

(3) The stellar-atmosphere parameters used by Takeda *et al.* [12] were taken directly from [1] and [3]; i.e., they were derived using different methods, which could lead to a systematic shift of the potassium abundances between the two samples. Moreover, the estimates of the iron abundance and microturbulence velocity based on an analysis of FeI lines performed in [3] yielded values of ξ_{turb} that exceeded estimates obtained in other studies by 25–35%. In particular, $\xi_{turb} = 1.4$ km/s was derived for the Sun, while most estimates give $\xi_{turb} = 0.8$–1.0 km/s.

Therefore, we have reanalyzed the potassium abundances of Galactic disk stars taking into account non-LTE effects. In our analyses, we have mainly used our own echelle-spectrograph and CCD observations. To broaden the range of metallicities in the sample, we included stars from [4, 12] for which observations were obtained using CCD detectors. We redetermined the atmospheric parameters of most of the objects in accordance with commonly used methods; for the remaining stars, we adopted parameters found by another authors using similar methods. The resulting potassium abundances were computed via non-LTE modeling of the KI equilibrium states and line profiles, which had been tested earlier in an analysis of the solar spectrum [11]. The main aims of our study were as follows:

(1) Comparing the potassium abundances in the atmospheres of stars of solar metallicity and the Sun;

(2) Analyzing the [K/Fe]–[Fe/H] dependence for Galactic disk stars and selecting a preferred mechanism for the synthesis of potassium during the formation of these stars;

(3) Investigating the influence of deviations from LTE on the potassium abundances derived in differential analyses.

In Section 2, we describe the observational data used and the measurements of the KI λ7699 Å equivalent widths, and compare the data taken from different sources. In Section 3, we derive more accurate atmospheric parameters of the stars, estimate their possible errors, and investigate the accuracy of the methods we use. Section 4 briefly describes the method used in the non-LTE computations of the equilibrium level populations for KI and the profiles of the KI λ7699 Å line. In Section 5, we analyze the dependence of the non-LTE corrections on T_{eff}, $\log g$, and [Fe/H], as well as the influence of deviations from LTE on the derived potassium abundances and the errors due to uncertainties in the adopted atmospheric parameters. Further, we present the observed [K/Fe]–[Fe/H] dependences derived in LTE and non-LTE models and compare them with theoretical predictions of models for the chemical evolution of the Galaxy. Finally, we summarize our conclusions about the dominant mechanism for the synthesis of potassium during the formation of Galactic-disk stars.

2. OBSERVATIONAL DATA

We used high-quality observational data obtained using CCD detectors.

(1) The spectra of 19 solar-type stars were obtained on the 2-m Zeiss-2000 telescope of the Terskol Observatory (Northern Caucasus) and the 1-m Zeiss-1000 telescope of the Special Astrophysical Observatory of the Russian Academy of Sciences, using the MAESTRO [14] and GEGS [15] Coudé–echelle spectrometers. A WI 1242×1152 CCD with a pixel size of 22.5 × 22.5 microns was used as a detector. The average resolution of the spectra is of the order of $\lambda/\Delta\lambda = 45\,000$ and the signal-to-noise ratio near λ7699 Å reaches $S/N = 200$ due to the good sensitivity of the CCD detectors. Spectra of HD 61421, HD 142860, and HD 217014 were obtained in January and July 1996, of 14 of the sample stars in July–August 1998, and of HD 213575 and HD 225239 in September and October 1999. Solar spectra scattered in the Earth's atmosphere were obtained during every observing run. Most of the stars are investigated as part of a study of the chemical composition of photometric analogs of the Sun [16]. The preliminary reduction of the echelle spectra, including extraction of the CCD images, normalization, wavelength calibration, and measurement of the line equivalent widths was carried out using the DECH20 program package [17]. The measured equivalent widths of the KI λ7699 Å line are listed in Table 3, and the observed spectra of several stars in the range $\Delta\lambda$7697–7702 Å are shown in Fig. 1. Comparison of the derived W_λ values for the potassium line in several solar spectra and in the spectrum of Procyon shows that their mean error is $\Delta W_\lambda = \pm 4$ mÅ.

The stars studied have various topocentric radial velocities, so that their atmospheric KI λ7699 Å lines experience Doppler shifts relative to the nearby $\lambda\lambda$7695, 7697, 7702, and 7704 Å oxygen telluric lines. This is clearly visible in Fig. 1, where we have shifted the observed spectra along the horizontal axis to bring the position of the potassium line into agreement with the laboratory value. As a result, in some cases, the KI λ7699 Å line can overlap with the O_2 lines, which can have various intensities up to $W_\lambda = 10$ mÅ, depending on the observing conditions. For this reason, we must pay special attention to the correct exclusion of blending with telluric lines in measurements of the potassium-line equivalent widths. An example of such a procedure is shown in Fig. 2, for the spectra of HD 6582 and the hot comparison star HD 120315. The intensities of the $\lambda\lambda$7697, 7702, and 7704 Å telluric lines are comparable in both spectra, enabling us to reconstruct the intrinsic profile of the potassium line (Fig. 2) by applying the "removal of telluric lines" option of the DECH20 package [17]. Subsequent measurements of its equivalent width via direct integration and Gaussian fitting show that the results agree to within $\Delta W_\lambda = \pm 3$ mÅ.

(2) We used the data of Tomkin *et al.* [4] for six dwarfs with enhanced metallicities. The values W_{tomk} were measured by Tomkin *et al.* from spectra with $\lambda/\Delta\lambda = 60\,000$ and $S/N \simeq 400$ obtained by the Coudé–echelle spectrograph and Tek–CCD camera of the 2.7-m telescope of the McDonald Observatory.

(3) We selected eight dwarfs with moderate metal deficiencies from the sample of Takeda *et al.* [12], who derived the values W_{take} from spectra obtained by Chen *et al.* [3] with the Coudé–echelle spectrograph and Tek–CCD of the 2.16-m telescope of the Beijing Astronomical Observatory. These spectra have $\lambda/\Delta\lambda \simeq 40\,000$ and $S/N = 150$–300 in the interval $\Delta\lambda = 7692$–7722 Å. Takeda *et al.* [12] show that the equivalent widths of the KI λ7699 Å line derived in [12] and in [3] agree to within 2%.

In total, we derived potassium abundances for 33 stars. The list of objects studied is given in Table 1.

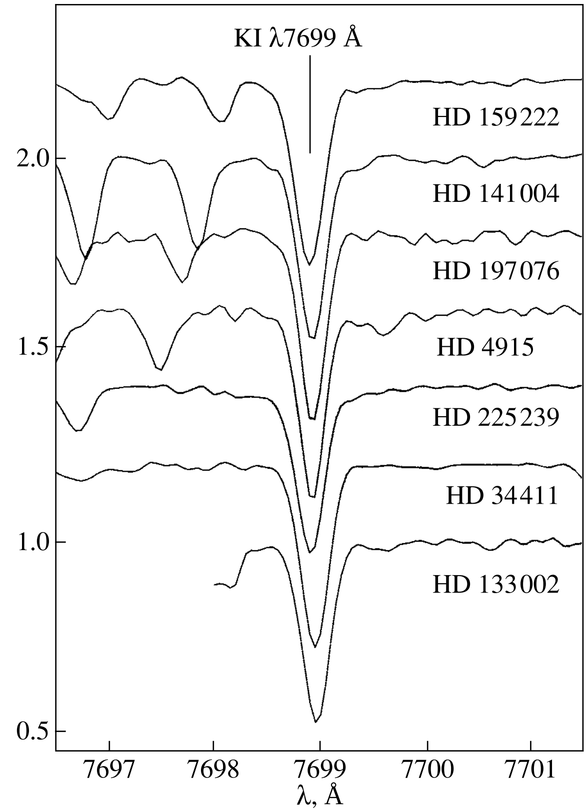

Fig. 1. Normalized spectra of several observed stars near the λ7699Å line. The spectra have been successively shifted along the vertical axis by 0.2.

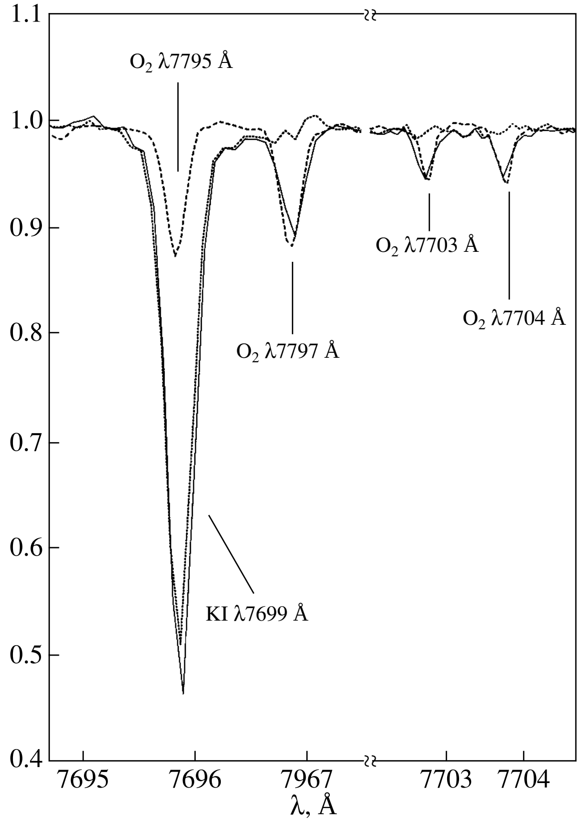

Fig. 2. Removal of telluric lines. The observed spectra of HD 6582 and HD 120315 are shown by solid and dashed curves, respectively. The dotted curve shows the corrected spectrum of HD 6582.

To expose possible systematic differences between the data of different authors and estimate the random measurement errors, we compared the equivalent widths of lines of various elements in the spectra of the three stars common to the samples [3, 4, 16] (Fig. 3). The regression equations relating the data of Galeev *et al.* [16] (W_{gale}), Chen *et al.* [3] (W_{chen}), and Tomkin *et al.* [4] (W_{tomk}) have the form

$$W_{chen} = 1.019W_{gale} - 2.4\ \text{mÅ} \pm 4.2\ \text{mÅ}$$
$$\text{for HD 10307},$$

$$W_{chen} = 1.012W_{gale} - 0.6\ \text{mÅ} \pm 3.4\ \text{mÅ}$$
$$\text{for HD 34411},$$

$$W_{tomk} = 0.974W_{gale} + 1.0\ \text{mÅ} \pm 3.2\ \text{mÅ}$$
$$\text{for HD 217014}.$$

These dependences show that there are no systematic differences between the data of [3, 4, 16] exceeding the 2% level, with the dispersion being within 4 mÅ. The estimates of the differences between W_{gale}, W_{chen}, and W_{tomk} are lower than the possible errors of individual measurements of W_λ for the KI λ7699 Å line, enabling us to use the data of [3, 4, 16] in a joint analysis.

3. DETERMINATION OF STELLAR ATMOSPHERIC PARAMETERS

The accuracy of the elemental abundances depends not only on the correctness of the observing method and the theory of line formation in stellar atmospheres that is used, but also on the accuracy of the adopted fundamental parameters of the stars. Therefore, we refined the atmospheric parameters of the stars using the methods described below. The values of T_{eff} and/or $\log g$ and [Fe/H] were determined for 23 stars. The parameters of the remaining stars were taken from [18–21].

Table 1 lists the effective temperatures T_{eff}, surface gravities $\log g$, microturbulence velocities ξ_{turb}, and masses M for the 33 stars, together with the number of lines of ionized iron N(FeII) used for the analyses. The superscripts indicate stars for which parameters were taken from the papers listed above. The absence of a superscript by a parameter or star number means that the parameters were derived in the present paper.

Table 1. Atmospheric parameters of the stars

HD	T_{eff}, K	$\log g$	[Fe/H] $\pm\sigma$, dex	ξ_{turb} $\pm\sigma$, km/s	M, $M_\odot$	N (FeII)	HD	T_{eff}, K	$\log g$	[Fe/H] $\pm\sigma$,dex	ξ_{turb} $\pm\sigma$, km/s	M, $M_\odot$	N FeII
4307	5740	3.97	−0.19	0.9	1.09	11	142373^2	5840	3.84	−0.57	1.3		
			0.07	0.2			142860^4	6254	4.02	−0.19	1.4		
4915	5640	4.46	−0.38	0.8	0.83	7	146233	5790	4.39	0.03	0.8	1.00	10
			0.08	0.5						0.03	0.2		
6582	5310	4.47	−1.02	0.9	0.71	6	159222	5870	4.41	0.12	1.1	1.07	7
			0.06	0.3						0.05	0.4		
9562	5865	3.96	0.16	1.2	1.21	8	186408	5780	4.21	0.01	1.0	0.99	10
			0.05	0.2						0.08	0.2		
10307	5870^1	4.34	0.06	0.9	1.06	10	186427	5760	4.31	0.03	0.9	0.97	23
			0.05	0.2						0.08	0.2		
19373^2	5970	4.15	0.03	1.2			187923	5780	4.10	−0.17	1.0	1.05	10
			0.05	0.2						0.08	0.2		
34411	5880	4.22	0.05	1.0	1.05	11				0.05	0.2		
			0.06	0.3			197076	5830	4.45	−0.05	0.8	1.05	9
55575^2	5890	4.25	−0.36	1.0						0.04	0.2		
60319^3	5930	4.23	−0.89	1.2	0.88	6	199960	5980	4.26	0.26	1.1	1.15	8
			0.01	0.1						0.04	0.3		
61421^4	6470	4.01	0.01	1.9			201891^3	5910	4.30	−1.05	1.2	0.83	3
62301^2	5938	4.06	−0.69	1.3						0.01	0.1		
67228	5850^2	3.98	0.12	1.2	1.18	6	208906^2	6030	4.35	−0.64	1.2		
			0.04	0.2			210855	6310	3.82	0.08	1.7	1.51	5
86728	5810	4.33	0.24	0.8	1.07	7				0.03	0.1		
			0.04	0.2			213575	5680	4.13	−0.23	1.2	0.98	11
88986	5810	4.12	0.04	1.0	1.10	8				0.07	0.2		
			0.02	0.2			217014	5793^4	4.37	0.22	1.0	1.16	18
106516^3	6210	4.32	−0.78	1.5	0.89	6				0.05	0.2		
			0.02	0.1			222143	5800	4.42	0.04	0.8	1.03	7
133002	5570	3.58	−0.52	1.5	1.53	19				0.07	0.2		
			0.08	0.3			225239	5500	3.74	−0.43	1.3	1.14	21
141004	5940	4.21	0.00	0.9	1.08	8				0.08	0.2		
			0.05	0.2									

Note: In the column "T_{eff}," the superscripts 1 and 2 denote data from [18] and [19], respectively. The superscript by the number of a star denotes the source of the atmospheric parameters: [19] (2), [20] (3), and [21] (4). The absence of a superscript by a parameter or number of a star means that the corresponding parameters were derived in this paper.

3.1. Effective Temperature

We derived the effective temperatures for 20 of the stars using the $V-K$ and $V-R$ versus T_{eff} color-index calibrations of Alonso *et al.* [22]. The various color-index calibrations of [22] (using $B-V$, $R-I$, $V-R$, $V-I$, $V-K$, $J-H$, $J-K$, and $ubve$-β) are based on the T_{eff} values derived by Alonso *et al.* [18] using the infrared-flux method and the grid of LTE model atmospheres of Kurucz [23]. The photometric V and R magnitudes (for 12 stars) were taken from [24], and the K magnitudes (for 8 stars) were taken from [25].

The temperatures of three stars were derived in a similar way by one of us (N. N. Shimanskaya) in an earlier paper [20] using $V-K$. The T_{eff} for HD 10307 derived using the infrared-flux method was adopted in accordance with [18]. The effective temperatures for nine stars were derived by Fuhrmann [19, 21] based on the profiles of their Balmer lines.

For eight stars, we compared the T_{eff} values derived using $V-K$ and $V-R$ (T_{VK} and T_{VR}). The T_{VR} values are somewhat higher than the T_{VK} values, with the average difference being $\overline{T_{VK}-T_{VR}} = -40$ K. We also carried out a similar temperature comparison for a sample of 60 dwarfs with various metallicities and $T_{eff} = 5300$–6800 K, for which $\overline{T_{VK}-T_{VR}} = -3 \pm 60$ K. We compared the spectroscopic and photometric (color) temperatures for the 15 stars that are common to the samples [19, 21] and our own sample. The T_{eff} values of all but three of the stars are confined to the narrow range 5780–5940 K. Therefore, it is not possible to firmly conclude whether or not there exists a $T_{\rm color} - (T_{\rm spect} - T_{\rm color})$ dependence, as was suggested, for example, in [20]. The average differences of the temperatures derived using the two methods are $\overline{T_{\rm color} - T_{\rm spectrum}} = 30 \pm 50$ K. Thus, the mean errors of the temperature estimates based on different color indices ($V-K$, $V-R$) or different methods do not exceed 60 K.

3.2. Surface Gravity log g

We derived the parameter $\log g$ for 23 stars from the relation

$$\log\frac{g}{g_\odot} = \log\frac{M}{M_\odot} + 4\log\frac{T_{eff}}{T_{eff\odot}} + 0.4V_0 \qquad (2)$$
$$+\,0.4\mathrm{BC} + 2\log\pi + 0.12$$

using the parallaxes π from the HIPPARCOS catalog [26]. The bolometric corrections were taken from the paper of Bergbusch and Van der Berg [27]. The masses of the stars M were derived from the theoretical evolutionary tracks of Girardi *et al.* [28], which were computed for a wide range of Z from 0.030 to 0.0004, which corresponds to metallicities $[M/\mathrm{H}] = +0.2\ldots-1.7$. The resulting values of $\log g$ are in the range $3.6 < \log g < 4.5$. The errors in $\log g$ are determined by the errors in π, T_{eff}, and M, and do not exceed 0.2 dex.

The surface gravities of three stars determined using this same method were taken from [20]. Values of $\log g$ for the remaining stars derived using the wings of the MgI $\lambda\lambda$5172, 5183 Å lines were taken from [19, 21]. Comparisons of the $\log g$ values derived from line profiles and from (2) made in [19, 21] and by us for the 15 stars in common with similar T_{eff} values indicates an absence of systematic differences, with the random errors being no more than 0.06 dex, within the limits of the accuracy in the surface gravity.

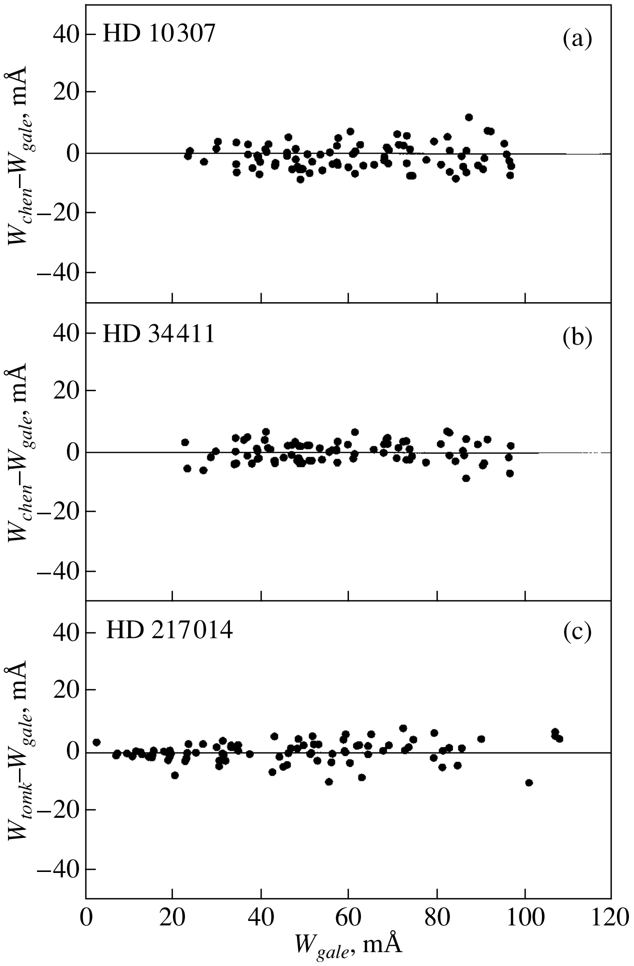

Fig. 3. Comparison of observed line equivalent widths for stars common to the studies of (a) Galeev *et al.* [16] (W_{gale}), (b) Chen *et al.* [3] (W_{chen}), and (c) Tomkin *et al.* [4] (W_{tomk}).

3.3. Iron Abundance and Microturbulence Velocity

The iron abundance [Fe/H] and microturbulence velocity ξ_{turb} were derived for 23 stars from the equivalent widths of FeII lines. Table 2 gives a list of the thirty lines used. For most of the lines, values of $f_{ij}\varepsilon_\odot(\mathrm{Fe})$ and the van der Waals broadening constant C_6 refined using the Solar Flux Atlas [34] were taken from [20]. In [20], the values of f_{ij} were derived for a fixed iron abundance ($\log \varepsilon_{\odot}(\mathrm{Fe}) = 7.51$, in accordance with [35]). The computations were based on the LTE solar-atmosphere model from the grid of Kurucz [23]. The solar microturbulence velocity was assumed to be 0.8 km/s. With the aim of refining the atomic parameters, we carried out additional computations for nine FeII lines using a similar method. Table 2 lists the empirically refined oscillator strengths and correction factors for C_6 ($\Delta \log C_6$). For comparison, we also give experimental values of $\log_i f_{ij}(\mathrm{exp})$ and data from the VALD [29] database. We can see that, with the exception of a few lines, our values of $\log g_i f_{ij}(\mathrm{prof})$ are in good agreement with these data.

We determined the metallicities of the stars using equivalent widths of the FeII lines taken from the sources listed above in the description of the observational data used. Table 1 gives the values of [Fe/H] and ξ_{turb} together with the dispersion σ and the number of ionized-iron lines used N(FeII). The errors in the iron abundances do not exceed 0.08 dex, and the errors in ξ_{turb} are, on average, 0.2 km/s.

For three stars, the iron abundance [Fe/H] and microturbulence velocity computed using the above method were taken from [20]. For the remaining stars, these parameters were derived in [19, 21], based on analyses of the profiles of three FeII lines; the corresponding estimates of the errors in [Fe/H] and ξ_{turb} do not exceed 0.09 dex and 0.2 km/s.

4. METHOD OF THE NON-LTE COMPUTATIONS

We determined the potassium abundances using the method for computing equilibrium states of the KI atom developed in [11]. This method includes a 36-level atomic model for KI that yields accurate results for the atmospheres of stars with $T_{eff} =$ 2000–15 000 K, and a set of atomic parameters for the observed lines that was refined during an analysis of the Solar Flux Atlas of Kurucz [34]. Only one strong resonance line (KI λ7699 Å) and two weak subordinate lines (K $\lambda\lambda$5801, 6938 Å) with an equivalent width less than 5 mÅ were observed in the spectra of our sample stars. We derived the potassium abundances using the λ7699 Å line only, since other lines are in different spectral ranges, are located on another part of the curve of growth, and may have substantial relative errors W_{λ}. We adopted the atomic parameters of the λ7699 Å line $\log g_i f_{ij} = -0.169$, $\gamma_R = 3.663 \times 10^{-7}$, and $\log C_6(\mathrm{prof.}) = 29.30$. The computations of the non-LTE level populations and equivalent widths were carried out using the NONLTE3 program package developed by Sakhibullin [36], which implements a complete linearization method as realized by Auer and Heasley [37]. The computations of the absorption coefficients took into account all continuum opacity sources at all frequencies, about 530 000 of the strongest lines at wavelengths $\lambda > 912$ Å from the lists of Kurucz [23], and the main molecular bands according to the theory of Nersisyan *et al.* [38] (these last data were kindly provided by Ya. V. Pavlenko of the Main Astronomical Observatory of the National Academy of Sciences of the Ukraine).

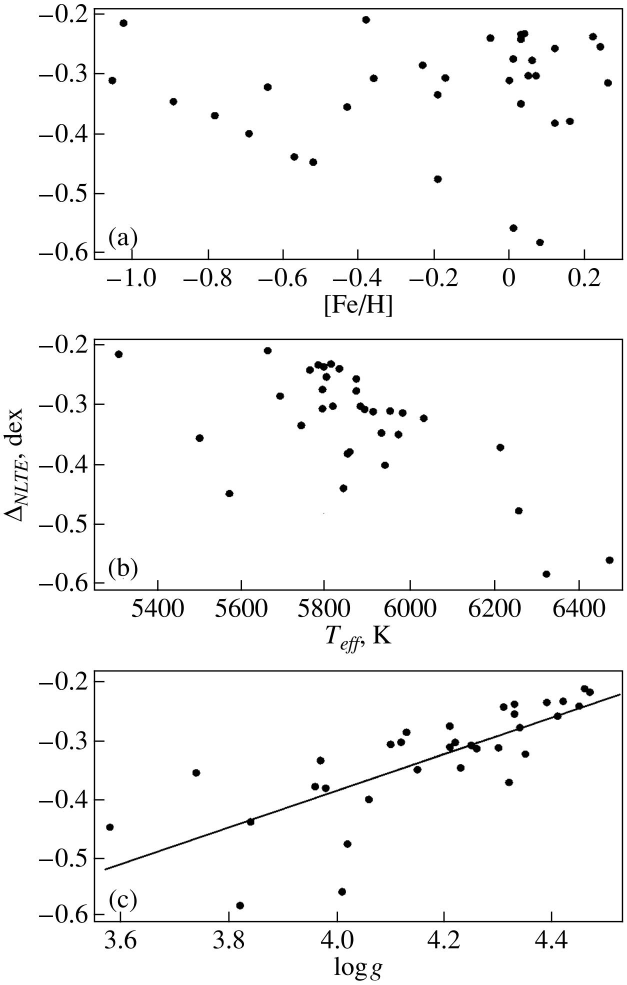

Fig. 4. Dependences of non-LTE corrections Δ_{NLTE} for our sample stars on (a) metallicity [Fe/H], (b) effective temperature T_{eff}, and (c) surface gravity $\log g$.

All the potassium abundances for our sample stars were computed using the grids of blanketed model atmospheres of Kurucz [23]. Model atmospheres with parameters outside the grids were computed using the interpolation procedure developed in [39, 40], which provides accuracies of the electron temperature and gas pressure no worse than 1%. The solar potassium abundances obtained using different model atmospheres differ by up to a factor of 0.09 dex [11].

Table 2. Atomic parameters of the FeII line used to determine the metallicities and microturbulence velocities

λ, Å	E_i, eV	$\log g_i f_{ij}$				$\Delta \log C_6$
		prof	exp	refs.	VALD [29]	
4178.86	2.58	−2.51	−2.48	[30]	−2.50	0.38
4416.82	2.78	−2.54	−2.54	[31]	−2.41	0.26
4491.40	2.85	−2.70	−2.70	[30]	−2.70	0.22
4508.28	2.85	−2.29	−2.33	[31]	−2.25	0.31
4515.34	2.84	−2.42	−2.41	[30]	−2.45	0.34
4520.23	2.81	−2.54	−2.55	[31]	−2.60	0.38
4576.33	2.84	−2.83	−2.90	[32]	−2.92	0.38
4620.52	2.83	−3.17	−3.19	[32]	−3.24	0.26
4923.93	2.89	−1.28	−1.24	[30]	−1.32	0.34
5100.66	2.81	−4.12			−4.17	0.26
5132.67	2.81	−3.96			−3.98	0.26
5136.80	2.84	−4.30			−4.29	0.17
5197.57	3.23	−2.18	−2.10	[30]	−2.10	0.22
5234.63	3.22	−2.19	−2.22	[32]	−2.23	0.76
5256.93	2.89	−4.10				0.12
5264.81	3.33	−3.03	−3.27	[33]	−3.12	0.42
5325.56	3.22	−3.11	−2.60	[30]	−3.12	0.22
5414.07	3.22	−3.54	−3.58	[33]	−3.54	0.67
5425.26	3.20	−3.16			−3.16	0.31
5991.38	3.15	−3.47			−3.54	0.62
6084.11	3.20	−3.75			−3.78	0.30
6149.25	3.89	−2.67			−2.72	0.12
6247.56	3.89	−2.24			−2.31	0.22
6369.46	2.89	−4.09	−3.55	[33]	−4.16	0.22
6383.72	5.55	−2.15			−2.07	0.26
6416.93	3.89	−2.58			−2.65	0.38
6432.68	2.89	−3.53	−3.51	[32]	−3.52	0.26
6456.39	3.90	−2.00			−2.07	0.51
6516.09	2.89	−3.19	−3.44	[33]	−3.32	0.34
7515.84	3.90	−3.39	−3.41	[33]	−3.46	0.17

Note: The values of $\log g_i f_{ij}$(prof) and $\Delta \log C_6$ were obtained by analyzing the profiles of solar lines. The fifth column gives references to the experimental determinations of the oscillator strengths of the FeII lines.

However, differential analyses of stellar relative to solar potassium abundances reduce the differences due to the structure of the model atmosphere to 0.01 dex.

The initial solar abundance $\log \varepsilon_\odot(\mathrm{K}) = 5.12$ used for the computations of the equilibrium states of the KI atom was adopted in accordance with the data of [35], which were confirmed by the results of the non-

Table 3. Non-LTE and LTE $\log\varepsilon$(K) values and their errors σ, [K/Fe] ratios, and the non-LTE corrections Δ_{NLTE}. (Results are grouped according to observations by different authors)

HD	[Fe/H]	W_χ	LTE			Non-LTE			Δ_{NLTE}, dex
		mÅ	$\log\varepsilon$	[K/Fe]	σ	$\log\varepsilon$	[K/Fe]	σ	
This paper									
Sun	0.00	173.0	5.33	0.00		5.11	0.00		−0.22
6582	−1.02	164.4	4.58	0.27	0.09	4.36	0.27	0.08	−0.22
61421	0.01	155.2	5.72	0.38	0.09	5.16	0.04	0.06	−0.56
142860	−0.19	144.0	5.56	0.42	0.08	5.08	0.16	0.06	−0.48
213575	−0.23	176.5	5.31	0.21	0.08	5.02	0.14	0.06	−0.29
217014	0.22	185.0	5.48	−0.07	0.08	5.24	−0.09	0.06	−0.24
225239	−0.43	158.0	5.11	0.21	0.08	4.75	0.07	0.06	−0.36
Galeev *et al.* [16]									
4307	−0.19	151.5	5.31	0.17	0.08	4.98	0.06	0.06	−0.33
4915	−0.38	156.1	5.02	0.07	0.07	4.81	0.08	0.06	−0.21
10307	0.06	170.2	5.47	0.08	0.07	5.19	0.02	0.06	−0.28
34411	0.05	158.5	5.38	−0.00	0.07	5.07	−0.09	0.06	−0.31
133002	−0.52	158.9	5.18	0.37	0.08	4.73	0.14	0.08	−0.45
141004	0.00	154.1	5.42	0.09	0.07	5.11	0.00	0.06	−0.31
146233	0.03	166.1	5.30	−0.06	0.07	5.07	−0.07	0.06	−0.23
159222	0.12	175.4	5.42	−0.03	0.09	5.16	−0.07	0.08	−0.26
186408	0.01	171.3	5.40	0.06	0.07	5.12	0.00	0.06	−0.28
186427	0.03	175.1	5.37	0.01	0.08	5.13	−0.01	0.06	−0.24
187923	−0.17	169.4	5.40	0.24	0.08	5.09	0.15	0.06	−0.31
197076	−0.05	155.6	5.27	−0.01	0.07	5.02	−0.04	0.06	−0.25
222143	0.04	169.2	5.34	−0.03	0.10	5.11	−0.04	0.06	−0.23
Takeda *et al.* [12]									
19373	0.03	165.9	5.51	0.15	0.09	5.16	0.02	0.07	−0.35
55575	−0.36	141.7	5.19	0.22	0.07	4.88	0.13	0.05	−0.31
62301	−0.69	126.9	5.09	0.45	0.09	4.69	0.27	0.06	−0.40
60319	−0.89	117.2	4.92	0.48	0.08	4.57	0.35	0.06	−0.35
106516	−0.78	112.6	5.03	0.48	0.09	4.65	0.32	0.05	−0.38
142373	−0.57	137.9	5.19	0.43	0.09	4.75	0.21	0.06	−0.44
201891	−1.05	101.4	4.73	0.45	0.08	4.41	0.35	0.06	−0.32
208906	−0.64	112.5	4.93	0.24	0.08	4.60	0.13	0.06	−0.33
Tomkin *et al.* [4]									
9562	0.16	169.0	5.54	0.05	0.09	5.16	−0.11	0.07	−0.38
67228	0.12	168.0	5.52	0.07	0.09	5.14	−0.09	0.08	−0.38
86728	0.24	170.0	5.42	−0.15	0.08	5.16	−0.19	0.07	−0.26
88986	0.04	160.0	5.39	0.02	0.08	5.08	−0.07	0.07	−0.31
199960	0.26	168.0	5.54	−0.05	0.08	5.22	−0.15	0.07	−0.32
210855	0.08	159.0	5.76	0.35	0.08	5.17	−0.02	0.07	−0.59

Table 4. Errors in $\log\varepsilon$ determined by uncertainties in atmospheric parameters

HD	Non-LTE				LTE			
	$\sigma(T_{eff})$	$\sigma(\log g)$	$\sigma(\xi_{turb})$	σ	$\sigma(T_{eff})$	$\sigma(\log g)$	$\sigma(\xi_{turb})$	σ
4915	0.04	0.03	0.02	0.06	0.06	0.04	0.02	0.07
6582	0.06	0.03	0.03	0.08	0.08	0.05	0.03	0.09
34411	0.04	0.02	0.04	0.06	0.06	0.04	0.03	0.07
61421	0.04	0.01	0.05	0.06	0.03	0.06	0.05	0.09
106516	0.04	0.01	0.03	0.05	0.05	0.06	0.04	0.09
133002	0.04	0.01	0.06	0.08	0.05	0.04	0.04	0.08
142860	0.03	0.01	0.05	0.06	0.06	0.04	0.04	0.08
146233	0.04	0.02	0.03	0.06	0.05	0.04	0.02	0.07
199960	0.04	0.03	0.05	0.07	0.05	0.06	0.03	0.08
217014	0.04	0.03	0.04	0.06	0.05	0.05	0.04	0.08

LTE analysis [10, 11] of the Solar Flux Atlas [34]. In the computations for stars with nonsolar chemical compositions, the initial potassium abundance was varied in proportion to the metallicity. For several stars with resultant abundances that differed from the initial abundances by 0.2 dex or more, we repeated the non-LTE computations with a corrected value of $\log\varepsilon$(K).

5. ANALYSIS OF RESULTS

5.1. Non-LTE and LTE Potassium Abundances

The resulting non-LTE and LTE abundances $\log\varepsilon$(K) are given in Table 3, and estimates of possible errors introduced by inaccuracies in the atmospheric parameters are listed in Table 4. The errors (σ) were calculated assuming that the average uncertainties in the effective temperature, surface gravity, and microturbulence velocity were $\Delta T_{eff} = 60$ K, $\Delta\log g = 0.2$, and $\Delta\xi_{turb} = 0.2$ km/s. The influence of the adopted metallicity on the $\log\varepsilon$(K) values obtained does not exceed 0.01 dex for all the stars. In the LTE approximation, as a rule, the main errors in the potassium abundances are determined by uncertainties in T_{eff} and $\log g$, while the influence of ξ_{turb} is not significant. The average σ for our sample in the LTE approximation is 0.08 dex; HD 6582 and HD 222143 have upper limits of $\sigma = 0.10$ dex. If deviations from LTE are taken into account, the dependence of the computed abundances on the stellar temperatures becomes weaker by 20–35%, and the dependence on the surface gravity becomes weaker by a factor of 1.8 to 2.7. On the contrary, the influence of ξ_{turb} on $\log\varepsilon$(K) increases substantially and, in most cases, becomes larger than the influence of the other parameters. On the average, the non-LTE potassium abundances exhibit the following dependences on the atmospheric parameters:

$$\Delta T_{eff} = +60K \rightarrow \Delta\log\varepsilon_{NLTE}(\text{K}) = +0.04\ \text{dex},$$

$$\Delta\log g = +0.2 \rightarrow \Delta\log\varepsilon_{NLTE}(\text{K}) = -0.02\ \text{dex},$$

$$\Delta\xi_{turb} = +0.2\ \text{km/s} \rightarrow \Delta\log\varepsilon_{NLTE}(\text{K}) = -0.04\ \text{dex}.$$

Thus, in the analyses of the non-LTE potassium abundances, special attention should be paid to accurate determination of T_{eff} and ξ_{turb}. On average for all the stars, allowance for non-LTE effects reduces the total random error by 25–30%, to $\sigma = 0.06$ dex.

The analysis of the non-LTE corrections Δ_{NLTE} given in Table 3 and in Fig. 4 leads us to the following conclusions.

(1) The non-LTE corrections for all the stars are negative, and their magnitudes exceed 0.20 dex, which implies possible errors in the abundance determinations of more than 3σ. The non-LTE corrections for our sample lie in the range $\Delta_{NLTE} = -0.21 - -0.59$ dex, with the average being $\overline{\Delta_{NLTE}} = -0.33$ dex.

(2) Non-LTE effects for the solar atmosphere constitute one of the smallest corrections to the abundances: $\Delta_{NLTE} = -0.22$ dex. As a result, the ratio

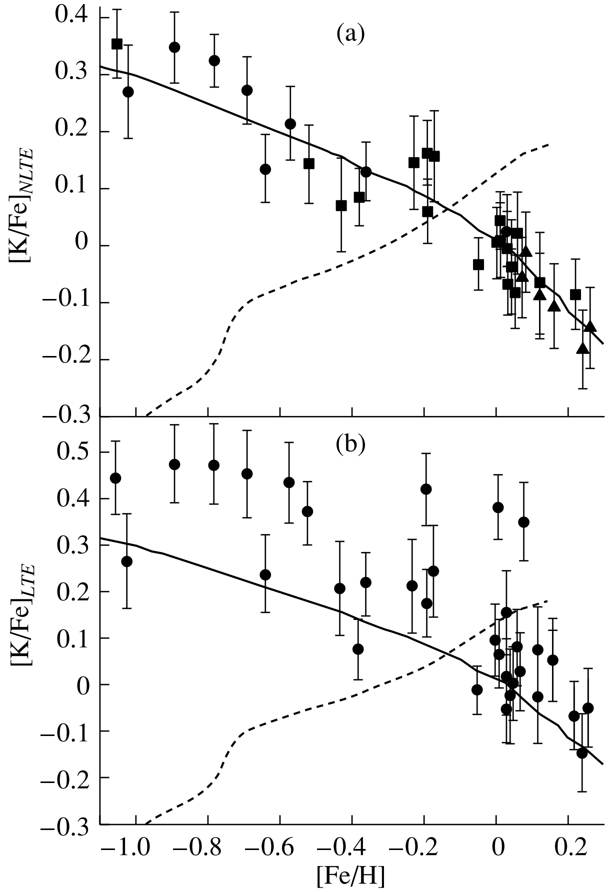

Fig. 5. Observed (a) non-LTE and (b) LTE [K/Fe] ratios as functions of the metallicity [Fe/H]. The squares show data from the present paper and Galeev *et al.* [16], the dots data from Takeda *et al.* [12], and the triangles data from Tomkin *et al.* [4]. The solid and dashed curves give the theoretical distributions according to Samland [8] and Alibes *et al.* [6].

$\overline{\text{[K/Fe]}}$ averaged over all the sample stars after correction for deviations from LTE is reduced by more than 0.1 dex.

(3) We did not find explicit dependences of Δ_{NLTE} on the metallicity (Fig. 4a) or the equivalent widths of the λ7699 Å line. However, as was shown in [11], such dependences are likely to appear as the metallicity decreases below [Fe/H] = −1.3 and the λ7699 Å line moves into the linear part of the curve of growth. Four stars with $T_{eff} > 6200$ K ($\overline{\Delta_{NLTE}} = -0.49$ dex) have large non-LTE corrections, but the influence of the temperature on Δ_{NLTE} is small for the remaining stars (Fig. 4b). At the same time, the $\Delta_{NLTE} - \log g$ trend that is evident Fig. 4c results in a substantial redistribution of the non-LTE potassium abundances, even among stars of the same spectral type.

Thus, determining the observed [K/Fe]–[Fe/H] dependence becomes possible only after taking into account non-LTE effects. This results both in a correction of the individual [K/Fe] ratios in the range from +0.01 dex to −0.40 dex and in a decrease in the average value $\overline{\text{[K/Fe]}}$ by −0.11 dex.

5.2. [K/Fe]–[Fe/H] dependence

The non-LTE and LTE ratios [K/Fe] derived by us are listed in Table 3, and their distribution as a function of metallicity is shown in Fig. 5. These relations were computed using the formula

$$[\text{K/Fe}] = (\log\varepsilon(\text{K}) - \log\varepsilon(\text{Fe})) - (\log\varepsilon_\odot(\text{K}) - \log\varepsilon_\odot(\text{Fe})) \quad (3)$$

using the solar value $\log\varepsilon_\odot(\text{K}) = 5.11$, derived from echelle spectra obtained in the present study (Table 3).

In addition, Fig. 5 shows the results of computations of the variations of [K/H] in Galactic-disk stars by Samland [8] (solid curve) and Alibes *et al.* [6] (dashed curve). Analysis of the derived [K/Fe]–[Fe/H] dependence leads to the following conclusions.

(1) For the ten stars with metallicities $-0.05 <$ [Fe/H] < 0.05, $\overline{\text{[K/Fe]}} = -0.01 \pm 0.04$ dex. This provides evidence that the solar potassium abundance is consistent with the average $\log\varepsilon(\text{K})$ for solar-metallicity stars, and confirms that we may use $\log\varepsilon_\odot(\text{K})$ as a standard. The value $\log\varepsilon_\odot(\text{K}) = 5.11 \pm 0.03$ we have derived coincides with the meteoritic value, $\log\varepsilon(\text{K}) = 5.12$ [35].

(2) The tendency for [K/Fe] to decrease with increasing metallicity dominated in all stages of formation of stars of the thick and thin disks with [Fe/H] > -1.0. The behavior of the [K/Fe]–[Fe/H] dependence varies from [K/Fe] $= 0.03 - 0.30 \times$ [Fe/H] for stars with metallicities $-1.0 <$ [Fe/H] < -0.3 to [K/Fe] $= -0.01 - 0.54 \times$ [Fe/H] for stars with [Fe/H] > -0.3. Approximation of this dependence by a second-order polynomial gives a curve that coincides within ±0.03 dex with the theoretical distribution obtained by Samland *et al.* [8] for a model with potassium synthesis during explosive oxygen burning in massive type II supernovae. According to [8], such supernovae are the end products of the evolution of stars with masses much higher than $10M_\odot$. Our [K/Fe]–[Fe/H] dependence clearly does not support the theoretical predictions of [5–7] (Fig. 5) based on the hypothesis that potassium is synthesized during hydrostatic oxygen burning. Therefore, we confirm the conclusion made earlier by Takeda *et al.* [12] for stars with moderate metal deficiencies that reactions

involving the explosive burning of ^{16}O dominate in the synthesis of ^{39}K nuclei.

(3) The individual values of [K/Fe] for 90% of the stars in our sample are consistent with the theoretical dependence [8] within the errors. This agreement, together with the fact that potassium and iron are synthesized in supernovae of various types, points toward a high efficiency of the mixing of matter in the Galaxy, which ensured homogeneity of the abundances of these elements in the interstellar medium during the formation of disk stars with $[\mathrm{Fe/H}] > -1.0$. Justification of this assertion requires more extensive studies of the abundances of potassium and other elements synthesized only during explosive oxygen burning in type II supernovae. Following [7, 8], such elements should include chlorine (Cl) and, possibly, vanadium (V), for both of which the volume of observational data is limited.

(4) Accurate determination of the [K/Fe]–[Fe/H] distribution is possible only after taking into account non-LTE effects. As Fig. 5b shows, in an LTE approximation, the dispersion of $\overline{[\mathrm{K/Fe}]}$ is about 0.15 dex (with an average of $\overline{[\mathrm{K/Fe}]} = 0.08$ dex), even for solar-metallicity stars. In the metallicity range $-1.0 < [\mathrm{Fe/H}] < -0.3$, the stars with the highest overabundances of potassium have the highest non-LTE corrections. As a result, the dispersion of [K/Fe] is increased in the LTE analysis, hindering the formulation of reliable conclusions about the [K/Fe]–[Fe/H] distribution. Thus, we do not confirm the conclusion of Takeda *et al.* [12] that the results of differential analyses of LTE potassium abundances are correct.

6. CONCLUSION

We have determined LTE and non-LTE potassium abundances for the atmospheres of 33 stars. The equivalent widths of the KI λ7699 Å resonant line were measured in the spectra of 20 stars observed by Galeev *et al.* [16]. The values of W_λ for 13 stars were adopted in accordance with the data of [3, 4], which used a similar system of equivalent widths. We determined the atmospheric parameters for most of the stars: T_{eff} from the $V-K$ and $V-R$ photometric color indices, $\log g$ using the astrometric parallaxes from the HIPPARCOS catalog, and [Fe/H] and ξ_{turb} from the W_λ values for FeII lines. The atmospheric parameters of the remaining stars had been found earlier using similar methods. The non-LTE abundances were computed using a 36-level atomic model for KI [11] that was developed and tested by us in an analysis of the observed solar spectrum using the NONLTE3 program package [36]. The results of our study lead us to the following conclusions.

(1) Deviations from LTE in the KI atom have a definitive influence on the resulting potassium abundances. The non-LTE corrections to the abundances for all our sample stars derived from the KI λ7699 Å line are negative; they vary in the range $\Delta_{NLTE} = -0.21...-0.59$ dex and depend on the surface gravity and effective temperature of the stars. One of the lowest corrections ($\Delta_{NLTE} = -0.22$ dex) is obtained for the solar atmosphere. This value decreases the average for the sample as a whole $\overline{[\mathrm{K/Fe}]}$ by more than -0.1 dex.

(2) The atmospheric potassium abundances for the Sun and ten stars with solar metallicities do not differ at the level of the abundance errors (0.03 dex).

(3) For all Galactic-disk stars with $[\mathrm{Fe/H}] > -1.0$, the ratio [K/Fe] decreases monotonically with increasing metallicity. Moreover, this tendency becomes stronger as the metallicity increases, from $\Delta[\mathrm{K/Fe}] = -0.30\Delta[\mathrm{Fe/H}]$ for $-1.0 < [\mathrm{Fe/H}] < -0.2$ to $\Delta[\mathrm{K/Fe}] = -0.54\Delta[\mathrm{Fe/H}]$ for $[\mathrm{Fe/H}] > -0.2$. This indicates a sharp decrease in the efficiency of the synthesis of potassium at the present epoch.

(4) Our [K/Fe]–[Fe/H] dependence is consistent with results of theoretical modeling of the synthesis of potassium during explosive oxygen burning in type II supernovae [8] (within $\Delta[\mathrm{K/Fe}] = \pm 0.04$ dex) and contradicts data obtained assuming potassium synthesis during hydrostatic oxygen burning [6, 7]. We thus confirm the dominance of explosive oxygen burning in potassium synthesis, concluded earlier in [3, 12] for stars with moderate metal deficiencies, for a wider range of metallicities of Galactic-disk stars, ($-1.0 < [\mathrm{Fe/H}] < 0.3$). At the same time, the non-LTE analyses of Takeda *et al.* [12] for six halo stars with $-2.0 < [\mathrm{Fe/H}] < -1.2$ show an average excess of potassium equal to 0.3 dex, with a scatter of $\Delta[\mathrm{K/Fe}] = 0.35$ dex. Hill *et al.* [41] derived $[\mathrm{K/Fe}] = 0.3$ taking into account the non-LTE corrections of [11] for the star CS 31082-001, with a metal underabundance of $[\mathrm{Fe/H}] = -2.9$. However, KI $\lambda\lambda$7665, 7699 Å lines were not detected in the spectra of two stars (CS 22949-037 and CD−38 245) with extremely low metal abundances (($[\mathrm{Fe/H}] \sim -4.0$)) [42], suggesting a deficiency of potassium by more than 0.1 dex. It is clear that the [K/Fe] values listed above do not enable us to draw firm conclusions on the form of the [K/Fe]–[Fe/H] dependence for halo stars and indicate the need for additional studies.

7. ACKNOWLEDGMENTS

The authors are sincerely grateful to L.I. Mashonkina and V.F. Suleimanov for useful advice and suggestions concerning the text of the paper. We are grateful to the staff members of the Terskol observatory for their multifaceted help with the observations. This work was supported by the Russian Foundation for Basic Research (project codes 02-02-17174 and 02-02-17423) and the Tatarstan Republican Academy of Sciences. V.V. Shimansky and A.I. Galeev express their special gratitude to the Russian Foundation for Basic Research for several IAU grants (project codes 01-02-06065, 02-02-06591, and 01-02-06068).

REFERENCES

1. R. G. Gratton and C. Sneden, Astron. Astrophys. **178**, 179 (1987).
2. R. G. Gratton and C. Sneden, Astron. Astrophys., Suppl. Ser. **68**, 193 (1987).
3. Y. Q. Chen, P. E. Nissen, G. Zhao, *et al.*, Astron. Astrophys., Suppl. Ser. **141**, 491 (2000).
4. J. Tomkin, B. Edvardsson, D. L. Lambert, and B. Gustafsson, Astron. Astrophys. **327**, 587 (1997).
5. P. X. Timmes, S. E. Wooskey, and T. A. Weaver, Astrophys. J., Suppl. Ser. **98**, 617 (1995).
6. A. Alibes, J. Labay, and R. Canal, Astron. Astrophys. **370**, 1103 (2001).
7. A. Goswami and N. Prantzos, Astron. Astrophys. **359**, 191 (2000).
8. M. Samland, Astrophys. J. **496**, 155 (1998).
9. J. H. Bruls, R. J. Rutten, and N. Shchukina, Astron. Astrophys. **265**, 237 (1992).
10. Y. Takeda, K. Kato, and Y. Watanabe, Publ. Astron. Soc. Jpn. **48**, 511 (1996).
11. D. V. Ivanova and V. V. Shimansky, Astron. Zh. **77**, 432 (2000) [Astron. Rep. **44**, 376 (2000)].
12. Y. Takeda, G. Zhao, Y.-Q. Chen, *et al.*, Publ. Astron. Soc. Jpn. **54**, 275 (2002).
13. I. F. Bikmaev, A. I. Galeev, G. A. Galazutdinov, and F. A. Musaev, Astron. Zh. (in press).
14. F. A. Musaev, G. A. Galazutdinov, A. V. Sergeev, *et al.*, Kinemat. Fiz. Neb. Tel **13**, 282 (1999).
15. F. A. Musaev, Pis'ma Astron. Zh. **22**, 795 (1996) [Astron. Lett. **22**, 715 (1996)].
16. A. Galeev, I. Bikmaev, F. Musaev, and G. Galazutdinov, *ASTROECO-2002 Abstract Book* (ASTROECO-2002, Terskol, 2002), p. 39.
17. G. A. Galazutdinov, Preprint No. 92, 1 (Spec. Astrophys. Obs., Nizhniĭ Arkhyz, 1992).
18. A. Alonso, S. Arribas, and C. Martínez-Roger, Astron. Astrophys., Suppl. Ser. **117**, 227 (1996).
19. J. Bernkopf, A. Fidler, and K. Fuhrmann, *Astrophysical Ages and Time Scales*, ASP Conf. Ser. **245** (Astron. Soc. Pacif., San Francisco, 2001), p. 207.
20. N. N. Shimanskaya and L. I. Mashonkina, Astron. Zh. **78**, 122 (2001) [Astron. Rep. **45**, 100 (2001)].
21. K. Fuhrmann, Astron. Astrophys. **338**, 161 (1998).
22. A. Alonso, S. Arribas, and C. Martínez-Roger, Astron. Astrophys. **313**, 873 (1996).
23. R. L. Kurucz, SAO CD-ROMs (MA0 2138, Cambridge, USA, 1994).
24. *Catalog of WBVR Magnitudes of Brightest Stars in the Northern Sky* [in Russian], Tr. Gos. Astronom. Inst. Shternberga, **LXIII**, 1991.
25. G. P. Di Benedetto, Astron. Astrophys. **339**, 858 (1998).
26. *The Hipparcos and Tycho Catalogues* (ESA SP-1200, 1997), p. 1.
27. P. A. Bergbusch and D. A. van der Berg, Astrophys. J., Suppl. Ser. **81**, 163 (1992).
28. L. Girardi, A. Bressan, G. Bertelli, and C. Chiosi, Astron. Astrophys., Suppl. Ser. **141**, 371 (2000).
29. F. Kupka, N. Piskunov, T. A. Ryabchikova, *et al.,* Astron. Astrophys., Suppl. Ser. **138**, 119 (1999).
30. S. Kroll and M. Kock, Astron. Astrophys., Suppl. Ser. **67**, 225 (1987).
31. J. Moity, Astron. Astrophys., Suppl. Ser. **52**, 37 (1983).
32. R. Schnabel, M. Kock, and H. Holweger, Astron. Astrophys. **342**, 610 (1999).
33. C. Hiese and M. Kock, Astron. Astrophys. **230**, 244 (1990).
34. R. L. Kurucz, I. Furenlid, J. Brault, and L. Testerman, *Solar Flux Atlas from 296 to 1300 nm* (Nat. Solar Obs., Sunspot, New Mexico, 1984).
35. N. Grevesse, A. Noels, and A. J. Sauval, *Cosmic Abundances,* ASP Conf. Ser. **99** (Astron. Soc. Pacif., San Francisco, 1996), p. 117.
36. N. A. Sakhibullin, Tr. Kazan. Astron. Obs. **48**, 9 (1983).
37. L. H. Auer and J. Heasley, Astrophys. J. **205**, 165 (1976).
38. S. E. Nersisyan, A. V. Shavrina, and A. A. Yaremchuk, Astrofizika **30**, 247 (1989).
39. V. F. Suleĭmanov, Pis'ma Astron. Zh. **22**, 107 (1996) [Astron. Lett. **22**, 92 (1996)].
40. N. A. Sakhibullin and V. V. Shimansky, Astron. Zh. **73**, 73 (1996) [Astron. Rep. **40**, 62 (1996)].
41. V. Hill, B. Plez, R. Cayrel, *et al.,* Astron. Astrophys. **387**, 560 (2002).
42. E. Depague, V. Hill, M. Spite, *et al.,* Astron. Astrophys. **290**, 187 (2002).

Translated by L. Yungel'son

Astronomy Reports, Vol. 47, No. 9, 2003, pp. 763–776. Translated from Astronomicheskiĭ Zhurnal, Vol. 80, No. 9, 2003, pp. 830–844.
Original Russian Text Copyright © 2003 by Shimansky, Borisov, Shimanskaya.

The Impact of Reflection Effects on the Parameters of the Old Pre-Cataclysmic Variables MS Peg and LM Com

V. V. Shimansky[1], **N. V. Borisov**[2], **and N. N. Shimanskaya**[1]

[1]*Kazan State University, ul. Lenina 18, Kazan, 420008 Tatarstan, Russia*
[2]*Special Astrophysical Observatory, Russian Academy of Sciences, Nizhniĭ Arkhyz, Karachaĭ-Cherkessian Republic, 357147 Russia*

Received December 11, 2002; in final form, March 14, 2003

Abstract—We have determined the main parameters of the old precataclysmic variable stars MS Peg and LM Com. The radial velocities of the components, reflection effects in the spectra, and light curves of the systems are studied based on model stellar atmospheres subject to external irradiation. Forty-seven moderate-resolution spectra for MS Peg and 57 for LM Com obtained with the 6-m telescope of the Special Astrophysical Observatory are used to derive the refined orbital periods of 0.1736660 days and 0.2586873 days, respectively; the orbital eccentricities do not exceed $e = 0.04$. The mass ($M_w = 0.49\,M_\odot$) and radius ($R_w = 0.015\,R_\odot$) of the MS Peg primary calculated using the gravitational redshift correspond to those for a cooling carbon white dwarf with a thin hydrogen envelope. The parameters of the red dwarf ($M_r = 0.19\,M_\odot$, $T_{eff} = 3560$ K, $R_r = 0.18\,R_\odot$) are close to those derived from evolutionary tracks for main-sequence M stars with solar chemical composition. The radius ($R_r = 0.22\,R_\odot$) and temperature ($T_{eff} = 3650$ K) of the LM Com secondary exceed theoretical estimates for main-sequence stars with masses of $M_r = 0.17\,M_\odot$. The luminosity excess of the red dwarf in LM Com can be explained by a prolonged ($T > 5 \times 10^6$ yrs) relaxation of the M star to its normal state after the binary leaves the common-envelope stage. For both systems, theoretical U, B, V, and R light curves and spectra calculated using the adopted sets of parameters are generally consistent with the observations. This confirms the radiative origin of the hot spots, the unimportance of horizontal radiative transport, and the absence of large-scale velocity fields with high values ($V_{trans} > 50$ km/s) at the surfaces of the secondaries. Most of the emission lines in the spectra of these objects are formed under conditions close to thermalization, enabling modeling of their profiles in an LTE approximation. A strong $\lambda3905$ Å emission line has been identified as the $3s^23p4s$ $1P^0$–$3s^23p^2$ $1S$ SiI $\lambda3905.52$ Å line formed in the atmosphere of the hot spot. The observed intensity can be explained by non-LTE "superionization" of SiI atoms by soft UV radiation from the white dwarf. We suggest a technique for identifying binaries whose cool components are subject to UV irradiation based on observations of $\lambda3905$ Å emission in their spectra. © *2003 MAIK "Nauka/Interperiodica"*.

1. INTRODUCTION

Pre-cataclysmic variables (PCVs) are detached binaries that consist of a white dwarf or hot, low-luminosity subdwarf paired with a late-type star [1]. The evolutionary status of PCVs is intermediate between systems with common envelopes and cataclysmic variables—a property that has led to growing interest in studies of these stars. Another factor that has facilitated the expansion of studies of these objects is the relative simplicity of their structure and the possibility of detecting radiation from both components, which enables the determination of the fundamental parameters of the stars. One of the main ways in which the list of known PCVs has been extended is via studies of white dwarfs with enhanced red and IR fluxes. Large-scale spectroscopic and photometric observations of faint blue stars carried out in the 1980s and 1990s led to substantial progress in this area [2–5]. In their latest review, Ritter and Kolb [6] present data for more than 60 objects unambiguously identified as PCVs—almost a factor of four more than were in the initial list of Ritter [1]. No fewer than 50% of the new systems contain cooling white dwarfs with moderate temperatures of $T_{eff} = 15\,000$–$35\,000$ K; i.e., they are old PCVs.

Most old PCVs display composite spectra with strong hydrogen Balmer lines, numerous lines of neutral atoms of heavy elements, and molecular bands. The band intensities indicate that the secondary components of the systems are K–M main-sequence stars. At the same time, the presence of a red dwarf in a PCV results in reflection effects due to reprocessing of the UV radiation of the hot component into optical radiation at the surfaces of the cool companion. These effects do not result in substantial brightness oscillations in old PCVs; for most systems, their amplitudes at various wavelengths do not exceed 0.2^m. However, reflection effects strongly influence the spectra of the systems, leading to the occurrence of Balmer and Paschen emission lines and lines of heavy elements with equivalent widths up to $W_\lambda = 10$ Å and more. In addition, old PCVs are distinguished by the fact that emission lines make a substantial contribution to the total V and U radiation of the system and can increase the brightness-variation amplitude by up to a factor of two at these wavelengths. Therefore, the radiation of PCVs must be analyzed taking into account the impact of reflection effects on the formation of their line spectra.

Young PCVs with brightness variations up to 1.5^m have been considered in a number of studies [7–9]. However, the temperature structure of the irradiated star was not calculated, and the reflection effects were taken into account only in a blackbody approximation. It is evident that these techniques are unable to reproduce the observed emission-line profiles and brightness-variation amplitudes of old PCVs.

Sakhibullin and Shimansky [10] suggested an alternative approach to analyzing reflection effects in the spectra of close binaries: quantitative modeling of the structure of the atmospheres of the irradiated stars based on the balance between heating and cooling of the gas. Applying this technique to the precataclysmic variable NN Ser made it possible to simultaneously reproduce the observed continuum spectra and hydrogen emission-line profiles with the same set of parameters for the system [11]. Further development of the technique [10] included calculations of blanketed spectra of binaries including the effects of X-ray and UV irradiation, taking into account the main molecular bands and more than half a million lines. In a separate study, we will demonstrate in detail the capacities of the SPECTR program package for analyzing the spectra and light curves of the close binary HW Vir.

The ability of the SPECTR package to jointly take into account the effects of reflection and blanketing made it possible to advance to studies of old PCVs. We chose MS Peg and LM Com for this purpose—two recently discovered and relatively little-studied objects.

MS Peg ≡ GD 245 was initially included in the list of single magnetic white dwarfs in the review of McCook and Sion [12]; however, Tytler and Rubenstein [13] noted the presence of Balmer emission lines. Schultz *et al.* [14] established that the intensities and radial velocities of the Hα emission varied with amplitudes exceeding $\Delta W_\lambda = 4.0$ Å and $\Delta V_r = 60$ km/s. Later, Schultz *et al.* [15] showed that the upper limit for the orbital period of MS Peg does not exceed 12 hrs, so that the object is a close binary. The only multi-faceted study of MS Peg has been made by Schmidt *et al.* [16], on the basis of original photometric and echelle-spectroscopic observations. All the observed variations of the system's radiation occur on the timescale of the orbital period, equal to $P = 0.17366$ days, and are fully consistent with the action of the reflection effect. The primary of MS Peg is on a sequence of cooling white dwarfs with an effective temperature of $T_{eff} = 22\,000$ K, while the secondary is a main-sequence M4 star. Schmidt *et al.* [16] concluded that there is no mass transfer in the system and that it is a precataclysmic variable.

LM Com ≡ PG 1224 + 309 is classified in Green's Palomar survey [3] as an object with enhanced UV radiation. Earlier, Ferguson *et al.* [17] carried out a combined photometric and spectroscopic study of several stars from [3] and demonstrated the composite nature of the spectrum of PG 1224+309. The theoretical representation of the observed spectra indicated that they include a superposition of radiation from a white dwarf with a temperature of $T_{eff} = 31\,000$ K and an M2 red dwarf. The physical binarity of the star was demonstrated in the survey of Orosz *et al.* [4], who detected variations of the radial velocities of the Hα emission with $\Delta V_r = 83$ km/s. Later, in their analysis of optical and UV photometric and spectroscopic observations of LM Com, Orosz *et al.* [18] showed that the observed brightness oscillations with amplitudes from 0.08^m in B to 0.2^m in R and I are sinusoidal and correspond rigorously to the radial-velocity variations of the primary and secondary with the period $P = 0.25869$ days. The spectra contained narrow emission lines of hydrogen and heavy elements, whose intensities varied synchronously with the brightness of LM Com. According to the derived parameters of the secondary, it is a main-sequence M star that does not fill its Roche lobe. As a result, Orosz *et al.* [18] classified LM Com as a classical PCV with pronounced reflection effects.

Thus, the evolutionary statuses of both systems have been determined with certainty; however, a substantial number of their parameters have been obtained using statistical dependences or evolutionary assumptions for the white and red dwarfs. Here, we have verified the parameters of MS Peg and LM Com based primarily on the correspondence between theoretically predicted and observed reflection effects. Our preliminary analysis of previously published observations indicated that no such correspondence was seen for the adopted parameters of the systems, and we have accordingly redetermined these parameters based on our own spectroscopic observations. In addition, we have detected some features in the spectra of the systems that cannot be explained in the

Table 1. Observations of MS Peg (JD is Julian date, φ orbital phase, and V_w, V_r the radial velocities of the primary and secondary)

JD 2451740+	φ	V_r, km/s	V_w, km/s	JD 2451740+	φ	V_r, km/s	V_w, km/s
7.3098	0.329	130.3		7.4068	0.888	−184.2	15.3
7.3148	0.358	120.8	−95.2	7.4098	0.905	−168.4	30.1
7.3208	0.393	109.9	−75.3	7.4128	0.923	−170.7	10.4
7.3238	0.410	95.6	−60.3	7.4168	0.946	−151.1	22.2
7.3278	0.433	65.7	−65.4	7.4198	0.963	−129.1	0.2
7.3318	0.456	27.4	−70.3	7.4228	0.980	−88.4	−9.8
7.3348	0.473	−5.5	−55.4	7.4258	0.997		−24.4
7.3378	0.491	−28.7	−45.7	7.4288	0.015	−34.9	−29.7
7.3398	0.502	−34.2	−33.9	7.4328	0.038		−29.7
7.3438	0.525	−58.0	−15.4	7.4388	0.072	24.2	−51.7
7.3468	0.543	−97.4	−10.5	7.4468	0.118	65.5	−78.6
7.3488	0.554	−129.7	−10.8	7.4498	0.136	92.9	−90.2
7.3518	0.571	−132.5	14.8	7.4528	0.153	128.0	−112.4
7.3548	0.589	−151.1	13.8	7.4558	0.170	144.1	−101.5
7.3578	0.606	−173.3	24.3	7.4578	0.182	163.7	−114.6
7.3598	0.617	−192.2	4.7	7.4608	0.199	158.0	−109.8
7.3628	0.635	−211.6	34.5	7.4648	0.222	166.3	−122
7.3648	0.646	−222.8	34.5	7.4688	0.245	180.6	−114.3
7.3678	0.663	−244.0	53.9	7.4718	0.262	174.9	−117.9
7.3718	0.686	−251.2	39.4	7.4738	0.274	182.8	−119.7
7.3738	0.698	−268.4	35.3	7.4768	0.291	171.7	−129.0
7.3768	0.715	−271.1	59.5	7.4798	0.308	174.8	−99.4
7.3988	0.842	−217.9	51.0	7.4828	0.326	155.7	−107.5
7.4038	0.871	−214.3	50.0				

framework of existing models of binary spectra with reflection effects. We present brief descriptions of our observations and modeling technique in Sections 2 and 3. In Section 4, the radial-velocity curves are analyzed and the ephemeris of each system is refined. Complete sets of parameters for MS Peg and LM Com are derived in Section 5. In Section 6, we analyze the accuracy of the modeling technique and also consider the observed characteristics of the λ3905 Å emission and possible physical mechanisms for its formation.

2. OBSERVATIONS

Spectroscopic observations of MS Peg and LM Com were carried out with the 6-m telescope of the Special Astrophysical Observatory equipped with a long-slit spectrograph [19] and a CCD detector (Photometrics, 1024 × 1024 pixels with size 24 × 24 micron) mounted at the prime focus. MS Peg was observed on July 21, 2000 using a diffraction grating with 1302 lines/mm, providing a dispersion of 1.2 Å/pixel. The star was studied in the two spectral intervals $\Delta\lambda = 3880{-}5120$ Å and $\Delta\lambda = 4050{-}5290$ Å. The seeing disk exceeded $2''$, which enabled us to obtain spectra with a resolution of about 2.6 Å. LM Com was observed on January 16, 2001 under favorable conditions; the seeing disk was smaller than $1''$. Due to the low brightness of the object ($m_V = 16.16^m$ [18]), a grating with 651 lines/mm was used, which provided a dispersion of 2.35 Å/pixel. Spectra in the interval $\Delta\lambda = 3700{-}6100$ Å with a two-pixel resolution of 4.6 Å were obtained. In total, 47 individual spectrograms with exposures of 180 s for MS Peg and 57 spectrograms with exposures of 300 s for LM Com were obtained, fully covering the orbital periods of the systems. The average signal-to-noise ratios were $S/N = 39$ in the MS Peg and $S/N = 46$ in the LM Com spectrograms. The wavelength and flux

Table 2. Observations of LM Com (JD is Julian date, φ is orbital phase, and V_w, V_r are the radial velocities of the primary and secondary)

JD 2451920+	φ	V_r, km/s	V_w, km/s	JD 2451920+	φ	V_r, km/s	V_w, km/s
6.414	0.636	73	29	6.528	0.077		−40
6.419	0.655	94	51	6.531	0.088		−39
6.422	0.667	52	63	6.535	0.104		−50
6.426	0.682	40	76	6.539	0.119		−75
6.43	0.698	16	47	6.543	0.135		−89
6.434	0.713	−5	45	6.546	0.146		−80
6.437	0.725	−47	72	6.551	0.166		−109
6.442	0.744	−14	85	6.554	0.177		−70
6.446	0.760	−71	79	6.558	0.193		−110
6.449	0.771	−78	75	6.562	0.208		−64
6.453	0.787	−67	69	6.566	0.224		−81
6.457	0.802	−62	84	6.57	0.239		−119
6.461	0.818	−98	65	6.573	0.251		−102
6.464	0.829	−107	59	6.578	0.270	238	−78
6.469	0.849	−85	50	6.581	0.282	259	−127
6.472	0.860	−114	38	6.585	0.297	277	−84
6.476	0.876		29	6.589	0.313	279	−71
6.481	0.895	−122	29	6.593	0.328	245	−55
6.485	0.910	−92	45	6.598	0.347	238	−70
6.489	0.926		24	6.602	0.363	265	−51
6.492	0.938		21	6.605	0.383	253	
6.496	0.953		9	6.637	0.506	249	−18
6.5	0.968		−10	6.641	0.522	242	6
6.504	0.984		−9	6.645	0.537	199	1
6.508	0.999		19	6.648	0.549	181	11
6.512	0.015		−21	6.653	0.568	175	17
6.516	0.030		−27	6.656	0.580	154	33
6.52	0.046		−23	6.660	0.595	103	52
6.523	0.057		−25				

calibration were carried out using spectra of an Ar-Ne-He lamp and of the spectrophotometric standard star BD+28 2106 [20], obtained simultaneously with the observations of the studied systems. The observing logs presented in Tables 1 and 2 contain the Julian dates of the observations, the orbital phases φ according to our corrected ephemeris (see below), and the derived heliocentric radial velocities of the primary $V_w(obs)$ and secondary $V_r(obs)$ components.

The spectrograms were processed using standard procedures in the MIDAS package [21].

3. MODELING TECHNIQUE

In our studies of MS Peg and LM Com, we have used the results of theoretical modeling of the system radiation taking into account reflection effects a number of times. Here, we briefly describe the modeling procedure and the accuracy of the calculated data; these will later be refined and presented in detail in a separate study.

Initially, the surface of each star is divided into concentric rings with their centers coincident with the semimajor axis of the system. For each ring, the local parameters of the external radiation (its intensity K_x in units of the integrated radiation of

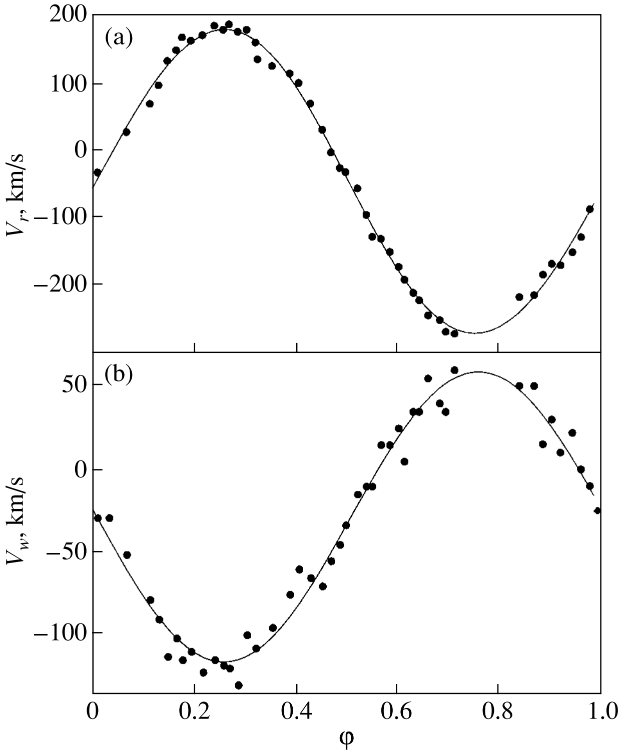

Fig. 1. Radial-velocity curves for the (a) red and (b) white dwarfs in MS Peg. The upper and lower plots present the approximations for the elliptical and circular orbit.

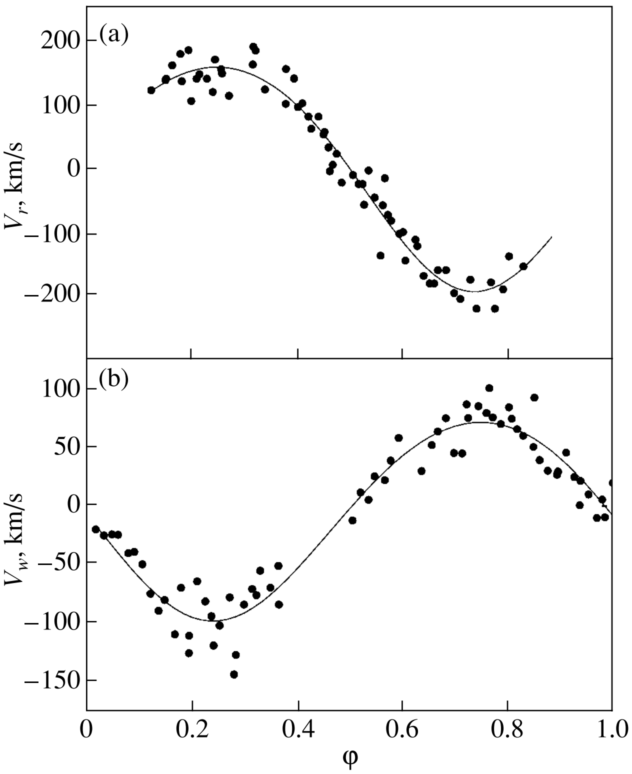

Fig. 2. Radial-velocity curves for the (a) red and (b) white dwarfs in LM Com. The upper and lower plots present the approximations for the elliptical and circular orbit.

the atmosphere and the cosine of the angle of incidence $\mu = \cos\theta$) are determined taking into account the mutual influence of the components' radiation. When modeling the primaries, external radiation was not included; when modeling the secondaries, the frequency distribution for the incoming radiative flux corresponded to the spectra of white dwarfs with the appropriate parameters. Next, the temperature structure of the local irradiated atmosphere was calculated following the procedure [22], together with the specific intensity of the radiation emitted at various angles to the surface of the star. The specific intensities were determined in the wavelength interval $\Delta\lambda = 3000–10\,000$ Å in steps of $\Delta\lambda = 0.035$ Å taking into account all sources of opacity tabulated in the SPECTR program package [10]—about 530 000 lines from [23] and the main molecular bands obtained by Ya. Pavlenko (Central Astronomical Observatory, National Academy of Sciences of the Ukraine) in the framework of the theory of Nersysian *et al.* [24]. The hydrogen-line profiles were obtained using the broadening theory of Vidal, Cooper, and Smith [25]. Some additional broadening factors were considered for other lines: Doppler broadening due to thermal motions and microturbulence (with $\xi_{turb} = 1.5$ km/s), natural damping, Stark broadening in the approximation of [23], and van der Waals broadening, with the constants C_6 determined from the classical Unsold formula [26] with the scaling factor $\Delta \log C_6 = 0.7$.

To determine the total spectrum of the stellar radiation, all the rings were divided into sectors in steps of 1°. The visibility conditions (inclination of the surface to the line of sight), area, possibility of being eclipsed by the companion, and radial velocity due to the star's rotation were determined for each sector. The spectra from all the sectors were summed taking into account the Doppler shifts specified by the radial velocities. The total spectra of the systems were obtained for 72 orbital phases by summing the spectra of the system components for the specified component radii, radial velocities of the orbital motion, and detector response function, which was represented by a Gaussian whose half-width corresponded to the resolution. When analyzing the light curves of the objects, the total radiated fluxes were convolved with the transparency curves for the Johnson system in accordance with the data of [27].

The following initial data are required to carry out the calculations using the suggested technique: the

Table 3. Parameters of MS Peg

Parameter	Component	
	primary	secondary
$P_{\rm orb}$, days	0.1736660 ± 0.0000002	
φ_0 (JD)	2451747.428 ± 0.0006	
K, km/s	-87.0 ± 2.1	222.8 ± 2.5
γ, km/s	-28.5 ± 1.4	-48.6 ± 1.8
e	0.012 ± 0.006	
ω, deg	340 ± 30	
q	0.39 ± 0.02	
T_{eff}, K	$22170 \pm 130^*$	3560 ± 150
$M/M_\odot$	0.49 ± 0.04	0.19 ± 0.02
$R/R_\odot$	0.015 ± 0.001	0.18 ± 0.01
$a/R_\odot$	1.15 ± 0.03	
i, deg	67.6 ± 2.1	
π, arcseconds	0.017	

* Value taken from [16].

Table 4. Parameters of LM Com

Parameter	Component	
	primary	secondary
$P_{\rm orb}$ (days)	0.2586873 ± 0.0000012	
φ_0 (JD)	2451926.506 ± 0.002	
K, km/s	-84.6 ± 3.1	175.9 ± 4.8
γ, km/s	-10.3 ± 4.8	-11.2 ± 5.4
e	0.04 ± 0.03	
ω, deg	250 ± 20	
q	0.48 ± 0.02	
T_{eff}, K	$29300 \pm 500^*$	3650 ± 150
$M/M_\odot$	0.35 ± 0.03	0.17 ± 0.02
$R/R_\odot$	0.020 ± 0.003	0.22 ± 0.02
$a/R_\odot$	1.37 ± 0.04	
i, deg	75 ± 4	
π, arcseconds	0.0035	

* Value taken from [18].

atmospheric parameters of the stars (effective temperature T_{eff}, surface gravity $\log g$, metallicity $[A]$), their radii in units of the semimajor axes, the inclination of the system to the line of sight, and the amplitudes of both the orbital and rotational velocities of the components.

The parameters of the hydrogen atmospheres of the white dwarfs in MS Peg ($T_{eff} = 22\,170 \pm 130$ K, $\log g = 8.05 \pm 0.02$) [16] and LM Com ($T_{eff} = 29\,300 \pm 400$ K, $\log g = 7.38 \pm 0.1$) [18] were derived by Bergeron [28] from the observed Balmer-line profiles. Our calculations of the spectra of the systems at orbital phases close to the minimum brightness indicated that these T_{eff} and $\log g$ values can reproduce the observed hydrogen-line profiles and continuum slopes with sufficient accuracy (Fig. 5). The observed MS Peg spectra at minimum brightness did not reveal any absorption lines of helium and heavy elements associated with the radiation of the primary. The spectra of LM Com contain numerous unidentified absorption features; however, helium lines are likewise absent. Accordingly, we used the BINARY3 code [29] to calculate the model atmospheres for the hydrogen white dwarfs with the parameters found by Bergeron *et al.* [28] and used these in our further analysis. Models of the non-irradiated atmospheres of the secondaries were interpolated in T_{eff} and $\log g$ using the model grid of Kurucz [23]. The corresponding atmospheric parameters of the objects were also determined, as were their radii and the amplitudes of their radial velocities (see below). In the calculations, we used a solar-abundance scale of heavy elements in accordance with the data from [30].

4. RADIAL VELOCITIES

We derived the radial velocities by comparing the theoretical and observed spectra of both systems. The theoretical spectra taking into account reflection effects were calculated following the above procedure, essentially using the parameters of MS Peg and LM Com published in [16, 18]. The exception was that the radii of the secondaries R_r were varied to match the theoretical and observed light curves [16, 18]. As a result, we obtained the preliminary estimates for the radii $R_r = 0.19\ R_\odot$ for MS Peg and $R_r = 0.23\ R_\odot$ for LM Com. The corresponding rotational velocities of the secondaries were calculated assuming that the rotation was synchronous with the orbital motion: $V \sin i = 52$ km/s and $V \sin i =$

40 km/s. Previously, a number of studies of binaries including reflection effects [9, 31] have considered the question of how temperature inhomogeneities on the surfaces of rapidly rotating secondaries can result in differences in the radial velocities determined from groups of emission and absorption lines. For example, Wood *et al.* [32] present an empirical relationship for the calculation of the velocity of the center of mass of a star from the velocity derived from emission lines. However, our technique automatically takes into account the Doppler shifts of lines when the spectra of individual surface elements are calculated. Therefore, our radial-velocity estimates for the secondaries refer to their centers of mass. According to our calculations, taking into account the rotational velocities of the secondaries increases the amplitude of the radial velocities derived from emission lines by $\Delta K_r = 22$ km/s for MS Peg and by $\Delta K_r = 17$ km/s for LM Com.

Tables 1 and 2 present heliocentric radial velocities for both components of MS Peg and LM Com. When determining the radial velocities of the red dwarfs, we took into account the Doppler shifts of the H_β, TiI $\lambda5036, 5038$ Å, CaII $\lambda3933, 3968$ Å, FeI $\lambda5012$ Å, FeII $\lambda4549, 4923, 5018$ Å, and MgI $\lambda5183$ Å emission lines and of the intense emission blend formed by the MgI $\lambda5167$, 5172 Å, FeI $\lambda5167$ Å and FeII $\lambda5169$ Å lines. For LM Com, we also used the FeI $\lambda5269$ Å emission line and the combined NaI $\lambda5189, 5195$ Å doublet. To determine the radial velocities of the white dwarfs, we analyzed the H_β, H_γ, and H_δ absorption lines in the spectra of both systems. The resolution of the MS Peg spectra was $\dfrac{\lambda}{\Delta\lambda} \approx 1700$, which provided accuracies for the radial velocities of the primary and secondary of $\sigma = 10.7$ km/s and $\sigma = 9.3$ km/s, respectively. In the case of LM Com, the accuracy of the radial velocities was limited by the lower spectral resolution ($\frac{\lambda}{\Delta\lambda} \approx 1000$) to the estimated values $\sigma = 21$ km/s for the white dwarf and $\sigma = 23$ km/s for the red dwarf.

A comparison between the observed and theoretical velocities of the red dwarf in MS Peg calculated using the refined ephemeris of [16] indicated a phase shift of about 0.35 of an orbital period. We accordingly carried out a joint analysis of the radial-velocity curve using the data of [15, 16] and of the present study, which yielded the refined ephemeris

$$\mathrm{JD} = 2451747.428(\pm 0.0006)$$
$$+\,0.1736660(\pm 0.0000002)E,$$

where $E = 0.0$ corresponds to minimum reflection effects. The duration of the interval covering the analyzed observations is 2900 days (16 700 periods), making it possible to achieve high accuracy in the orbital period (2×10^{-7} days).

The number of measured radial velocities of the red dwarf of LM Com is insufficient to enable a reliable approximation using a circular orbit. The observed velocities of the white dwarf indicate that the error in the ephemeris [18] for the epoch of our observations was about 0.046 of an orbital period. Taking into account the maximum acceptable period error [18] of 0.000004 days, we corrected the LM Com ephemeris:

$$\mathrm{JD} = 2451926.506(\pm 0.002)$$
$$+\,0.2586873E(\pm 0.0000012).$$

In our subsequent analysis of the radial-velocity curves for both components, we used our data together with the data of [14, 18].

We studied the measured radial velocities of the red dwarf in MS Peg and of the white dwarf in LM Com using models with circular and elliptical orbits; in the remaining cases, we restricted our consideration to the case of a circular orbit. Figures 1 and 2 present the resulting light curves, and the corresponding orbital parameters are given in Tables 3 and 4. We can draw the following conclusions.

(1) **MS Peg**

a) The orbital eccentricity does not exceed $e = 0.02$.

b) The γ velocities of the red dwarf obtained from the data of [15] and of the present study differ by $\Delta\gamma = 25 \pm 6$ km/s; this discrepancy cannot be due to incorrect account of the rotational velocity of the secondary, and its origin remains unclear.

c) Our radial-velocity amplitudes and those presented by Schmidt *et al.* [16] ($K_w = 101 \pm 6$ km/s, $K_r = 216 \pm 4$ km/s) are consistent within 1σ for the red dwarf and 2σ for the white dwarf; when the radial velocities measured from the $\mathrm{H}\gamma$ lines are excluded from the analysis, the K_w values determined in both studies also coincide within 1σ.

d) The ratio of the amplitudes of the radial velocities of the components is $q = K_w/K_r = M_r/M_w = 0.39 \pm 0.02$, and the difference of the γ velocities is $\Delta\gamma = \gamma_w - \gamma_r = 20.1 \pm 2.2$ km/s.

(2) **LM Com**

a) The orbit may display a slight eccentricity of about $e = 0.04$.

b) The derived γ velocity of the white dwarf coincides with $\gamma_w = -4 \pm 12$ km/s from [18] within the errors. At the same time, the γ velocity of the red dwarf is smaller than that presented in [18] by $\Delta\gamma_r = 18$ km/s, i.e., by approximately 2σ.

c) We have substantially corrected the amplitude of the radial velocities of the white dwarf given in [18] ($K_w = 112 \pm 14$ km/s) using the large number of our measured $V_w(obs)$ values. The similar variation in the amplitude for the secondary, $\Delta K_r = 16$ km/s, can be explained by the fact that Orosz *et al.* [18] did not take into account corrections of the radial velocities for the rotation of the red dwarf, which they estimated to be $\Delta K_r = 21$ km/s.

d) The ratio of the amplitudes of the radial velocities of the components is $q = K_w/K_r = M_r/M_w = 0.48 \pm 0.02$, and the difference of the γ velocities is $\Delta\gamma = \gamma_w - \gamma_r = 0.9 \pm 7.3$ km/s.

5. PARAMETERS OF MS Peg AND LM Com

The difference between the γ velocities of the primary and secondary corresponds to the difference of the gravitational potentials at their surfaces:

$$\Omega_w - \Omega_r = c\Delta\gamma.$$

As will be shown below, the secondary components of the systems are main-sequence M stars whose gravitational potentials vary within a small interval $\Omega_r = 1.0{-}1.2\ \Omega_\odot$, according to their evolutionary tracks [33]. As a result, applying the above formula, we will obtain $\Omega_w = 32.7 \pm 3.7\Omega_\odot$ for MS Peg and $\Omega_w = 2.2 \pm 11.6\ \Omega_\odot$ for LM Com. For all possible parameters of the white dwarf in LM Com, the gravitational potential at its surface should exceed $\Omega_w = 15\ \Omega_\odot$. Therefore, the calculated Ω_w value indicates some errors in the radial velocities derived from the Balmer lines in the spectra of the white dwarfs with resolution $\dfrac{\lambda}{\Delta\lambda} \approx 1000$.

The mass M and radius R of a star can be determined directly from the potential and gravitational acceleration at the stellar surface, if known. The value of $\log g$ at the surfaces of the white dwarfs were also found using the method of [28] to be $\log g = 7.77 \pm 0.02$ [16] for MS Peg and $\log g = 7.38 \pm 0.1$ [18] for LM Com. The combination of Ω_w and $\log g_w$ for MS Peg yields a mass for the white dwarf of $M_w = 0.49\ M_\odot$ and a radius of $R_w = 0.015\ R_\odot$. Taking into account the known component-mass ratio $q = 0.39$, we can calculate the mass of the red dwarf, $M_r = 0.19\ M_\odot$, the semimajor axis of the system, $A = 1.15\ R_\odot$, and the inclination of the orbit to the plane of the sky, $i = 68°$. The resulting parameters of the primary correspond to a star on the theoretical tracks of [34] with a degenerate carbon core and a thin ($M = 10^{-4}\ M_\odot$) hydrogen envelope.

This procedure cannot be used to directly calculate the parameters of LM Com. Therefore, we determined the mass ($M_w = 0.35\ M_\odot$) and radius ($R_w = 0.020\ R_\odot$) of the white dwarf from its atmosphere parameters (see above) using the evolutionary models of [34] for stars with carbon cores. The corresponding mass of the secondary is $M_r = 0.17\ M_\odot$, the semimajor axis of the system is $A = 1.37\ R_\odot$, and the inclination of the orbit to the plane of the sky is $i = 73°$.

The radii of the red dwarfs in both systems were derived by fitting the observed MS Peg [16] and LM Com [18] light curves using the procedure for modeling reflection effects described above. Under the conditions in old precataclysmic variables, the total amplitudes of the U, B, V, and R brightnesses are specified by the ratio of the radius of the secondary and the semimajor axis R_r/A and also by the effective temperature of the primary. On the other hand, the ratios of the brightness amplitudes in different bands depend on the effective temperatures of the components, the radius of the white dwarf R_w, and the metallicity of the red dwarf [M/H], while the shape of the light curve depends on the ratio R_r/A and the orbit's inclination to the plane of the sky i.

We adopted initial values for the effective temperatures of the red dwarfs in accordance with [16, 18]: $T_{eff} = 3560$ K for MS Peg and $T_{eff} = 3650$ K for LM Com. A comparison of the theoretical and observed absorption features in the spectra at phases close to $\varphi = 0.0$ indicates that the errors in these adopted temperatures do not exceed $\Delta T_{eff} = 150$ K for MS Peg and $\Delta T_{eff} = 250$ K for LM Com. The intensities of molecular bands and metallic lines in the wavelength interval $\Delta\lambda 4700{-}5400$ Å suggest that the red dwarfs have solar metallicity, with possible deviations Δ[M/H] $\pm$ 0.2 for MS Peg and Δ[M/H] $\pm$ 0.4 for LM Com.

Thus, we found preliminary values for most of the model parameters used in independent ways. Therefore, the fitting of the observed light curves makes it possible not only to determine the radii of the red dwarfs, but also to verify the entire set of parameters.

Figures 3a and 3b present the resulting observed and theoretical U, B, and V light curves for MS Peg and the B, V, and R light curves for LM Com. The corresponding radii of the secondaries are $R_r = 0.18\ R_\odot$ and $R_r = 0.22\ R_\odot$. We were able to reproduce well the observed amplitudes and shapes of the light curves of MS Peg. The deviations from the theoretical U and B curves at the end of the observations are clearly due to some peculiarities of those observations and were not taken into consideration. The theoretical amplitudes of the brightness variations of LM Com are also overall in good consistency with the observed. However, as we can see in Fig. 3b, the observed interval when reflection effects influence the object's brightness is 6–8% longer than predicted. Test calculations varying the parameters of LM Com indicated that the observed R light curve cannot be accurately fit with the reflection-effect model. The observed distortions of the light curve may be due

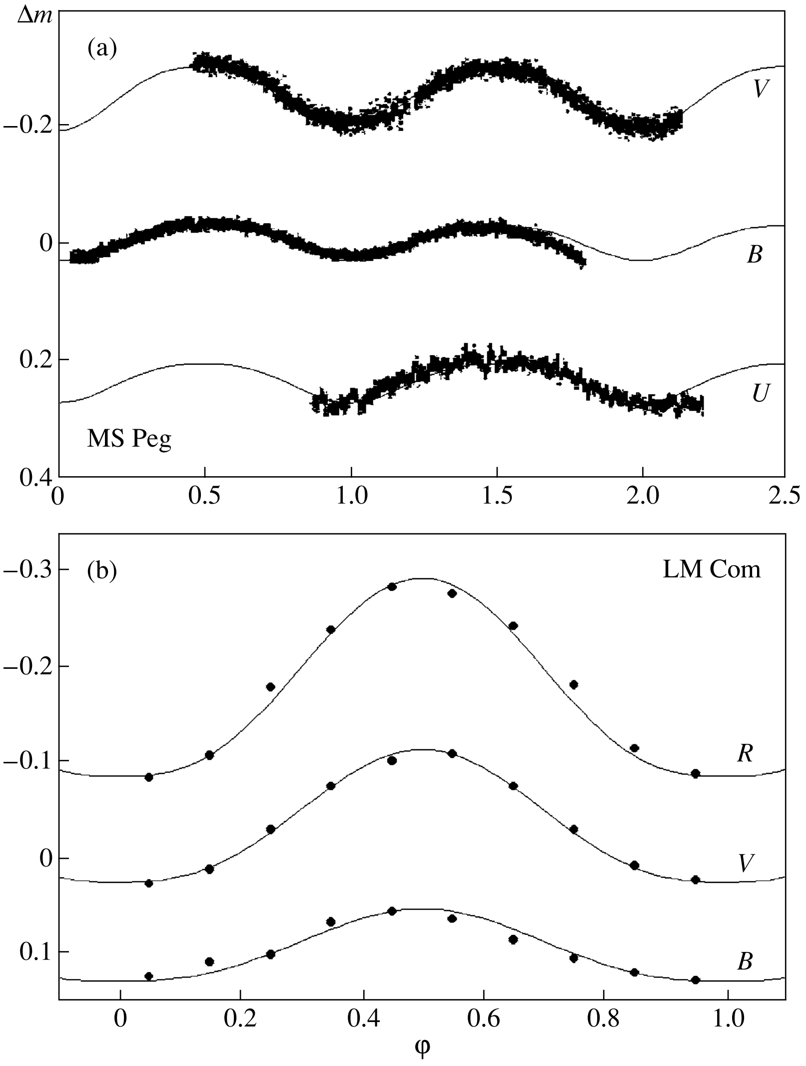

Fig. 3. Observed (points) [22, 24] and theoretical (curves) (a) U, B, and V light curves for MS Peg and (b) B, V, and R light curves for LM Com.

to weak horizontal energy transport in the course of surface mass transfer from the central zones of a hot spot to its periphery. The role of and mechanisms for such horizontal transport have been considered previously in a number of studies; their application to LM Com requires a special analysis.

Tables 3 and 4 present the resulting system parameters. The parallaxes of the objects were estimated using the apparent V magnitudes $m_v(\text{MS Peg}) = 13\overset{m}{.}68$ [35] and $m_v(\text{LM Com}) = 16\overset{m}{.}16$ [18], the effective temperatures and radii of the components, and the theoretical calibrations of [23]. The effective temperature and radius of the MS Peg red dwarf coincide with the evolutionary tracks of main-sequence stars with mass $M_r = 0.19\,M_\odot$ within the errors [33]. On the other hand, evolutionary models of stars with a mass of $M_r = 0.17\,M_\odot$ yield an effective temperature and radius lower than those determined for the LM Com red dwarf by $\Delta T_{eff} = 250$ K and $\Delta R_r = 0.03\,R_\odot$. It has repeatedly been noted in earlier studies of young PCVs [8, 9, 36] that their secondaries display effective temperatures and radii exceeding the normal values for the corresponding main-sequence stars by up to a factor of two. These perturbations occur in late-type stars during the common-envelope stage [1, 37] and remain in young PCVs, whose average age does not exceed 3×10^5 yrs. At the same time, studies of the old precataclysmic variables EG UMa [38] and HR Cam [31], with ages of more than 10^8 yrs, indicated that the parameters of the secondaries were in good consistency with evolutionary models for the stars. Therefore, the differences between the calculated and model parameters of the LM Com red dwarf may be determined by the average time for the relaxation of the secondaries toward their quiescent state after

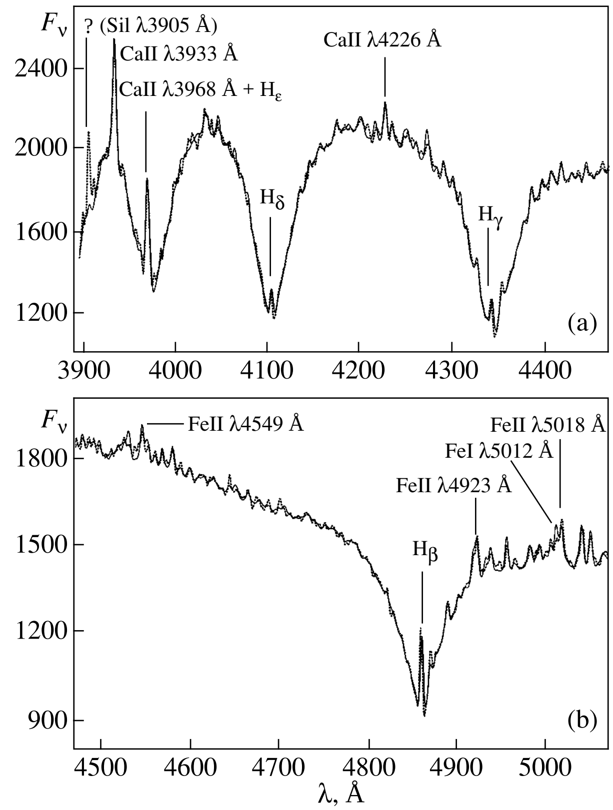

Fig. 4. Theoretical (solid) and observed (dotted) averaged spectra of MS Peg at orbital phases $\varphi = 0.4$–0.6. The arrows indicate the spectral lines used to determine the radial velocities.

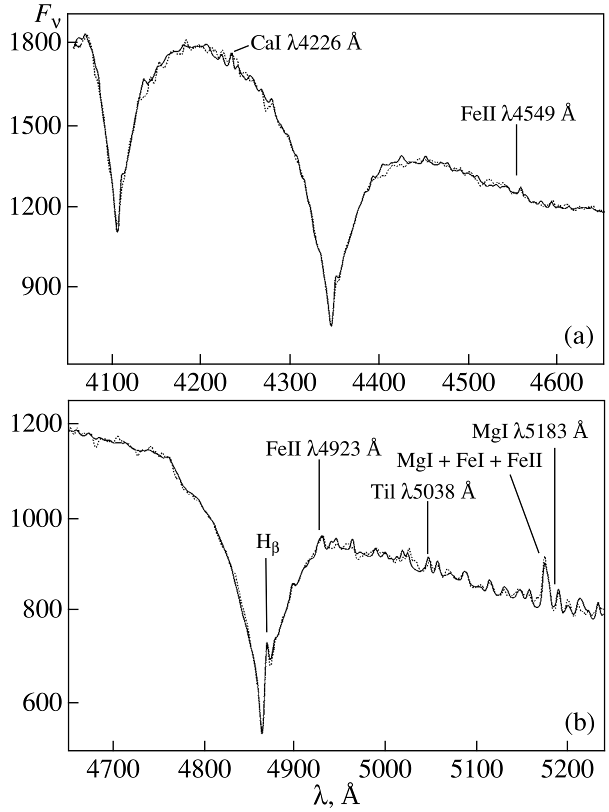

Fig. 5. Theoretical and observed averaged spectra of MS Peg at orbital phases $\varphi = 0.2$–0.3. The notation is the same as in Fig. 4.

they undergo the common-envelope stage. Using the parameters of the LM Com white dwarf, we can estimate this time to be 5×10^6 years.

6. REFLECTION EFFECTS IN THE SPECTRA OF MS Peg AND LM Com

To verify the resulting parameters of the systems and the procedure used to take reflection effects into account, we compared the theoretical and observed spectra at various orbital phases. Since the signal-to-noise ratio of the individual spectrograms is fairly low ($S/N \approx 45$), we averaged spectra at similar phases. In the averaging, all the spectrograms were transformed into the reference system of the secondary, underwent three-point smoothing in wavelength, and were summed in time intervals with a duration of 0.1 of the orbital period. The signal-to-noise ratios of the resulting spectra were about $S/N = 100$ for MS Peg and $S/N = 120$ for LM Com. In addition, we obtained spectra at the maximum and minimum brightnesses with signal-to-noise ratios $S/N = 150$ by summing the spectrograms within phases $\Delta\varphi = 0.9$–0.1 and $\Delta\varphi = 0.4$–0.6. All the theoretical spectra were averaged in the same way for the comparisons. Figures 4 and 5 present the resulting spectra of MS Peg at the maximum brightness and at elongation, while Fig. 6 presents the spectra of LM Com at the maximum brightness.

We can see from Figs. 4–6 that the additional radiation in emission lines of heavy elements contributes substantially to the total U, B, and V brightnesses of the objects. Test calculations for the MS Peg light curves indicate that taking into account blanketing in lines and molecular bands increases the brightness in the V band by 35%, in the B band by 25%, and in the U band by more than a factor of two. Therefore, quantitative analyses of the reflection effects in old PCVs require that the emission lines and, accordingly, the structure of the irradiated atmosphere of the secondary be properly modeled. A comparison of the observed and theoretical spectra of MS Peg and LM Com indicates that this problem can be solved using our technique. For example, the theoretical intensities and Doppler half-widths of emission lines at wavelengths $\Delta\lambda = 3920$–5500 Å coincide with the observed values at various orbital phases. As a result, we can draw the following conclusions about the physics of reflection effects in old PCVs.

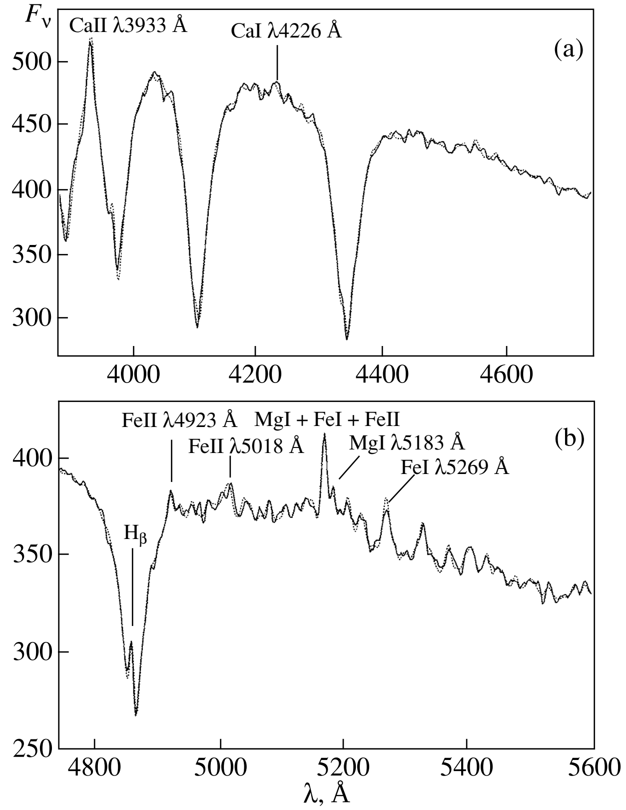

Fig. 6. Theoretical and observed averaged spectra of LM Com at orbital phases $\varphi = 0.5{-}0.6$. The notation is the same as in Fig. 4.

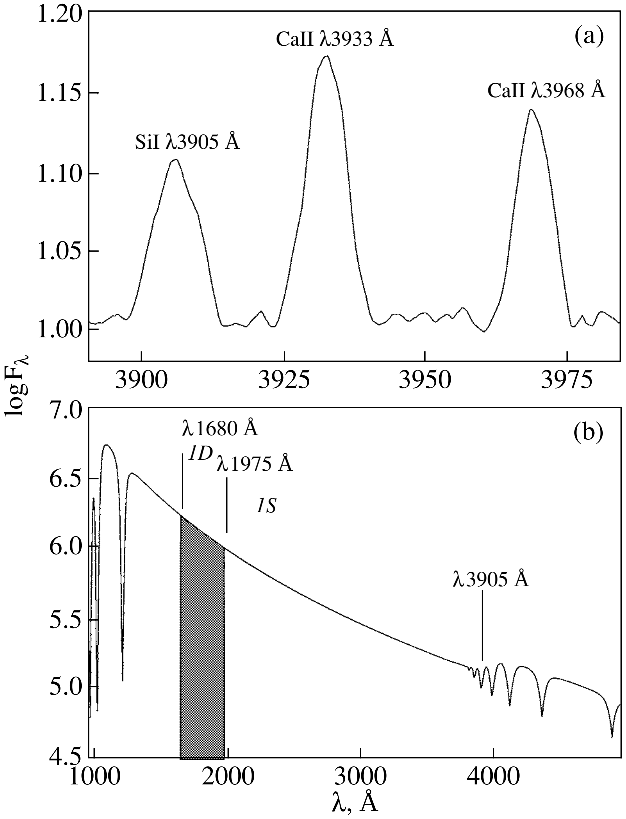

Fig. 7. Formation of SiI λ3905 Å lines in the spectra of LM Com: (a) normalized observed spectrum at phases $\varphi = 0.4{-}0.6$ and (b) theoretical spectrum of the white dwarf. The interval $\Delta\lambda = 1680{-}1975$ Å for the ionization of SiI atoms from the $3s^23p^2$ $1S$ level and the site of formation of the λ3905 Å line are marked in the lower plot.

(1) The structure of the irradiated atmosphere is specified by the absorption and re-emission of the incoming flux, with the preservation of thermal-balance conditions; no signs of the influence of stellar wind and magnetic fields on the atmosphere have been detected.

(2) The atmosphere of the secondary has no global high-velocity flows of matter, which would result in deformations of the emission-line profiles. As is noted above, such flows can transport energy horizontally within a hot-spot zone. Given the resolution of the spectra of MS Peg (2.6 Å), we estimate the upper limit for the velocity of such flows to be $V_{trans} = 35$ km/s.

(3) More than 90% of the emission lines of metals in the first and second ionization stages form under conditions close to thermalization. A similar conclusion was previously drawn for the CaII ion based on non-LTE studies of its equilibrium states in stellar atmospheres with external irradiation [39]. Taking into account deviations from LTE in the populations of CaII levels in the irradiated atmospheres of secondaries in old PCVs decreases the intensity of the $\lambda\lambda$3933, 3968 Å emission lines by no more than 10%. Therefore, the line spectra of these systems may be calculated in an LTE approximation.

However, our LTE study of the spectra of MS Peg cannot explain the strong emission feature at λ3905 Å (Fig. 4). Its Doppler shifts are in full agreement with those of other emission lines; the precise wavelength of the feature is λ3905.5 Å. The equivalent width W_λ of the emission line varies synchronously with that of the CaII λ3933, 3968 Å lines and reaches $W_\lambda =$ 900 mÅ at maximum brightness. Thus, the λ3905 Å emission feature forms under the action of external radiation in a hot-spot zone on the surface of the MS Peg secondary. Bearing in mind the similar values of the parameters and reflection effects in the two studied systems, we searched for λ3905 Å emission in the spectra of LM Com. For this purpose, we normalized the averaged observed spectrum in the phase interval $\Delta\varphi = 0.4{-}0.6$ to the theoretical spectrum, calculated without taking into account blanketing in the lines. Figure 7a presents the resulting spectrum within the interval $\Delta\lambda 3900{-}4000$ Å. The emission feature $\lambda 3905$ Å is evident, and its intensity is comparable to those of the CaII $\lambda 3933, 3968$ Å lines. We detected a similar emission line in published observed spectra of the star BPM 6502 [40], whose parameters overall correspond to those of MS Peg. Thus, $\lambda 3905$ Å line emission is characteristic of the spectra of a number of old PCVs with moderately cool primaries and requires special consideration.

We suggest that this emission feature is most likely the $\lambda 3905.523$ Å line, formed in the $3s^2 3p^2\, 1S{-}3s^2 3p4s\, 1P^0$ transitions of neutral silicon. According to various studies, the oscillator strength of this line ranges from $f = 0.081$ [23] to $f = 0.101$ [41]. The lower transition level is metastable, with an excitation energy of $E_{ex} = 1.909$ eV [23]. In the flux atlas of the quiescent Sun [42], the SiI $\lambda 3905$ Å line displays an absorption profile with an equivalent width of about $W_\lambda = 1100$ mÅ. However, in the spectra of sunspots and active flare regions, the line contains an emission core of variable intensity, which cannot be explained in an LTE approach. Non-LTE calculations [43] indicated that the $\lambda 3905$ Å emission in the spectrum of the solar photosphere is associated with UV irradiation from the chromosphere at wavelengths $\Delta\lambda = 1300{-}1800$ Å. The external irradiation results in the "superionization" of SiI atoms from weakly excited levels in the SiII state, with the subsequent recombination of the atoms into highly excited SiI levels and the enhanced generation of photons in lines of cascade transitions.

The efficiency of this mechanism for the formation of the SiI $\lambda 3905$ Å line may increase in the atmospheres of old-PCV secondaries. To analyze this mechanism from an energetic point of view, we will consider the variable LM Com; the theoretical spectrum of the white dwarf in this system is presented in Fig. 7b. In the atmosphere of an M star, the radiative ionization of SiI atoms from the $3s^2 3p^2\ 1S$ level occurs primarily in the wavelength interval indicated in Fig. 7b and is limited by the thresholds of ionization from the $3s^2 3p^2\ 1S$ ($\lambda = 1975$ Å) and $3s^2 3p^2\ 1D$ ($\lambda = 1680$ Å) levels. In this interval, the bound–free transition from the $3s^2 3p^2\ 1S$ level contributes 15–30% of the total absorption coefficient of the medium. The integrated radiation of the white dwarf at wavelengths $\Delta\lambda = 1300{-}1800$ Å exceeds the observed intensity of the $\lambda 3905$ Å line by a factor of 4×10^3. Taking into account the dilution of this radiation at the surface of the secondary, less than 3% of the flux resulting in the ionization of atoms from the $3s^2 3p^2\ 1S$ level is re-emitted in the $3s^2 3p4s\ 1P^0{-}3s^2 3p^2\ 1S$ cascade-transition lines. This demonstrates the energetic possibility that the $\lambda 3905$ Å emission line forms under the action of ionizing processes at UV wavelengths. The thermalization of reflection spectra is apparently violated during the formation of Si lines, which requires a separate non-LTE study. Note that SiI $\lambda 4102$ Å line emission, which is formed by a similar mechanism [43], is not observed in the spectra of PCVs due to the small oscillator strength, $f = 0.00074$ [23].

Thus, the $\lambda 3905$ Å emission in the spectra of PCVs is probably due to the UV irradiation of the stars; i.e., it has a purely radiative origin. In contrast, this line is not seen in the spectra of single UV Ceti-type flare stars, which possess thick chromospheres that emit relatively little UV irradiation. This suggests a new method of searching for close wd+dM, dA+dK and symbiotic binaries with reflection effects. Standard techniques for detecting such systems involve long-term photometric or spectroscopic observations of stars with composite spectra with Balmer and H and K CaII emission lines. At the same time, the identification of $\lambda 3905$ Å emission in individual spectra of an object will provide direct evidence that it is a close binary with significant reflection effects. The advantages of this approach are most obvious for systems with small orbital inclinations, where the brightness and radial-velocity variations of the components are small. However, the applicability of the method is restricted to close binaries containing white dwarfs with $\Delta T_{eff} = 17\,000{-}35\,000$ K. The UV radiation of objects with $T_{eff} < 17\,000$ K is insufficient to give rise to the observed reflection effects, while the $\lambda 3905$ Å emission cannot originate due to a high degree of ionization of SiI atoms in the atmosphere of a hot spot in systems containing hot white dwarfs and blue subdwarfs.

7. CONCLUSION

We have analyzed reflection effects in old precataclysmic systems and their use in determining the parameters of these objects. Similar studies of eclipsing binaries carried out previously by other authors were very effective in blackbody approximations. Our results indicate that quantitative light-curve analyses remain effective, even in the absence of eclipses. However, our new modeling of the emission lines originating during the irradiation of cool components by their hot companions has yielded a number of qualitatively new results.

(1) The parameters of the primaries of MS Peg and LM Com are consistent with those calculated in models of cooling white dwarfs with carbon cores and thin hydrogen envelopes [34].

(2) The effective temperature ($T_{eff} = 3560$ K) and radius ($R_r = 0.18\,R_\odot$) of the MS Peg secondary are consistent with evolutionary models of main-sequence stars with mass $M_r = 0.19\,M_\odot$ and solar chemical composition. On the other hand, the parameters of the LM Com red dwarf ($T_{eff} = 3650$ K, $R_r = 0.22\,R_\odot$) exceed the theoretical values for a star with mass $M_r = 0.17\,M_\odot$. This discrepancy may indicate that there is a substantial period of relaxation of the red dwarfs to their quiescent state after the ejection of a common envelope by the close binary. For LM Com, the duration of this period is no less than 5×10^6 yrs.

(3) Adequate modeling of the observed spectral lines is possible for both systems using the theory of the formation of the radiation of irradiated atmospheres and the derived sets of system parameters. The profiles of most of the lines can be calculated based on model atmospheres in an LTE approximation. Taking into account blanketing in the emission lines of heavy elements and molecular bands increases the amplitudes of the photometric reflection effects by up to a factor of two.

(4) No evidence has been found for the influence of the stellar wind and magnetic fields of the secondaries of MS Peg and LM Com on the structure of their irradiated atmospheres. The absence of emission lines in the spectra of the objects at phases close to $\varphi = 0.0$ indicates that the chromospheres of the red dwarfs themselves do not play a significant role.

(5) There is no global stable mass transport at the surfaces of the red dwarfs with velocities exceeding $V_{trans} = 35$ km/s for MS Peg and $V_{trans} = 60$ km/s for LM Com. However, the fact that the observed duration of the phase of enhanced brightness exceeds the theoretical value by 6–8% may serve as indirect evidence for matter outflow from a hot-spot zone in LM Com.

(6) A $\lambda 3905$ Å emission line whose intensity cannot be explained theoretically in LTE models has been detected in the spectra of both systems. The probable origin of this line is the "superionization" of SiI atoms from weakly excited levels under the action of UV irradiation, with the subsequent re-emission of these photons in cascade-transition lines. Thus, the SiI $\lambda 3905$ Å line has a radiative origin, and can serve as a diagnostic of the presence of external UV irradiation in old PCVs. Further studies are required to investigate the use of this line for the identification of new close-binary systems.

8. ACKNOWLEDGMENTS

The authors are grateful to the Time Allocation Committee for the 6-m telescope for support of their program of studies of close-binary spectra. We thank N.A. Sakhibullin and V.F. Suleĭmanov for useful discussions and A. Pramsky and K.V. Balyakov for their assistance in the observations and preprocessing of the spectra. This work was supported by the Russian Foundation for Basic Research (project codes 99-02-17488 and 02-02-17174) and the Academy of Sciences of the Tatarstan Respublic. V.V. Shimansky additionally thanks the Russian Foundation for Basic Research, which provided him with IAU grants (project codes 02-02-06591 and 01-02-06065).

REFERENCES

1. H. Ritter, Astron. Astrophys. **169**, 139 (1986).
2. R. G. Probst, Astrophys. J., Suppl. Ser. **53**, 335 (1983).
3. R. F. Green, M. Schmidt, and J. Liebert, Astrophys. J., Suppl. Ser. **61**, 305 (1986).
4. J. A. Orosz, R. A. Wade, and J. J. B. Harlow, Astron. J. **114**, 317 (1997).
5. P. F. L. Maxted, T. R. Marsh, and C. K. J. Moran, Mon. Not. R. Astron. Soc. **319**, 305 (2000).
6. H. Ritter and U. Kolb, Astron. Astrophys. (in press).
7. D. H. Ferguson and T. A. James, Astrophys. J., Suppl. Ser. **94**, 723 (1994).
8. D. L. Pollacco and S. A. Bell, Mon. Not. R. Astron. Soc. **262**, 377 (1993).
9. D. L. Pollacco and S. A. Bell, Mon. Not. R. Astron. Soc. **267**, 452 (1994).
10. N. A. Sakhibullin and V. V. Shimansky, Astron. Zh. **74**, 432 (1997) [Astron. Rep. **41**, 378 (1997)].
11. N. A. Sakhibullin and V. V. Shimansky, Odessa Astron. Publ. **10**, 94 (1998).
12. G. P. McCook and E. M. Sion, Astrophys. J., Suppl. Ser. **65**, 603 (1987).
13. D. Tytler and E. Rubenstein, in *IAU Coll. No. 114: White Dwarfs* (Springer, Berlin, 1989), p. 524.
14. G. Schultz, B. Zuckerman, and E. E. Becklin, Bull. Am. Astron. Soc. **25**, 824 (1993).
15. G. Schultz, B. Zuckerman, and E. E. Becklin, Astrophys. J. **460**, 402 (1996).
16. G. D. Schmidt, P. S. Smith, and D. A. Harvey, Astron. J. **110**, 398 (1995).
17. D. H. Ferguson, R. F. Green, and J. Liebert, Astrophys. J. **287**, 320 (1984).
18. J. A. Orosz, R. A. Wade, J. J. B. Harlow, *et al.*, Astron. J. **117**, 1598 (1999).
19. V. L. Afanas'ev, A. N. Burenkov, V. V. Vlasyuk, and S. V. Drabek, Preprint No. 234, 128 (Spec. Astrophys. Obs., Nizhniĭ Arkhyz, 1995).
20. R. C. Bohlin, Astron. J. **111**, 1743 (1996).
21. P. Ballester, *ESO/ST-ECF Data Analysis Workshop 177* (1992).
22. D. V. Ivanova, N. A. Sakhibullin, and V. V. Shimansky, Astron. Zh. **79**, 433 (2002) [Astron. Rep. **46**, 390 (2002)].
23. R. L. Kurucz, SAO CD-ROMs (MA02138, Cambridge, USA, 1994).

24. S. E. Nersisyan, A. V. Shavrina, and A. A. Yaremchuk, Astrofizika **30**, 247 (1989).
25. C. R. Vidal, J. Cooper, and E. W. Smith, Astron. Astrophys., Suppl. Ser. **25**, 37 (1973).
26. A. Unsold, *Physik der Sternatmospheren* (Springer, Berlin, 1955).
27. V. L. Straĭzhis, *Multicolor Stellar Photometry* [in Russian] (Mokslas, Vil'nyus, 1977).
28. P. Bergeron, R. A. Saffer, and J. Liebert, Astrophys. J. **394**, 228 (1992).
29. N. A. Sakhibullin and V. V. Shimansky, Astron. Zh. **73**, 793 (1996) [Astron. Rep. **40**, 723 (1996)].
30. E. Anders and N. Grevesse, Geochim. Cosmochim. Acta **53**, 197 (1989).
31. P. F. L. Maxted, T. R. Marsh, C. K. J. Moran, *et al.*, Mon. Not. R. Astron. Soc. **300**, 1225 (1998).
32. J. H. Wood, E. L. Robinson, and E. H. Zhang, Mon. Not. R. Astron. Soc. **277**, 87 (1995).
33. L. Girardi, A. Bressan, G. Bertelli, *et al.*, Astron. Astrophys., Suppl. Ser. **141**, 371 (2000).
34. J. A. Panei, L. G. Althaus, and O. G. Benvenuto, Astron. Astrophys. **353**, 970 (2000).
35. K. Bern and S. Wramdemark, Lowell Obs. Bull. **8**, 1 (1973).
36. D. H. Ferguson, J. Liebert, S. Haas, *et al.*, Astrophys. J. **518**, 866 (1999).
37. I. J. Iben and M. Livio, Publ. Astron. Soc. Pac. **105**, 1375 (1993).
38. V. V. Shimansky and N. V. Borisov, Astron. Zh. **79**, 450 (2002) [Astron. Rep. **46**, 406 (2002)].
39. D. V. Ivanova, N. A. Sakhibullin, and V. V. Shimansky, Astron. Zh. (in press).
40. A. Kawka, S. Wennes, J. Dupuis, *et al.*, Astron. J. **120**, 3250 (2000).
41. M. J. Seaton, C. J. Zeippen, J. A. Tully, *et al.*, Rev. Mex. Astron. Astrofis. **23**, 19 (1992).
42. R. L. Kurucz, I. Furenlid, J. Brault, *et al.*, *Solar Flux Atlas from 296 to 1300 nm* (Nat. Solar Obs. Sunspot, New Mexico, 1984).
43. C. Cincunegui and P. J. D. Mauas, Astrophys. J. **552**, 877 (2001).

Translated by K. Maslennikov

Astronomy Reports, Vol. 47, No. 9, 2003, pp. 777–788. Translated from Astronomicheskiĭ Zhurnal, Vol. 80, No. 9, 2003, pp. 845–856.
Original Russian Text Copyright © 2003 by Kolotilov, Shenavrin, Shugarov, Yudin.

UBVJHKLM Photometry of the Symbiotic Mira V407 Cyg in 1998–2002

E. A. Kolotilov, V. I. Shenavrin, S. Yu. Shugarov, and B. F. Yudin

Sternberg Astronomical Institute, Universitetskiĭ pr. 13, Moscow, 119992 Russia

Received December 19, 2002; in final form, March 14, 2003

Abstract—New results of $UBVJHKLM$ photometry of the symbiotic Mira V407 Cyg performed in 1998–2002 are reported. In 2002, these observations were supplemented with RI observations and a search for rapid variability in the V band. The hot component of V407 Cyg experienced a strong flare in 1998, which was the second in the history of photometric observations of this star; this flare is still continuing. During the flare, the spectral energy distribution of the hot component can be approximated by blackbody radiation with a temperature of ~7200 K. At the maximum brightness, the bolometric flux from the hot component did not exceed 3% of the Mira's mean bolometric flux, while its bolometric luminosity was $\sim 400 L_\odot$. Appreciable variations of the star's BV brightness ($\sim 0\overset{m}{.}7$) on a timescale of several days have been observed. These variations are not correlated with variations of $B-V$. Flickering on a timescale of several minutes with an amplitude of $\sim 0\overset{m}{.}2$ has been detected in the V band. The observations suggest that the hot component can be in three qualitatively different states. In a model with a rapidly rotating white dwarf, these states can be associated with (i) the quiescent state of the white dwarf (with a very low accretion rate), (ii) an ejection state, and (iii) an accretion state. The Mira pulsation period P is $\approx 762\overset{d}{.}9$, with its infrared maximum occurring $\sim 0.15P$ after the visual maximum. A “step” is observed on the ascending branch of the Mira infrared light curves. In 1998, the gradual increase of the mean K brightness of the Mira that had been observed since 1984 was interrupted by an unusually deep minimum, after which the mean level of the K brightness considerably decreased. *© 2003 MAIK “Nauka/Interperiodica”*.

1. INTRODUCTION

V407 Cyg (AS 453, Nova Cygni 1936) belongs to a small subgroup of symbiotic stars called symbiotic Miras. Symbiotic stars are binary systems in which the cool component is a red giant. If the giant is pulsating, i.e., if it is a Mira, the symbiotic star is called a symbiotic Mira.

V407 Cyg was discovered by Hoffmeister [1], as a nova flare in Cygnus. At the maximum of the flare in August 1936, the photographic magnitude of V407 Cyg was $m_{\rm pg} \approx 14$. Subsequently, the brightness of the star began to decrease slowly, and two years later its photographic magnitude fell to $m_{\rm pg} \approx 16$. Meinunger [2] plotted its light curve and found that, after the flare, the brightness of the star began to pulsate with a period of $P \approx 745^{\rm d}$ and an amplitude of $\Delta M_{pg} \geq 3.5$. The presence of TiO absorption bands in the spectrum suggested that it was a Mira, and the flare of the star indicated that it was a symbiotic Mira.

However, the firm classification of V407 Cyg as a symbiotic star, i.e., a binary system, was made only in 1994. The first spectrum of V407 Cyg, obtained in August 1994, looked typically symbiotic. Intense emission lines of HI, HeI, HeII, NIII [NII], and [OIII] were observed against the background radiation of an M6–M7 red giant [3]. Earlier, only Hα emission had been observed in the spectrum, with this line sometimes being intense [4, 5] and sometimes completely disappearing from the spectrum [6].

A typical symbiotic spectrum for V407 Cyg was observed for the second time in October 1995 [7], when the Mira was in a phase intermediate between the maximum and minimum. At the same time, near its brightness maximum in March 1995, the Mira dominated in the optical, and only the Hα line was visible in the spectrum [7]. We will call this state of the hot component the quiescent state. It differs from the flare in a lower brightness of the hot component and a higher degree of excitation of the spectrum, in particular, the presence of the HeII λ4686 Å line in the spectrum.

We shall call the passive state the state of the hot component when its signatures are completely absent in the optical, even at the minimum brightness of the Mira. BV photometry and spectral observations of V407 Cyg during the passive state of the hot component in June–August 1991 were presented in [3]: $B \approx 17.2$, $B-V \approx 2.05$, $W(\mathrm{H}\alpha) \approx 5$ Å. Note that ultraviolet observations obtained with the IUE Space Observatory in May 1991 with an exposure of about 7 h detected no radiation from V407 Cyg.

Based on the character of the flares of the hot components of symbiotic stars, three subtypes have been distinguished: classical symbiotic stars (prototype Z And), symbiotic novae (prototype V1016 Cyg), and recurrent novae (prototype T CrB). However, the flares of some symbiotic stars do not strongly resemble flares of these subtypes. These stars include such well-known symbiotic stars as CH Cyg, R Aqr, MWC 560, and the less known V407 Cyg.

Observations of V407 Cyg at 1–10-μm detected the presence of dust in the envelope of the star [6]. Accordingly, V407 Cyg can also be classified as a D-type (dusty) symbiotic star. Miras with such long pulsation periods as that of V407 Cyg already have optically thick dust envelopes. However, the dust envelope of the symbiotic Mira V407 Cyg turned out to be optically thin; its structure is studied in detail in [8].

We began *UBVJHKLM* photometric observations of V407 Cyg in 1984. The data for 1984–1997 were published in [3]. In the current paper, we report and analyze similar observations carried out in 1998–2002, during which time the star experienced a second nova-like flare, similar to the flare of 1936. This episode was the main motivation to publish our observations for this time interval. In addition, the increase of the mean level of the Mira's IR brightness observed in 1984–1997 was interrupted by a deep minimum in 1998, when the Mira was its reddest during the entire history of infrared photometric observations of V407 Cyg. In 2002, we also searched for rapid variability (flickering) of the hot component, which had not yet faded at that time. The search was successful, and the results are presented here. Note that we are also performing regular low- and high-resolution spectral observations of V407 Cyg, which will be analyzed in detail in a forthcoming paper.

2. OBSERVATIONS

Photometric observations of V407 Cyg in the *UBVJHKLM* system are carried out on the 0.6-m and 1.25-m telescopes of the Crimean Laboratory of the Sternberg Astronomical Institute (SAI). As standards, we chose star No. 9 from [9] ($U = 11.01$, $B = 10.17$, $V = 9.14$) and BS 8079 ($J = 1.00$, $H = 0.18$, $K = -0.05$, $L = -0.28$, $M = -0.06$). The observational errors in the optical do not exceed $0\overset{m}{.}03$ when the star is brighter than 15^m and can reach $0\overset{m}{.}2$ when the brightness of the star approaches 17^m. The errors in the infrared do not exceed $0\overset{m}{.}02$. The results of the observations are listed in Table 1.

In 2002 we began photometric *BVRI* observations of V407 Cyg with the SBIG ST-7 CCD camera on the 0.6-m telescope of the Crimean Laboratory of the SAI and the 0.38-m telescope of the Crimean Astrophysical Observatory. The field of view of the camera mounted on these two telescopes was $\sim 6'$ and $\sim 10'$, respectively. We chose four reference stars in the field of view: GSC 3588.0042 ($B = 13.67$, $V = 13.01$, $R = 12.40$, $I = 11.70$), 3588.0866b ($V = 14.64$, $R = 12.23$, $I = 10.25$), 3588.3170 ($B = 14.14$, $V = 13.33$, $R = 12.67$, $I = 12.14$), and 3588.1862 ($B = 14.49$, $V = 13.78$, $R = 13.12$). Their magnitudes were estimated relative to the standard GSC 3588.2054 ($B = 12.93$, $V = 12.31$, $R = 11.79$, $I = 11.43$). The results of the observations are presented in Tables 2 and 3. The corresponding errors do not exceed $0\overset{m}{.}02$.

Figure 1 shows light curves of the star plotted for the entire set of our photometric observations. The vertical dashes on the B light curve mark dates of maxima of the Mira's photographic brightness. The hot component of V407 Cyg flared in 1998, when the Mira was near its minimum, which turned out to be appreciably deeper and redder than the previous minimum. At that time, the optical brightness of V407 Cyg appreciably exceeded the Mira's brightness for the given phase of its light curve. The hot component continued to dominate in the UBV radiation of V407 Cyg and in the subsequent brightness minima of the Mira in 2000 and 2002.

3. THE MIRA V407 Cyg

Of the near-infrared spectral bands, the K band is optimal for studies of the pulsations of the Mira, which is surrounded by an optically thin dust envelope, because the K brightness of the star is affected only weakly by changes in the optical depth of the dust envelope [3]. A Fourier analysis of the K light curve of V407 Cyg shows that the dominant harmonic has a period of $P \approx 762\overset{d}{.}9$, and its full amplitude is $\sim 0\overset{m}{.}9$. The dates of the maxima are given by the formula

$$\mathrm{Max}(K) = 2445326 + 762\overset{d}{.}9E. \qquad (1)$$

These dates are marked by vertical dashes on the K light curve. The estimated pulsation periods in the $JHLM$ bands differ from the K-band estimate by no more than 3 days ($\leq 0.4\%$). The full amplitudes of the given harmonics in the $JHLM$ bands are $\sim 1\overset{m}{.}2$, $\sim 1\overset{m}{.}15$, $\sim 0\overset{m}{.}57$, and $\sim 0\overset{m}{.}54$, respectively.

We can see from Fig. 1 that the amplitude of the K brightness variations and the mean level of the Mira's brightness can both change from cycle to cycle. Figure 1 shows the sine-wave fit of the observed light curve corresponding to formula (1); we varied the extreme values of the fit so that it passed through the points of the light curve. In addition, the figure shows the trend of the mean K brightness of the Mira, which we determined as the trend of the sine wave approximating the light curve of the star.

On the (JD, $J-L$) graph, we have plotted a similar sine wave with a constant amplitude equal to $0\overset{m}{.}3$.

Table 1. *UBVJHKLM* photometry of V407 Cyg in 1998–2002

JD 2450000+	*U*	*B*	*V*	*J*	*H*	*K*	*L*	*M*
793				4.67	3.38	2.73	1.97	1.78
980				5.89	4.55	3.62	2.46	
998	14.63	14.63	13.70					
1006				5.95	4.59	3.66	2.50	
1010	15.04	14.88	13.78					
1011	14.81	14.54	13.63					
1016	14.69	14.76	13.55					
1020	14.91	14.75	13.66					
1033				5.95	4.43	3.66	2.48	2.13
1038				5.93	4.53	3.64	2.43	2.24
1060				5.84	4.48	3.62	2.43	2.14
1069				5.79	4.49	3.62	2.43	2.14
1093				5.55	4.31	3.45	2.29	1.99
1105	13.92	13.78	12.65					
1111		13.50	12.38					
1124				5.71	4.37	3.45	2.32	1.90
1141				5.55	4.41	3.47	2.34	2.11
1152				5.51	4.38	3.46	2.37	2.02
1161	13.55	13.51	12.42					
1164	13.51	13.48	12.41					
1180				5.46	4.29	3.46	2.32	2.01
1359				4.57	3.37	2.77	1.92	1.74
1365				4.57	3.40	2.74	1.94	1.75
1367	13.30	13.21	11.84					
1369	13.47	13.42	12.03					
1375	13.20	13.26	11.90					
1383				4.56	3.32	2.74	1.91	1.71
1387				4.54	3.30	2.71	1.88	1.71
1399	13.00	13.22	12.00					
1420				4.53	3.31	2.67	1.85	1.74
1434	13.43	13.44	12.22					
1439	13.45	13.44	12.23					
1449				4.52	3.24	2.64	1.87	1.75
1455	13.60	13.59	12.42					
1475				4.58	3.29	2.73	1.94	1.68
1494	13.61	13.63	12.61					
1505				4.65	3.34	2.74	1.94	1.86
1532				4.75	3.44	2.74	1.97	1.99
1549				4.80	3.48	2.83	2.02	2.00
1552	13.60	13.60	12.50					
1678	13.70	13.66	12.56					

Table 1. (Contd.)

JD 2450000+	U	B	V	J	H	K	L	M
1720	13.81	13.83	12.72					
1742				5.91	4.44	3.59	2.56	2.45
1762	13.88	13.82	12.84					
1767				5.83	4.46	3.60	2.54	2.33
1770				5.84	4.38	3.53	2.50	2.38
1773				5.78	4.42	3.55	2.49	2.39
1778				5.70	4.34	3.50	2.48	2.31
1780				5.68	4.31	3.46	2.43	2.30
1802				5.60	4.30	3.45	2.43	2.29
1824				5.52	4.24	3.43	2.38	2.18
1848				5.42	4.18	3.39	2.36	2.14
1864	14.34	14.23	13.15	5.44	4.20	3.39	2.38	2.19
1903				5.49	4.23	3.44	2.41	2.22
2095				4.65	3.43	2.83	2.07	1.96
2115	14.10	13.95	12.26					
2117				4.61	3.38	2.81	2.01	1.87
2122	14.32	14.07	12.43					
2125				4.62	3.34	2.74	2.03	1.92
2132	14.61	14.28	12.68					
2134	14.46	14.18	12.61					
2153				4.59	3.30	2.72	2.01	1.94
2164	14.63	14.35	13.08					
2178	14.57	14.46	12.99					
2187				4.56	3.28	2.70	1.98	1.99
2195	14.76	14.51	13.16					
2210				4.57	3.28	2.70	1.98	1.90
2220				4.59	3.30	2.70	1.99	1.93
2224	14.24	14.30	13.16					
2405	14.13	14.16	13.12					
2406	14.51	14.60	13.57					
2407		14.58	13.44					
2420				5.38	4.20	3.42	2.50	2.36
2440	14.62	14.62	13.67					
2441	14.54	14.65	13.54					
2450				5.58	4.20	3.42	2.50	2.36
2462	14.43	14.36	13.32					
2486				5.78	4.38	3.55	2.52	2.46
2488		14.61	13.54					
2510				5.88	4.50	3.62	2.57	2.53
2536				5.86	4.47	3.63	2.54	2.53
2565				5.73	4.38	3.57	2.50	2.50
2597				5.45	4.16	3.41	2.40	2.39

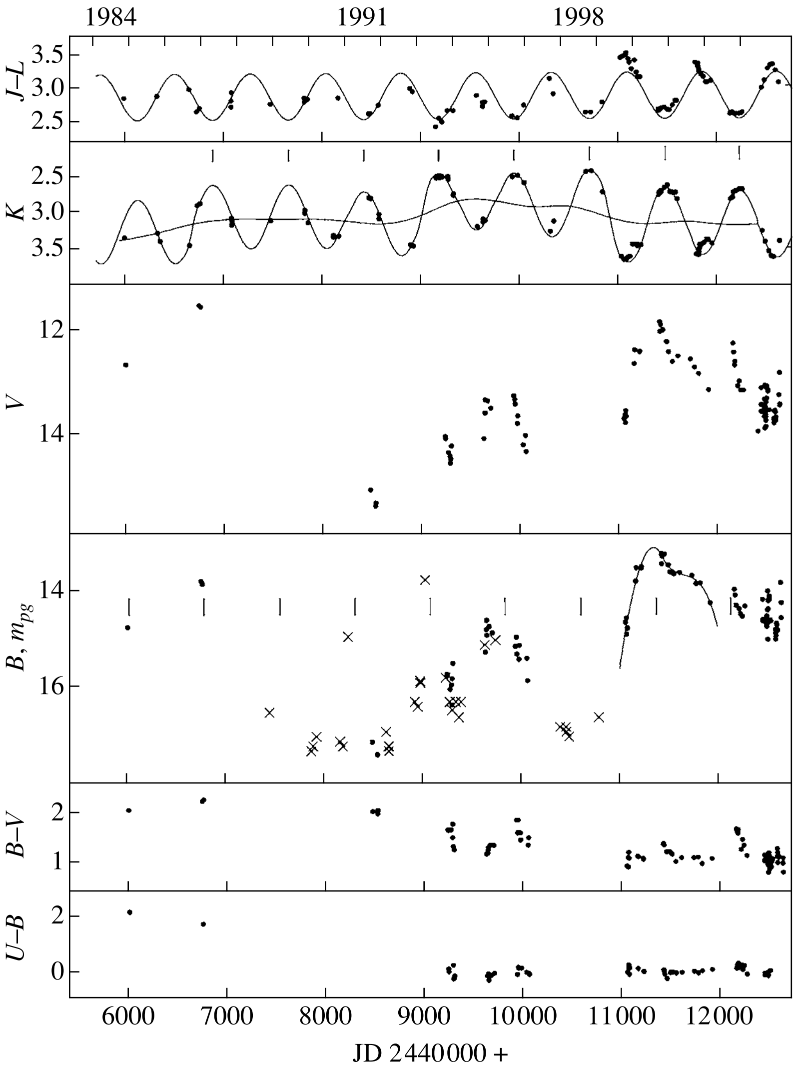

Fig. 1. Variations of the brightness of V407 Cyg in B, V, and K and of the $U-B$, $B-V$, and $J-L$ color indices. The crosses on the (JD, B) plot denote estimated photographic magnitudes of V407 Cyg. The vertical dashes on the (JD, K) plot denote the dates of IR brightness maxima of the Mira calculated using (1), while the vertical dashes on the (JD, B) plot indicate dates of maxima of its optical brightness. For a description of the solid curves, see the text.

This is the amplitude of the harmonic with $P \approx 762\overset{\rm d}{.}9$ in the variations of the $(J-L)$ color of the star. This color index is affected only weakly by variations in the Mira's luminosity and is a sensitive indicator of changes of its temperature and/or of the optical depth of the dust envelope [3].

The convolved K light curve demonstrates that the pulsations are not purely harmonic. Therefore, we searched for the Mira pulsation period using software developed by Yu.K. Kolpakov (http://infra.sai.msu.ru/prig/kolpakov). The method used to search for the periodicity consists of fitting the given time series with a composite multiterm function, whose polynomial part (a third-order polynomial) restores the cubic trend of the constant component of the signal, with the Fourier series expansion being carried out to the third harmonic. The coefficients of the approximating polynomial are found via a least-squares fit. The period is $\sim 762.2^{\rm d}$; i.e., it virtually coincides with the period of the dominant harmonic. The initial phase of the K brightness maximum also coincides (within one day) with the phase given in (1).

Figure 2 shows the convolved K light curve and $J-L$ color-index curve corresponding to (1) after removing the trend using Kolpakov's software. This software also plots curves approximating the above convolutions. We can see from Fig. 2 that the minimum brightness and maximum reddening occur at phase $\varphi \approx 0.4$. There is a step in the ascending branch of both curves, which appears due to a delay in the increase of the K brightness and a decrease

Table 2. $BVRI$ photometry of V407 Cyg in 2002

JD 2450000+	B	V	R	I
2374		13.95	11.33	7.57
2407	14.58	13.44	11.28	7.79
2439		13.34	11.23	8.02
2442		13.07	11.27	8.06
2445	14.69	13.89	11.44	8.11
2447	14.51	13.48	11.31	8.09
2448	14.72	13.59	11.33	8.09
2449	14.71	13.51	11.37	8.13
2450	14.67	13.61	11.39	8.13
2451	14.57	13.62	11.41	8.12
2453	14.61	13.68	11.45	8.14
2454	14.65	13.75	11.44	8.15
2455	14.38	13.39	11.30	8.14
2456	14.99	13.86		8.15
2459	13.99	13.12	11.25	8.24
2461	14.19	13.08	11.26	8.23
2472	14.09	13.19	11.30	8.34
2475	14.16	13.15	11.32	8.33
2536	14.99	13.71	11.61	8.46
2537	14.85	13.73	11.58	8.45
2538	14.78	13.79	11.63	
2539	14.91	13.71	11.62	8.43
2541		13.57	11.48	8.40
2548	14.66	13.55	11.52	8.39
2551	14.69	13.58	11.51	8.36
2555		13.75	11.57	8.41
2557	14.79	13.68	11.54	8.31
2587		13.25	10.98	7.85
2592	13.82	12.83	10.82	7.71
2595	14.54	13.45	10.94	7.77
2598	14.23	13.43	10.82	7.63

Table 3. V photometry of V407 Cyg on June 20, 2002

UT	$V_{\rm V407\ Cyg}$	$V_{\rm st}$	UT	$V_{\rm V407\ Cyg}$	$V_{\rm st}$
$0.5742^{\rm n}$	13.934	13.820	1.8558	13.860	13.825
0.6462	13.925	13.813	1.8918	13.828	13.820
0.7230	13.925	13.807	1.9254	13.797	13.819
0.9078	13.948	13.812	1.9614	13.823	13.821
0.9894	13.987	13.815	1.9974	13.827	13.816
1.0350	13.869	13.813	2.0310	13.836	13.813
1.0686	13.832	13.816	2.0670	13.852	13.815
1.1046	13.823	13.817	2.1030	13.883	13.816
1.1406	13.818	13.827	2.1366	13.910	13.826
1.1742	13.832	13.819	2.1726	13.866	13.810
1.2102	13.888	13.810	2.2086	13.830	13.811
1.2462	13.872	13.818	2.2422	13.881	13.821
1.2798	13.905	13.818	2.2782	13.752	13.818
1.3158	13.925	13.817	2.3118	13.718	13.811
1.3518	13.891	13.817	2.3478	13.721	13.815
1.3854	13.933	13.806	2.3838	13.735	13.813
1.4214	13.920	13.815	2.4174	13.737	13.814
1.4550	13.916	13.816	2.4534	13.805	13.814
1.4910	13.923	13.814	2.4894	13.747	13.808
1.5270	13.925	13.810	2.5230	13.724	13.822
1.5606	13.966	13.816	2.7678	13.766	13.815
1.5966	13.948	13.815	2.8086	13.699	13.813
1.6326	13.930	13.807	2.8470	13.663	13.817
1.6662	13.896	13.808	2.8854	13.747	13.818
1.7022	13.869	13.830	2.9238	13.725	13.897
1.7382	13.838	13.822	3.0486	13.819	13.805
1.8006	13.990	13.811	3.1398	13.752	13.815

in the (J–L) color of the Mira. This feature of the light curve is characteristic of many Miras but is not always present [10, 11].

The step in the convolved light curve is observed at phases $\varphi \approx 0.55$–0.70, and the step in the convolved color index curve occurs at $\varphi \approx 0.60$–0.75. In view of the wide scatter of the points near the step in both diagrams, we can conclude that the delays in the variations of the K brightness and (J–L) color take place synchronously. We associate the delay in the Mira's brightness and color variations with a delay in the variations of its bolometric luminosity and temperature.

The amplitude of the J–L color-index variations along the fitted curve is $\sim 0\overset{m}{.}76$ and corresponds to a change of the color temperature by $\sim$350 K. At the same time, the K brightness changes by $\sim 0\overset{m}{.}92$, which corresponds to a change of the bolometric magnitude of $\Delta m_{\mathrm{bol}} \approx 0.8$ [8]. The amplitude of the change of m_{bol} from the Mira's brightest maximum in 1997 to its deepest minimum in 1998 (Fig. 1) was $\sim 1\overset{m}{.}1$. When estimating the bolometric flux, we plotted the spectral energy distribution at 12–60-μm using IRAS data (for details see [8] and references therein).

Figure 1 shows that the mean level of the Mira's brightness was gradually increasing from 1984 to 1998. However, in 1998, the light minimum was as deep as it had been in 1984–1985, judging from the fitted sine wave. At the same time, the J–L color index took on its largest value, so that, accordingly, the color temperature was its lowest. Figure 3 shows that the $J-L = f(K)$ relationship has become steeper since 1998. The linear fits yield $J-L \approx 0.37K + 1.61$ before 1998 and $J-L \approx 0.81K + 0.42$ after 1998. The change in the slope is due to the fact that the J–L color index has appreciably increased near the brightness minimum ($K = 3.5$–3.6) since 1998, whereas it has not changed near the brightness maximum (Fig. 3).

If we take the B light curve of V407 Cyg for 1984–1997 (i.e., before the strong flare of the hot component) and convolve it with the period $762\overset{d}{.}9$, we find that the maximum of the Mira's photographic brightness precedes its K maximum by $\sim 0.15P$ (i.e., $\phi \approx \varphi + 0.15$; ϕ is the phase of the Mira's photographic brightness). This behavior is fairly typical of Miras [10, 11]. The dates of the maxima of the Mira's photographic brightness are marked on the B light curve (Fig. 1) by vertical bars.

The estimated period of the Mira's pulsations derived from the photographic light curve for 1935–1960 is $\sim 745^{\mathrm{d}}$ [2]. However, due to the restricted number of brightness estimates (most are upper limits), we cannot be sure that the Mira's period had changed by the beginning of our observations, though such behavior has been observed in some Miras (see [12] and references therein).

4. THE FLARE OF THE HOT COMPONENT OF V407 Cyg

The flare of V407 Cyg began in the first half of 1998. The first observations of the star on July 7, 1998, showed it to be unusually bright for the corresponding phase of the Mira's cycle ($\phi \approx 0.59$). In July, the mean brightness and color of the star were $\langle B\rangle \approx 14.7$, $\langle B{-}V\rangle \approx 1.05$, and $\langle U{-}B\rangle \approx 0.10$. Earlier, in October 1997, at phase $\phi \approx 0.22$, the photographic brightness of V407 Cyg was $m_{\mathrm{pg}} \approx 16.6$. This means that the hot component was still in the passive state at that time [3]. In the following in-

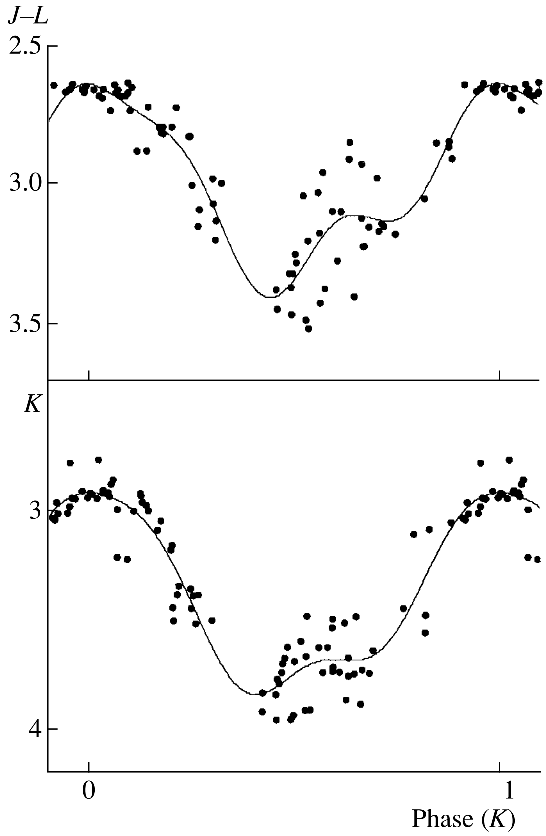

Fig. 2. K light curve and J–L color curve convolved with a period of 762.9 d after removing the trend (see text for details).

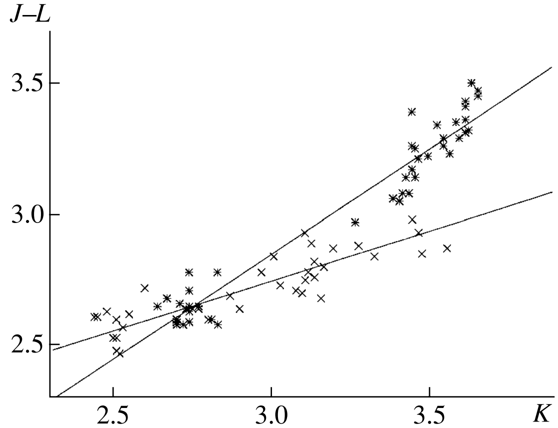

Fig. 3. The (K, J–L) plot. The crosses and asterisks show the data for 1984–1997 and 1998–2002, respectively. The straight lines show linear approximations to the given dependence separately for these two time intervals.

terval, the Mira was progressing toward its minimum brightness. Therefore, if the hot component had not been activated, the brightness of V407 Cyg should not have increased until July 1998. Note that the Hα line was barely visible in our low- and high-resolution spectra obtained in the autumn of 1997, whereas it was very intense in July 1998. At the same time, the HeII λ4686 Å line was not detected and was absent in the spectrum of V407 Cyg until the end of the autumn of 2002.

During the three months from July to October, the brightness of V407 Cyg increased by $\sim 1^m$ ($\langle B \rangle \approx$ 13.7 and 13.6 in October and December 1998 respectively), while the $B-V$ and $U-B$ color indices did not change appreciably. During the Mira's brightness minimum in May–June 2000, the mean B magnitude of V407 Cyg was $\langle B \rangle \approx 13.7$; in November 2000 ($\phi \approx$ 0.72), it was $\langle B \rangle \approx 14.2$, and it was $\langle B \rangle \approx 14.5$ during the Mira's brightness minimum in July–August 2002. Thus, the flare of the hot component has not ended, and the hot component continues to dominate in the UBV range near the Mira's minimum brightness. The mean color indices of the hot component are: $((B-V)_{\rm hot} \approx 1.06$ and $(U-B)_{\rm hot} \approx 0.03$.

Thus, the second of the two recorded flares of the hot component has already continued for two periods of the Mira's pulsations, over ~ 4 years. During the flare of 1936, the hot component faded after two years [1, 2], and it was $\sim 0\overset{m}{.}8$ fainter in photographic light (B band) at the brightness maximum.

We recorded the maximum brightness of V407 Cyg in July–August 1999 ($B \approx 13.3$), near the phase of the Mira's brightness maximum (Fig. 1). We can see from Fig. 1 that the Mira's photographic brightness can vary from maximum to maximum by at least 1^m. In the bright maxima of 1984 and 1992, its B magnitude was $B \approx 13.8$, so that its brightness at that time was comparable to the maximum brightness of V407 Cyg in July–August 1999. However, the mean color index in July–August 1999 was $U-B \approx -0\overset{m}{.}01$. This means that the hot component was dominating in both U and B at that time, $B \approx B_{\rm hot} \approx 13.3$. We have approximated the B light curve of V407 Cyg during 1998–2000 with a sixth-order polynomial, shown by the solid curve in Fig. 1. Its maximum corresponds to $B \approx 13.1$. The polynomial reflects changes of the mean brightness of the hot component. We use separate segments to indicate the mean brightness level of the hot component in December 2001 ($B \approx 14.3$) and in 2002 ($B \approx 14.6$), when it dominated the B light of V407 Cyg (Fig. 1), judging from the $U-B$ color index.

Thus, the B brightness of the hot component of V407 Cyg was $\sim 13\overset{m}{.}3$ in July–August 1999. In this case, in accordance with its color index $B-V)_{\rm hot}$, its V magnitude was $V_{\rm hot} \approx 12.24$, and, accordingly, the Mira's V magnitude was $V_{\rm cool} \approx 13.4$. Thus, the Mira's visual brightness during the maximum of 1999 was $\sim 0\overset{m}{.}8$ fainter than in the low-brightness maximum of 1986 (Fig. 1).

During the Mira's maximum brightness in July–August 2001, the mean color index was $U-B \approx 0.3$, which exceeded the value of $(U-B)_{\rm hot}$ by $\sim 0\overset{m}{.}23$. Since this difference is not large and the Mira's brightness falls off steeply with decreasing wavelength, we can suppose that the hot component dominated in the U band at that time. In this case, we can calculate its BV magnitudes and then calculate the Mira's magnitudes in these bands. These are $B_{\rm cool} \approx 15.8$, $V_{\rm cool} \approx 13.3$. Accordingly, the Mira's color index $B-V)_{\rm cool}$ is ≈ 2.5.

Thus, during the Mira's maximum of 2001, its brightness was also below the values we had recorded earlier in the maxima of 1984, 1986, 1990, and 1992 (Fig. 1), and its color became slightly redder. The lowered brightness of the Mira V407 Cyg with respect to its "normal" value during the maxima of 1999 and 2000 is not a unique event for this star [2, 13]. Moreover, the same behavior has been observed twice for the symbiotic Mira R Aqr, which is similar to V407 Cyg in many respects.

The maximum visual brightness of R Aqr in its "normal" bright state varies irregularly within 6^m–7^m [14, 15]. However, during the flare of its hot component in 1928–1934, when the amplitude of the brightness variations of R Aqr accordingly decreased, the maximum visual magnitude of the star fell to 8^m [14]. If we take into account that the hot component dominated in the visual at that time [16], the Mira's maximum brightness decreased with respect to its "normal" value by more than 1^m. As the hot component "faded" in 1934, the first maximum of the Mira was $\sim 9^m$, and only after two subsequent maxima did the Mira's brightness at this phase return to its "normal" level.

An overall decrease of the brightness of the Mira R Aqr by $\sim 1^m$ was observed in 1974–1980, in the absence of any activity of the hot component [14, 15]. Both in the former and in the latter case, this phenomenon is associated with screening of the Mira by a dust cloud. In the case of V407 Cyg, the observed behavior was connected with nonsphericity of the circumstellar dust envelope of the Mira, due to the binarity of the star [13].

According to the above estimates, during the maxima of 1999 and 2001, the Mira's $B-V)_{\rm cool}$ color index exceeded the values recorded during the maxima of 1984 and 1986 by $\sim 0\overset{m}{.}3$ (Fig. 1). This may confirm that the additional attenuation of the brightness of the Mira V407 Cyg is connected with the appearance of additional dusty material in the line of sight. If the circumstellar dust grains have similar optical parameters to those of interstellar dust, the observed enhanced reddening of the star corresponds to a decrease of the B brightness by $\sim 1\overset{m}{.}2$.

The degree of interstellar reddening toward V407 Cyg has not been precisely established. Its maximum value, estimated from the Mira's optical spectral energy distribution (SED), corresponds to the color excess $E(B-V) \approx 0.7$ [3]. According to our estimates, the equivalent width of the interstellar KI λ7699 Å absorption line in the spectrum of V407 Cyg corresponds to this color excess. With this color excess and the color indices $(U-B)_0 \approx -0.42$ and $B-V)_0 \approx 0.36$, the flaring hot component of V407 Cyg can formally be classified as a supergiant of spectral types A0 and F5, respectively.

At the same time, these color indices correspond to a source of blackbody radiation with a temperature of $\sim$7200 K. Let us suppose that the color temperature of the hot component at wavelengths $\lambda \geq 0.6$ μm is also close to 7200 K. In this case, the total flux of the hot component during the maximum of July–August 1999 at wavelengths $\lambda \geq 0.36$ μm was $\sim 2.2 \times 10^{-6}$ erg cm^{-2} s^{-1}.

To estimate the bolometric flux of the hot component during the flare, we must know its flux in the ultraviolet. At present, the only way to estimate the UV flux consists in finding an appropriate analog for the hot component of V407 Cyg. One possible analogue is the hot component of CH Cyg. During the flare of 1982–1984, its $B-V)_0$ and $(U-B)_0$ color indices were approximately the same, as for the flaring hot component of V407 Cyg. At the same time, the UV SED was similar to that of an A supergiant with an effective temperature of $\sim$9000 K [17]. The maximum in the SED was at the long-wavelength edge of the IUE spectrum ($\lambda \approx 3200$ Å). Note also that Merrill [16] associated the flaring hot component of the symbiotic Mira R Aqr with a Bep star.

To estimate the energy flux in the UV, we use blackbody curves for temperatures of 10 000, 15 000, and 20 000 K. Replacing these with the SEDs of A–B supergiants will not change our conclusions and would only give the illusion of improving the accuracy of the estimated UV flux.

Thus, we assume that the SEDs of the flaring hot component at $\lambda \leq 0.36$ μm and $\lambda \geq 0.36$ μm are given by blackbody curves for temperatures of 1.5×10^4 and 7200 K, respectively. During the brightness maximum in July–August 1999, the U magnitude of the hot component was $U_0 \approx 10.0$. In this case, the bolometric flux of the hot component was $F_{\rm hot,bol} \approx 4.0 \times 10^{-9}$ erg cm^{-2} s^{-1}, or $\sim$3% of the Mira's mean bolometric flux, which, with the given value of $E(B-V)$, is estimated to be $\sim 13.9 \times 10^{-8}$ erg cm^{-2} s^{-1}. If we decrease the temperature of the source of blackbody radiation to 10^4 K (or increase it to 2×10^4 K), the estimated bolometric flux of the hot component will decrease (increase) by $\sim$30%.

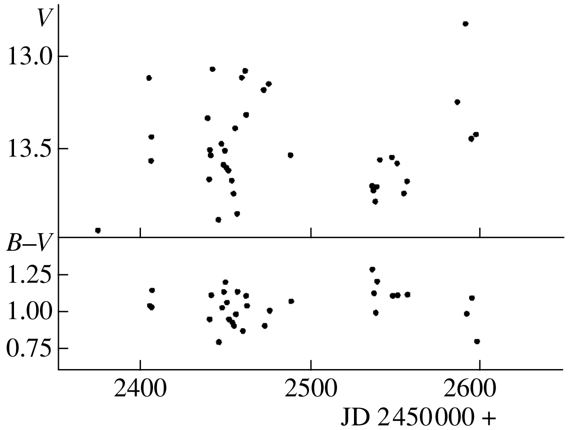

Fig. 4. Curves of the V brightness and $(B-V)$ color index of V407 Cyg in 2002.

In August 1994, when the λ4686 Å HeII line was detected in the spectrum of V407 Cyg, the temperature of the hot component was $\sim 6 \times 10^4$ K, and its bolometric flux (for $E(B-V) \approx 0.7$) was $\sim 2.5 \times 10^{-9}$ erg cm^{-2} s^{-1} [3]. Thus, if we measure the increase of the bolometric flux from the given quiescent state of the hot component, the bolometric flux increased during the flare by a factor of $\sim$1.6. Meanwhile, the U flux grew by a factor of $\sim$3.6. The disproportionate growth of these quantities is due to the fact that the temperature of the hot component of V407 Cyg decreased during the flare, and the maximum in the SED is shifted toward longer wavelengths.

The small increase of the bolometric luminosity of the hot component during the flares and the absence of the proportionality indicated above is also observed in a number of classical symbiotic stars (Z And, CI Cyg, AX Per) [18, 19]. The temporal characteristics of the flare of V407 Cyg are also similar to those of the flares of classical symbiotic stars.

In the quiescent state, the hot components of classical symbiotic stars have maximum temperatures that are sufficiently high to excite the HeII line, and their spectrum looks purely symbiotic. The hot component of V407 Cyg was detected in this state in 1994 and 1995, as is indicated above. However, the hot components of classical symbiotic stars in their quiescent state have luminosities comparable to the luminosities of their red giants [19]. The luminosity of

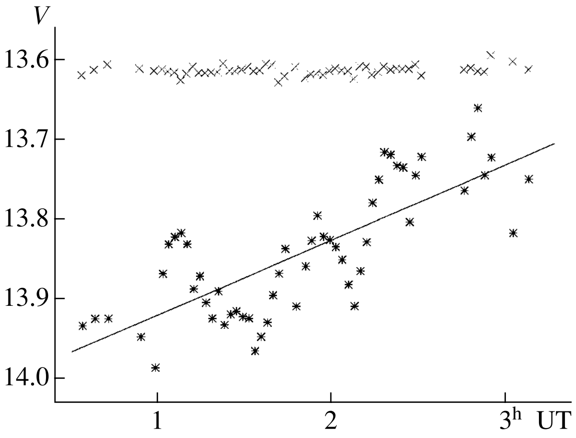

Fig. 5. V light curves of V407 Cyg (asterisks) and of the comparison star GSC 3588.1862 (crosses) on June 20, 2002. The light curve of GSC 3588.1862 has been shifted in the vertical direction by $-0\overset{m}{.}2$.

the hot component of V407 Cyg is only ~3% of the mean luminosity of the Mira. The same is true of the hot component of CH Cyg.

The third state of the hot component of V407 Cyg, which we call the passive state, is characterized by the Mira dominating in the optical, even when its brightness is minimum, and the UV radiation from V407 Cyg cannot be detected at all (see the Introduction). Classic symbiotic stars have no such third state.

5. RAPID VARIABILITY OF THE BRIGHTNESS OF THE HOT COMPONENT

Figure 4 shows the V light curve of V407 Cyg in 2002. We can see that the brightness of the star experiences appreciable changes over a day. In particular, we have recorded two episodes when the magnitude of V407 Cyg changed by $\sim 0\overset{m}{.}75$ in three days. The amplitudes of the B and V variations are approximately the same, and they are well correlated (the correlation coefficient is ~0.93). At the same time, the correlation coefficient for variations of the V brightness and $(B-V)$ color index is ~0.22, and, accordingly, the $(V, B-V)$ plot forms a cloud of points. The full amplitude of the variations of $B-V$ is $\sim 0\overset{m}{.}5$, and the error of this estimate (rms deviation of the estimated color index) does not exceed $0\overset{m}{.}05$.

Figure 5 shows V light curves of V407 Cyg and of the comparison star GSC 3588.1862 obtained within the one night of June 20, 2002. The integration time was 2 min, and the mean interval between brightness estimates was ~3 min. The observations were carried out over ~2.5 hours. The rms deviation of the individual brightness estimates for the comparison star from the mean value is $\sigma \approx 0\overset{m}{.}006$.

We can see from Fig. 5 that the brightness of V407 Cyg changes appreciably on timescales of minutes and hours. In particular, the mean brightness of V407 Cyg (solid curve in Fig. 5) increased by $\sim 0\overset{m}{.}2$ during our observations, while the difference between the maximum and minimum brightnesses was $\sim 0\overset{m}{.}3$. The mean time interval between the brightness peaks was ~8 min.

At present, flickering has been detected only in a few symbiotic stars, including the two recurrent novae RS Oph and T CrB, the two peculiar symbiotic systems CH Cyg and MWC 560, which are similar to V407 Cyg in many respects, the classical symbiotic star Z And, and Mira Ceti (see [20] and references therein). Flickering is inherent to almost all cataclysmic variables and is considered to provide observational confirmation of the presence of an accreting white dwarf as the hot component of these binary systems.

A model with a rapidly rotating magnetic white dwarf has been used to explain the photometric and spectral parameters of the activity of the hot components in CH Cyg and MWC 560 (see [21] and references therein). In this model, the magnetic rotator can be in three states, depending on the rate of accretion of material from the red giant: a passive state, ejection state, and accretion state. In the case of V407 Cyg, it is natural to associate these three states with the three states of its hot component described above.

A Fourier analysis of the light curve of V407 Cyg formally finds two harmonics with periods of $P \approx 18$ and 33 min and full amplitudes of $\sim 0\overset{m}{.}1$. Future observations should elucidate whether oscillations with any of these periods are preserved. Similar oscillations with periods of $P \approx 8.8, 70$, and 28 min were detected in CH Cyg [22], MWC 560 [22], and Z And [23], respectively. These are associated with the rotation of the white dwarf.

6. CONCLUSIONS

Thus, the hot component of the symbiotic Mira experienced its second strong flare in the history of photometric observations of V407 Cyg in 1998, the first flare being in 1936. The flares are certainly associated with accretion. If we suppose that the accretion rate changes due to a significant eccentricity of the orbit of this binary system, the period of its revolution (the interval between the flares) is ~66 years.

V407 Cyg is essentially an analog of the famous symbiotic Mira R Aqr, with the period of pulsations of its cool component being ~387 d and the presumed orbital period being ~44 years [15]. Its hot component has also been observed to be in three states similar to those of the hot component of V407 Cyg

[16]. In the quiescent (in our terminology) state, the hot component of R Aqr is classified as the nucleus of an Ofp planetary nebula, while it is classified as a Bep star during flares.

In the case of CH Cyg, the degree of excitation of its emission-line spectrum also decreases appreciably during flares of its hot component. In particular, the HeII $\lambda 1640$ Å line and NV, SiIV, CIV resonant lines disappear [22]. The parameters of the flares of V407 Cyg and CH Cyg are fairly similar. In particular, the bolometric luminosity of the flaring hot component of CH Cyg comprises only several percent of the luminosity of the red giant [24]. Furthermore, the hot components of both stars demonstrate flickering. This subgroup of symbiotic stars, which could be called R Aqr-type symbiotic stars, should probably also include MWC 560.

In our view, the lack of a passive state for the hot components of classical symbiotic stars can be explained by the fact that these hot components have fairly high intrinsic luminosities, similar to the nuclei of young planetary nebulae. In other words, the white dwarf in a classical symbiotic star (i.e., a degenerate helium or oxygen-carbon core) still has a sufficiently massive hydrogen envelope to sustain hydrogen burning. This envelope can be fed by the accretion of material from the red giant, and we note in this connection that the orbital periods of classical symbiotic stars do not exceed 2.5 years.

The hot components of R Aqr-type stars are white dwarfs with low intrinsic luminosities. In addition, in the case of the CH Cyg system, there are good reasons to suppose that its hot component is a rapidly rotating, magnetic white dwarf (see [21] and references therein). In the magnetic-rotator model for the hot components of R Aqr-type stars, the three states (passive, quiescent, and flaring) can be associated with the passive state (a very low accretion rate), the ejection state, and the accretion state of the white dwarf, respectively.

To estimate the power of the flare of the hot component of V407 Cyg, we must know the distance to the star. If we use the period–bolometric luminosity (P, L) dependence for oxygen-rich Miras [25] for this purpose, this yields the distance estimate ~ 1.7 kpc. The mean bolometric luminosity of the Mira is $\sim 1.2 \times 10^4 L_\odot$ ($M_{\rm bol} \approx -5.5$), and the maximum luminosity of the hot component during the flare is $\sim 400 L_\odot$. Assuming an effective temperature for the M6 red giant of ~ 3000 K, we find that the radius of the Mira V407 Cyg at the mean brightness is $\sim 420 R_\odot$. This value significantly exceeds the size of the Roche lobe of the red giant of a classical symbiotic star.

We have found an intense line of the lithium LiI $\lambda 6708$ Å doublet in a high-resolution spectrum of V407 Cyg [26]. This means that the Mira V407 Cyg is in a quite definite evolutionary stage, called the "hot bottom burning" (HBB) stage. In this case, the absolute bolometric magnitude $M_{\rm bol}$ should be from ≈ -6 to ≈ -7 [27]. Accordingly, the estimated bolometric luminosity of the hot component during its flare could be a factor of 1.5–4 higher than the value given above.

ACKNOWLEDGMENTS

The authors are grateful to V.P. Goranskiĭ and S.V. Antipin for help with the CCD observations and data processing. This work was supported by the Russian Foundation for Basic Research (project codes 02-02-16235, 02-02-17524, and 02-02-16462).

REFERENCES

1. C. Hoffmeister, Veroff. Sternw. Sonnebrerg. **1**, 295 (1949).
2. L. Meinunger, Mitt. Veranderl. Sterne. **87**, 111 (1966).
3. E. A. Kolotilov, Y. Munari, A. A. Popova, *et al.,* Pis'ma Astron. Zh. **24**, 526 (1998) [Astron. Lett. **24**, 451 (1998)].
4. K. M. Merrill and C. G. Burwell, Astrophys. J. **112**, 72 (1950).
5. G. Welin, Astron. Astrophys., Suppl. Ser. **9**, 183 (1973).
6. V. F. Esipov, O. G. Taranova, and B. F. Yudin, Astrofizika **29**, 285 (1986).
7. U. Munari and T. Zwitter, Astron. Astrophys. **383**, 188 (2002).
8. B. F. Yudin, Astron. Zh. **76**, 198 (1999) [Astron. Rep. **43**, 167 (1999)].
9. A.U. Landolt, Publ. Astron. Soc. Pac. **87**, 379 (1975).
10. G. W. Lockwood and R. F. Wing, Astrophys. J. **169**, 63 (1971).
11. A. E. Nadzhip, A. M. Tatarnikova, V. I. Shenavrin, *et al.,* Pis'ma Astron. Zh. **27**, 376 (1999).
12. P. A. Whitelock, New Astron. Rev. **43**, 437 (1999).
13. U. Munari, R. Margoni, and R. Stagni, Mon. Not. R. Astron. Soc. **242**, 653 (1990).
14. J. A. Mattei and J. Allen, J. R. Astron. Soc. Can. **73**, 173 (1979).
15. L. A. Willson, P. Garnavich, and J. A. Mattei, Inform. Bull. Var. Stars, No. 1961 (1981).
16. P. W. Merrill, Astrophys. J. **81**, 312 (1935).
17. J. Mikolajewska, P. L. Selvelli, and M. Hack, Astron. Astrophys. **198**, 150 (1988).
18. A. A. Boyarchuk, Astron. Zh. **44**, 1016 (1967).
19. B. F. Yudin, Astrophys. Space Sci. **135**, 143 (1987).
20. J. L. Sokoloski, L. Bildsten, and W. C. G. Ho, Mon. Not. R. Astron. Soc. **326**, 553 (2001).
21. T. Tomov, D. Kolev, U. Munari, and A. Antov, Mon. Not. R. Astron. Soc. **278**, 542 (1996).
22. M. Mikolajewski, T. Tomov, A. Dapergolas, and Y. Bellas-Veldis, in *Cataclysmic Variables and Related Objects,* Ed. by A. Evans and J. H. Wood (Kluwer, Dordrecht, 1996), p. 341.

23. J. L. Sokoloski and L. Bildsten, Astrophys. J. **517**, 919 (1999).
24. A. P. Ipatov, O. G. Taranova, and B. F. Yudin, Astron. Astrophys. **135**, 325 (1984).
25. E. A. Olivier, P. Whitelock, and F. Marang, Mon. Not. R. Astron. Soc. **326**, 490 (2001).
26. A. M. Tatarnikova, P. M. Marrese, U. Munari, *et al.,* Pis'ma Astron. Zh. (in press).
27. I. J. Sackmann and A. I. Boothroyd, Astrophys. J. **392**, L71 (1992).

Translated by G. Rudnitskiĭ

Astronomy Reports, Vol. 47, No. 9, 2003, pp. 789–796. Translated from Astronomicheskiĭ Zhurnal, Vol. 80, No. 9, 2003, pp. 857–864.
Original Russian Text Copyright © 2003 by Vereshchagin, Reva, Chupina.

The Structure of Proper-Motion Diagrams for Nearby Stars

S. V. Vereshchagin, V. G. Reva, and N. V. Chupina

Institute of Astronomy, Russian Academy of Sciences, Pyatnitskaya ul. 48, Moscow, Russia

Received December 9, 2002; in final form, March 14, 2003

Abstract—The structure of the proper-motion diagrams for an ensemble of nearby field stars is analyzed using a simple model. For comparison, the observed proper-motion diagram is constructed using data of the Hipparcos catalog. A complete description is given of the modification of the van Altena method, which allows stars with similar space motions to be identified based on their proper motions. In the original version of this method, the stars had to be located within one-quarter of the celestial sphere, whereas our version is free of this restriction. *© 2003 MAIK "Nauka/Interperiodica".*

1. INTRODUCTION

Van Altena [1] developed a method (which we will refer to as the VA method) for identifying the members of moving clusters. This method is based on the analysis of deviations of the proper-motion vectors from the direction of the cluster apex. Van Altena applied his method to the Hyades cluster. The Hyades stream spans about 40° in right ascension and 20° in declination. Other moving clusters and stellar groups of the Galactic disk occupy much smaller areas on the sky, since they are located relatively far from the Sun. The VA method works excellently in these cases, since the cluster stars are located within one-quarter of the celestial sphere, so that the angles between various directions (a star and the celestial pole, etc.) do not exceed 90° and the trigonometric functions do not change signs. However, the VA method must be modified to be applied to the Ursa Major (UMa) moving group, which occupies the entire celestial sphere, or to field stars. We report here a solution to the standard set of three equations for a "star—celestial pole—apex" spherical triangle, which makes it possible to apply the VA method to stellar samples regardless of the size of the areas they occupy on the sky. The reason van Altena [1] had to restrict his analysis to stars located within one-quarter of the celestial sphere is that he used only one of these equations.

Below, we derive the formulas for our version of the VA method. We use a simple model to analyze the relationship between the position of a star on the sky and its position in the proper-motion diagram. In our model, we consider a sample of stars with identical space velocities distributed quasi-uniformly on the sky. To compare our model analysis with observations, we also constructed the proper-motion diagram for a sample based on observations made by the Hipparcos satellite [2]. We consider three forms of the proper-motion diagrams: in equatorial coordinates, in VA coordinates, and in reduced coordinates.

New applications of classic methods of statistical astronomy have now become possible with the availability of catalogs based on observations made by the Hipparcos satellite, which enabled astrometric parameters to be measured with an accuracy of 1 milliarcsecond (1 mas). The availability of more accurate and extensive data has led to qualitative improvements in the results of these methods. In the current paper, we describe the methodological part of our ongoing analysis of the Ursa Major moving group. In [3], we analyzed the core of the moving group, which occupies a considerable fraction of the Big Dipper: a region of sky about 30° in size. Our studies of the entire moving group have required that the domain of applicability of the VA method be extended to the entire celestial sphere, and it is this problem we address in this paper.

2. GEOMETRY OF THE METHOD

The standard formulas for the star—celestial pole—cluster apex spherical triangle shown in Fig. 1a have the form

$$\cos\lambda = \sin D \sin\delta + \cos D \cos\delta \cos(A-\alpha), \quad (1)$$
$$\sin\lambda \sin\theta = \cos D \sin(A-\alpha),$$
$$\sin\lambda \cos\theta = \sin D \cos\delta - \cos D \sin\delta \cos(A-\alpha).$$

Here, α and δ are the equatorial coordinates of star S. The proper motion of this star is μ, and is directed toward the apex K with the coordinates (A, D). These equations also contain λ, the angular separation between the star and the apex, and θ, the angle between the directions from the star to the apex and from the star to the celestial pole (P). These angles are required

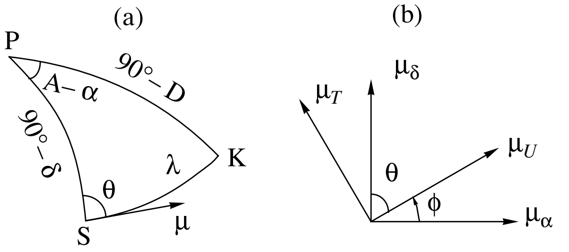

Fig. 1. (a) The star–apex–celestial pole spherical triangle. (b) Rotation of the axes of the Cartesian coordinate system for the proper motions by the angle $\varphi = 90° - \theta$.

to rotate the axes of the equatorial coordinate system through the angle $\varphi = \pi/2 - \theta$ and to transform the proper-motion components μ_α, μ_δ into the VA system. Note the similarity of the two coordinate systems indicated above. Their centers are fixed to the star. The component μ_δ in the equatorial system is always directed toward the North or South Pole, whereas the component μ_U in the VA system is directed toward the apex. Figure 1b illustrates a rotation of the coordinate axes. The angle θ can be found from the second and third equations of (1) via the function $\operatorname{arctg}\theta$, provided that allowance is made for the signs of the sine and cosine functions in the interval from 0° to 360°. The angle λ can take values from 0° to 180° and can be determined from the first equation of (1). These angles determine the directions of the resulting components μ_U and μ_T, regardless of the positions of the star and the apex on the sky. In the VA coordinate system, the proper-motion components are computed using the formulas

$$\mu_U = \mu_\alpha \cos\varphi + \mu_\delta \sin\varphi, \qquad (2)$$
$$\mu_T = -\mu_\alpha \sin\varphi + \mu_\delta \cos\varphi.$$

The following formulas are used for the inverse transformation:

$$\mu_\alpha = \mu_U \cos\varphi - \mu_T \sin\varphi, \qquad (3)$$
$$\mu_\delta = \mu_U \sin\varphi + \mu_T \cos\varphi.$$

These rotate the coordinate system μ_U, μ_T by the angle $-\varphi$ (Fig. 1b).

The essence of the VA method is analyzing the deviations of μ_T from zero. These deviations are equal to the deviations of the stellar motions from the direction toward the apex, and therefore can be used to assess the cluster membership of each star.

3. REDUCTION OF THE PROPER MOTIONS

Figure 2 shows the positions of two stars on the sky, denoted S_1 and S_2. Let their space velocities V_1 and V_2 be parallel and equal in magnitude. The position of the apex is shown by the letter K. As is evident from Fig. 2, two parallel space velocities that are equal in magnitude $V_1 = V_2$ produce different proper motions $\mu_1 \neq \mu_2$. This effect has nothing to do with the nature of the stellar motions and is a result of the projection of the velocity vectors onto a sphere, so that it makes sense to reduce the proper motions by eliminating the effect of the angle λ. The projections of V_1 and V_2 are equal to the proper motions $\mu_1 = V_1 \sin\lambda_1/4.738 r_1$ and $\mu_2 = V_2 \sin\lambda_2/4.738 r_2$, where r_1 and r_2 are the heliocentric distances of the two stars. Turning now to any of the stars in a real cluster located at a heliocentric distance R with the observed proper-motion component equal to μ_U, we can reduce this proper motion to the cluster center, which is located at an angular distance of λ_c and heliocentric distance of R_c. The reduced value of the proper motion μ_U is equal to $\mu_{U_c} = \mu_U(\sin\lambda_c/\sin\lambda)(R/R_c)$. The factor R/R_c represents an additional correction of the magnitudes of the proper motions to reduce them to the same heliocentric distance. The vectors μ_T are perpendicular to the KOS plane in Fig. 2 and are independent of λ but depend on R and so must be corrected to allow for distance differences. In much the same way as for μ_U, we obtain $\mu_T = V_t/kR$ and $\mu_{T_c} = V_t/kR_c$, and we finally have $\mu_{T_c} = \mu_T R/R_c$.

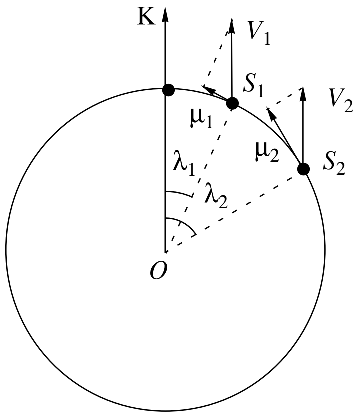

Fig. 2. The proper motions μ_1 and μ_2 as projections onto the sky of the space velocities V_1 and V_2 of stars S_1 and S_2.

4. MODEL OF THE MOTIONS OF FIELD STARS

We now use a simple model to analyze the relationship between the positions of the stars on the sky and their positions in the proper-motion diagram. This model consists of 10 270 stars moving in the direction of the solar antapex, with coordinates $A_{a\odot} = 91°$ and $D_{a\odot} = -30°$ [4]. This model can be thought of as a flow of stars moving toward its own apex with coordinates $A = A_{a\odot}$ and $D = D_{a\odot}$: the stars reflect the motion of the Sun toward its apex,

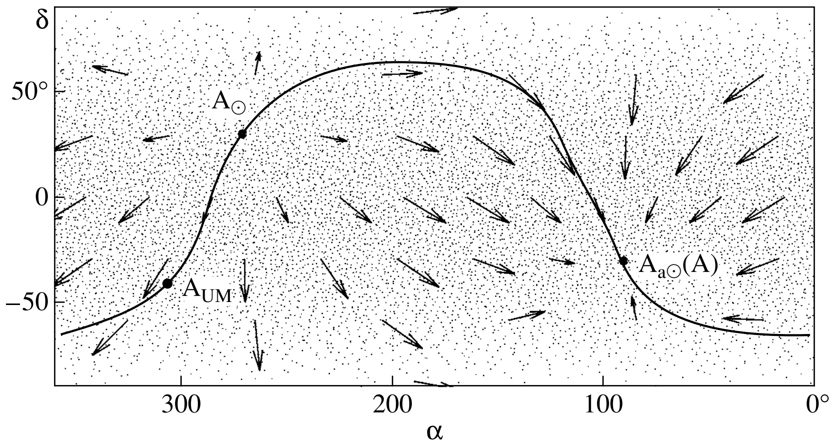

Fig. 3. Cartesian projection of the sky distribution of the simulated stellar sample. The arrows indicate the proper-motion vectors for some of the stars. The magnitudes of the vectors are corrected to make the space velocities of all the stars equal. The curve shows the projection onto the celestial sphere of the circle passing through the apex of the Ursa Major moving group and the solar antapex.

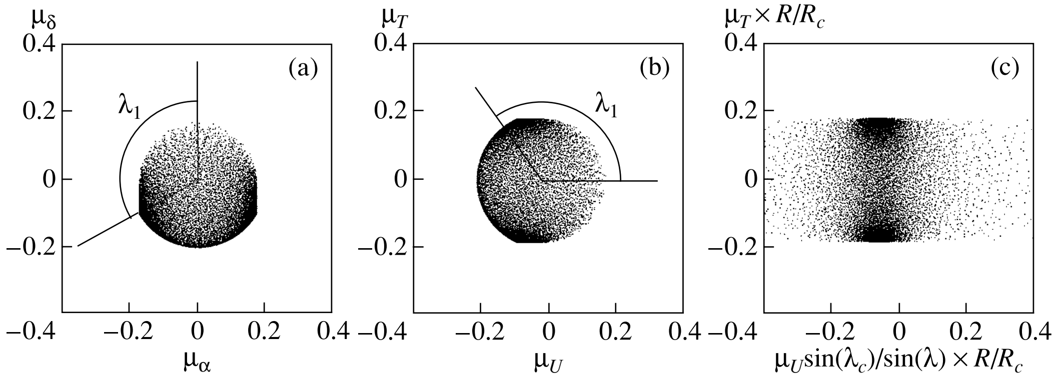

Fig. 4. Proper-motion diagrams (in mas/yr) for the model of the field-star motions (a) in equatorial coordinates, (b) in VA coordinates, and (c) in reduced coordinates in the VA system.

with the coordinates $A_\odot = 271°$ and $D_\odot = 30°$. The sky distribution of stars is quasi-uniform with a density of one star per 4 square degrees. The coordinates of the stars were taken in the form of a grid: $\alpha_i = \Delta\alpha \cdot i + \delta\alpha_i$, where $\delta\alpha_i$ are small random deviations within the interval $\Delta\alpha = 2\%/\cos\delta$. The declinations $(\delta\alpha_i)$ were taken of each α_i on the δ circle at 2° steps with random deviations on the $\pm 1°$ interval.

Because the stars in our model move exactly toward the apex, we have $\mu_T = 0$ for all the stars. Since all the stars have equal space velocities, we set the μ_U components equal to

$$\mu_{U_i} = M \sin\lambda_i. \tag{4}$$

We used the same constant magnitude $M = 200$ mas/yr for all the stars. Figure 3 shows the distribution of model stars on the sky and the field of the proper-motion vectors. All the stars are located at the same distance from the observer.

5. RELATIONSHIP BETWEEN THE POSITIONS OF A STAR ON THE CELESTIAL SPHERE AND IN THE PROPER-MOTION DIAGRAM

Figure 4 shows the proper-motion diagrams constructed for our model using the method described in Sections 2 and 3. The model stars move toward the solar antiapex, and the VA coordinate system is oriented toward the UM apex: $A = 300\overset{\circ}{.}7$ and $D = 29\overset{\circ}{.}7$. It is evident from Figs. 4a and 4b that the domains occupied by the stars have regular figures bounded by arcs and vertical lines. The stellar-density distribution in the diagrams is not uniform and shows conspicuous concentrations of points in the "corners." Why do the diagrams have these shapes? How are the positions of the stars inside these figures related to their positions on the sky? We can now begin to answer these questions. We use relations (3) and (4)

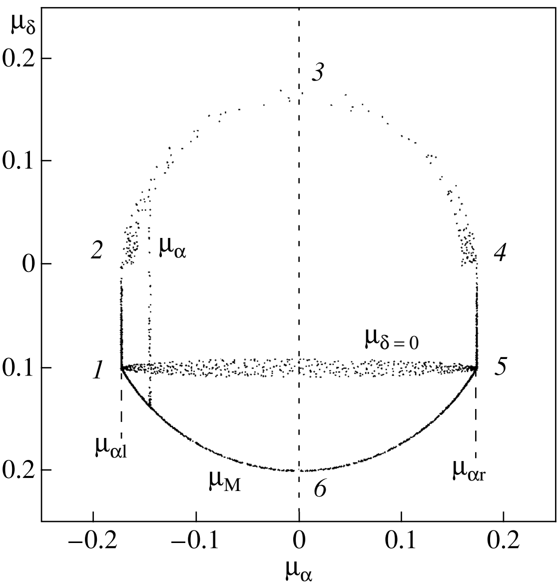

Fig. 5. Some details of the proper-motion diagram (in mas/yr) shown in Fig. 4a. The points show stars located in the regions marked in Fig. 6. The coordinates of the numbered points are: *1* $(-M\cos D,\ M\sin D)$, *2* $(-M\cos D,\ 0)$, *4* $(M\cos D,\ 0)$, and *5* $(M\cos D,\ M\sin D)$.

to obtain:

$$\mu_\alpha = M\sin\lambda\cos\varphi, \qquad (5)$$
$$\mu_\delta = M\sin\lambda\sin\varphi.$$

We then recall that $\varphi = \pi/2 - \theta$ (Fig. 1b) to derive relations for the last two inequalities in (1) in the form

$$\mu_\alpha/M = \cos D\sin(A-\alpha), \qquad (6)$$
$$\mu_\delta/M = \sin D\cos\delta - \cos D\sin\delta\cos(A-\alpha). \qquad (7)$$

We now rewrite (6) in the form $\sin(A-\alpha) = \dfrac{\mu_\alpha}{M\cos D}$ and denote $A_1 = \arcsin\dfrac{\mu_\alpha}{M\cos D}$ to obtain for each μ_α value in the proper-motion diagram ggtwo values of the coordinate α on the celestial sphere. Figures 5 and 6 illustrate this result more clearly. We can see from Fig. 6 that the stars are located on the celestial sphere within the intervals $\alpha_{1,2} = (A-\pi/2) \pm (\pi/2 - A_1)$ or $\alpha_{1,2} = (A+\pi/2) \pm (\pi/2 + A_1)$, depending on which of the two inequalities, $\mu_\alpha > 0$ or $\mu_\alpha < 0$, is satisfied. The first case shows symmetry and the positions of the stars lie close to the line $A - \pi/2$, while, in the second case, the stars lie close to the line $A + \pi/2$. This means that symmetric regions of the sky are projected into the same region of the proper-motion diagram. Thus, the proper-motion diagrams constructed separately for stars in the intervals from $\alpha = A - \pi/2$ to $\alpha = A + \pi/2$ and from $\alpha = A + \pi/2$ to $\alpha = A - \pi/2 + 2\pi$ have the same shapes but lower densities.

It follows from (6) that the boundary values for μ_α in the diagram in Fig. 5 are $\mu_{\alpha\mathrm{r}} = M\cos D$ and $\mu_{\alpha\mathrm{l}} = -M\cos D$. Stars with these $\mu_{\alpha\mathrm{l}}$ and $\mu_{\alpha\mathrm{r}}$ values lie along the line segments shown in Fig. 6: $\alpha_\mathrm{r} = (A - \pi/2)$ and $\alpha_\mathrm{l} = (A + \pi/2)$ (unlike the previous case, we see no forking here).

Note that the possible μ_α values in Fig. 5 do not reach the maximum specified by the model, $|\mu| = 200$ mas/yr. In accordance with (6), the maximum value of μ_α is $\mu_{\alpha\max} = |M\cos(-30°)| = 173$ mas/yr when $\alpha = A \pm \pi/2$ [at the maximum of $|\sin(A-\alpha)|$ in (6)].

Stars with $\delta = 0$ represent a special case, which is also shown in Fig. 6. It can readily be seen from (7) that, in this case, μ_δ is the same for all α, and is equal to $\mu_\delta = M\sin D = -100$ mas/yr, as is shown by the band between points 1 and 5 in Fig. 5.

6. THE SHAPE OF THE PROPER-MOTION DIAGRAM

We will now demonstrate that the shape of the diagram in Fig. 4a can also be interpreted in terms of Eqs. (1). To this end, we derive formulas describing the boundaries of the figures in Fig. 5: the upper and lower arcs and the lateral line segments. Let us consider Fig. 5, which shows the regions of the diagrams indicated in Fig. 4a. These regions enable us to trace the boundaries and show their positions on the sky. As we point out above, the lateral boundaries of the diagrams form vertical line segments. The equations describing these segments follow from (6) when $\sin(A-\alpha) = \pm 1$; i.e., $\alpha_{\mathrm{l,r}} = A \pm \pi/2$. In this case, the left-hand side of (6) acquires its maximum or minimum value, respectively. Thus, formula (6) implies that $\mu_{\alpha\mathrm{r}} = M\cos D$ and $\mu_{\alpha\mathrm{l}} = -M\cos D$ for the right- and left-hand boundaries, respectively. We also find by substituting $D = -30°$ that the maximum and minimum μ_α values are $\pm|M\cos(-30°)| = \pm 173$ mas/yr and are reached when $\alpha = A \mp \pi/2$. On the sky, these stars have right ascensions $\alpha_\mathrm{l} = A + \pi/2$ and $\alpha_\mathrm{r} = A - \pi/2$, respectively, when $-\pi/2 \le \delta \le \pi/2$ (see the vertical regions in Fig. 6).

It follows from (7) that at $\alpha = A \pm \pi/2$

$$\mu_\delta = M\sin D\cos\delta. \qquad (8)$$

We will make use of this property below. We now derive formulas describing the arcs forming the upper and lower boundaries of the diagram in Fig. 5. To this end, we transform (6) to a form that includes the sine of a difference of two angles. We introduce

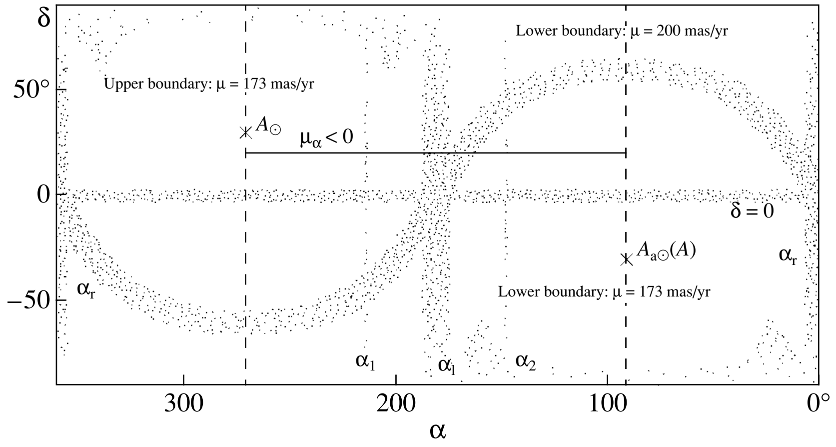

Fig. 6. Projection of the celestial sphere onto a plane. The points indicate stars from various regions shown on the proper-motion diagram (Fig. 5). Each μ_α in Fig. 5 has two corresponding values in this figure, α_1 and α_2. The value $\mu_\alpha = 0$ corresponds to $\alpha_1 = A_{a\odot}$ and $\alpha_2 = A_\odot$. Each of the boundary values $\mu_{\alpha\mathrm{l}}$ and $\mu_{\alpha\mathrm{r}}$ has only one corresponding value, $\alpha_\mathrm{l} = A_{a\odot} + \pi/2$ and $\alpha_\mathrm{r} = A_{a\odot} - \pi/2$, respectively. The dashed lines delineate the region $\mu_\alpha < 0$ located between the solar apex and antapex: $A_{a\odot} \le \alpha \le A_\odot$.

the variable $\eta = \sqrt{\sin^2 D + \cos^2 D \cos^2(A-\alpha)}$ and define the auxiliary angle ψ via the functions

$$\sin\psi = \sin D/\eta, \tag{9}$$

$$\cos\psi = \cos D\cos(A-\alpha)/\eta. \tag{10}$$

The equality (7) can then be transformed to the form

$$\mu_\delta/M = \eta\sin(\psi-\delta). \tag{11}$$

To find formulas for the upper and lower arcs, let us consider the extrema for μ_α and μ_δ. When $\eta = 1$, the angles ψ and D have the same sines [see (9)], and, when $\cos(A-\alpha) \pm 1$, they also have identical cosines, to within the sign [see (10)]. In this case, these angles are either equal to each other or differ by π: $\psi = -\pi - D$. Overall, the ψ values lie in the interval $-\pi - D \le \psi \le D$, and the $\psi - \delta$ values lie in the interval from $-\pi - D - \pi/2$ to $\pi/2 + D$. Because, by definition, $\eta \le 1$, it follows from (9) that $\sin\psi| \le |\sin D|$. We can now use Fig. 7 to find the maximum and minimum of the sine of the difference $\psi - \delta$.

Let us now find the μ_δ boundaries for a single specified μ_α. The lower boundary is $\mu_\delta = -M\eta$, and is attained when $\delta = \pi/2 + \psi$. The upper boundary is $\mu_\delta = M\cos D \times |\cos(A-\alpha)|$, and is attained when $\delta = -\pi/2$ if $A - \pi/2 \le \alpha \le A + \pi/2$ and when $\delta = \pi/2$ if $(A+\pi) - \pi/2 \le \alpha \le (A+\pi) + \pi/2$. We now proceed to obtaining formulas for the upper and lower boundaries. It is evident from Fig. 5 that these boundaries have the form of circular arcs centered on $(0, 0)$. It can readily be seen from (6) and the expression for the lower boundary of μ_δ that the lower arc obeys the equation

$$\mu_\alpha^2 + \mu_\delta^2 = M^2(\cos^2 D\sin^2(A-\alpha) + \sin^2 D + \cos^2 D\cos^2(A-\alpha)) = M^2.$$

Any pair of values (μ_α, μ_δ) that satisfies this equality gives the coordinates of a point on the arc of radius M. From formula (6) and the expression for the upper boundary of μ_δ, we have $\mu_\alpha^2 + \mu_\delta^2 = M^2(\cos^2 D\sin^2(A-\alpha) + \cos^2 D\cos^2(A-\alpha)) = M^2\cos^2 D$. The pair of values (μ_α, μ_δ) that satisfies this equality gives the coordinates of the point on an arc of radius $M\cos D$. In the interval $-M\cos D \le \mu_\alpha \le M\cos D$, the points ($\mu_\alpha$, μ_δ) of the upper boundary sweep from point 2 (Fig. 5) through the maximum [point 3, formula (12)], equal to $(0, M\cos D)$, to point 4; i.e., the upper boundary forms a semicircle of radius $M\cos D$ with both ends lying on the x axis. The points below the lower boundary sweep from left to right in Fig. 5, from

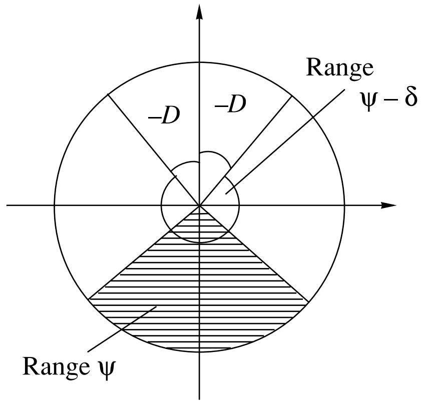

Fig. 7. Schematic of the angles in the proper-motion diagram. The boundaries of the angles ψ and $\psi - \delta$ are shown.

point 1 through the maximum (point 6), equal to $(0, -M)$ [see (13)], to point 5. It has the form of a circular arc of radius M whose ends are bounded by the angles D and $\pi - D$ from the positive direction of the X axis, as is also evident from Fig. 5. The ends of this arc intersect the vertical segments $\mu_{\alpha\mathrm{l}}$ and $\mu_{\alpha\mathrm{r}}$, forming the characteristic "angles" in the $\mu_\alpha - \mu_\delta$ diagram (Fig. 4a). We can find the maximum μ_δ of the set of upper limiting values:

$$\mu_\delta = M\cos D|\cos(A-\alpha)| = M\cos D \qquad (12)$$

when $|\cos(A-\alpha)| = 1$; i.e., $\alpha = A, A+\pi$. We have in this case $\sin(A-\alpha) = 0$ and, therefore, $\mu_\alpha = 0$. The above is also true for $\delta = -\pi/2$, $\alpha = A$ and $\delta = \pi/2$, $\alpha = A + \pi$. The condition for the minimum

$$\mu_\delta = -M\eta = -M \qquad (13)$$

is satisfied when $|\cos(A-\alpha)| = 1$, i.e., for the same α and μ_α as the condition for the maximum. We have taken the maximum value $\eta = 1$. The second coordinate of these points on the celestial sphere are $\delta = \pi/2 + \psi$, where ψ was taken for $|\cos(A-\alpha)| = 1$, namely, D, $-\pi - D(D < 0)$ in the cases $\cos(A-\alpha) = 1$ and $\cos(A-\alpha) = -1$, respectively; it follows that $\delta = D + \pi/2, -D - \pi/2$.

We thus find an interesting relationship between the map on the sky and the $\mu_\alpha - \mu_\delta$ diagram: each vertical line in the rectangular projection in the sky map (a declination circle on the celestial sphere) $\alpha = \mathrm{const}$ is mapped into a vertical segment $\mu_\alpha = \mathrm{const}$ in the $\mu_\alpha - \mu_\delta$ diagram. In this case, a single segment $\mu_\alpha = \mathrm{const}$ is mapped into two vertical lines on the sky $\alpha = \mathrm{const}$, except for the boundaries: the left and right boundaries of the $\mu_\alpha - \mu_\delta$ diagram are each mapped into a single vertical line $\alpha = \mathrm{const}$. In our sky map in Fig. 6, the boundaries of the $\mu_\alpha - \mu_\delta$ diagram correspond to a vertical line halfway between the solar apex and antiapex, so that the left and right boundaries of the diagram correspond to vertical lines located $\pi/2$ to the right and left of the apex, respectively. These two lines are the symmetry axes for the pair of vertical lines $\alpha = \mathrm{const}$ that correspond to the segment $\mu_\alpha = \mathrm{const}$ (except, as noted above, for the boundaries of the diagram): when $\mu_\alpha < 0$, the corresponding pair on the sky map is located on either side of the line $\alpha = A + \pi/2$ at a distance that does not exceed $\pi/2$. When $\mu_\alpha > 0$, the pair is located near the line $\alpha = A - \pi/2$. When $\mu_\alpha = 0$, the corresponding pair of verticals on the sky map passes through the apex and antapex of the stream.

7. STRUCTURE OF THE PROPER-MOTION DIAGRAMS

We used (6) to derive the condition for the extremum of μ_α: $\sin(A-\alpha) = 1$, which is satisfied when $\alpha = A \pm \pi/2$. As is evident from Fig. 4, the regions with a high density of points (the "angles") are located at the maximum and minimum values of μ_α (Fig. 4a). The directions toward these regions from the coordinate origin make angles $\lambda_{1,2} = \pm(\pi/2 - 0)$ to the μ_δ axis.

We have discovered an important property of the diagrams: the angle between the μ_δ axis and the direction from the coordinate origin to a region where the data points are concentrated in the diagram is equal to the angle between the celestial pole and the solar apex. This conclusion is independent of the direction chosen for the coordinate axes. If we have a sample that includes stars forming a stream, the presence of two symmetrically located regions of enhanced point density indicates that the direction chosen for the μ_U axis differs from the direction toward the antapex of the stream.

8. TRANSFORMATION TO THE VA COORDINATE SYSTEM

In the VA method, the observed μ_α and μ_δ are used to perform a linear transformation to μ_U and μ_T [see (2)]. However, this transformation would complicate the mathematical manipulations performed in Sections 5 and 6. As is evident from Section 5, the proper-motion diagram constructed in equatorial coordinates enables us to clearly trace the relationship between the position of a star on the sky and its position in the proper-motion diagram. This is why we analyzed this diagram in the coordinates $\mu_\alpha - \mu_\delta$. In practice, however, diagrams constructed in the VA system are useful for analyses of moving clusters.

The above arguments remain valid when comparing the positions of stars on the sky and in the $\mu_U - \mu_T$ diagram provided the following modifications are made. The great circle with the pole at the UM apex is taken as the equator of the coordinate system. In this case, the coordinates α and δ on the sky are replaced by T and U, respectively. Thus, a new U, T coordinate system is defined on the celestial sphere. In the proper-motion diagram, the μ_α and μ_δ axes are replaced by the μ_T and μ_U axes, respectively. When going from the $\mu_\alpha - \mu_\delta$ system to the $\mu_U - \mu_T$ system, the positions of stars are not mapped conformally, but the diagrams will be similar to each other. For example, the shapes of the diagrams in Figs. 4a and 4b do not exactly coincide. In our case, they are similar to each other only because the angle between the celestial pole and the solar antapex is approximately equal to the angle between the UM apex and the solar antiapex.

Why do we need such a transformation? An important feature of the diagrams associated with the apex is that, if we point the μ_U axis toward the apex of a moving cluster, stars that are members of this cluster will be concentrated at a single point in the $\mu_U - \mu_T$ diagram. This property of the diagram can be used to identify the members of a moving group. In the case of our model, the diagrams in Figs. 4b and 4c collapse into points if we direct the μ_U axis toward the solar antapex. Real groups of stars will not form a point but instead a clump of points with some finite size, due to the scatter of the space velocities of the stars in the stream and the errors in the measured proper motions and parallaxes.

Thus, we show in Figs. 4b and 4c diagrams with the μ_U axis directed toward the apex of the Ursa Major stream. This choice is determined by our analyses of this stream. In a future paper, we wiill report our results for the analysis of the stream as a whole. The diagrams in Figs. 4b and 4c show field stars, among which we wish to identify the stars belonging to the Ursa Major stream. The region $-3 \leq \Delta\mu_T \leq 3$ mas/yr and $100 \leq \Delta\mu_U \leq 110$ mas/yr should contain stars in the core of the Ursa Major stream [3], and a broader region should contain stars from the entire stream.

9. NEARBY STARS IN THE HIPPARCOS CATALOG

To construct the observed diagram shown in Fig. 8, we drew a sample of 16 972 stars scattered over the entire celestial sphere from the Hipparcos catalog [2]. To reduce the effect of uncertainties in the proper-motion measurements, we used only stars with proper-motion errors no greater than 1 mas/yr and heliocentric distances no greater than 150 pc. Our sample consists primarily of A–F stars. This composition of the sample corresponds kinematically to the solar motion in the Galactic disk adopted in our model (see Section 3).

Figure 8 shows the observed diagram constructed in the reduced coordinate system, while Figure 4c shows the analogous model diagram. The diagrams in Figs. 4c and 8 have similar structures, despite the simplicity of our model: stars are concentrated in regions located in the directions toward the solar apex, seen against the overall background of nonuniformly distributed stars. The scatter of μ_T in the observed diagram is much greater than the 200 mas/yr level adopted in the model. This indicates that the proper motions of the field stars exceed the adopted model constraints.

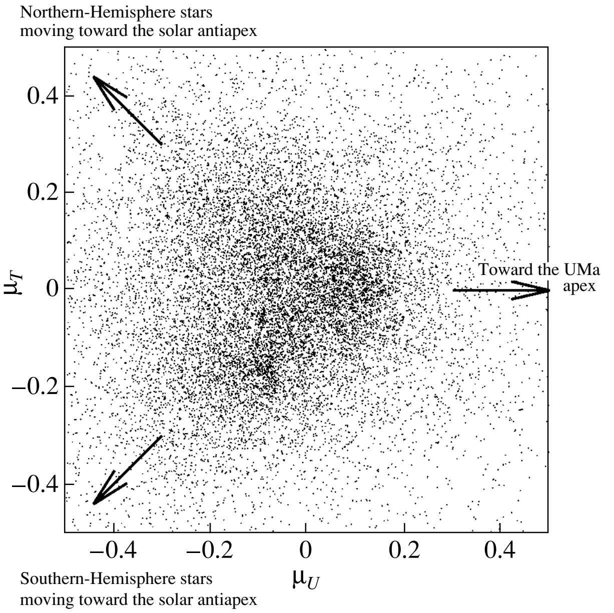

Fig. 8. The observed proper-motion diagram (in mas/yr) constructed in this paper.

Our model does not include the stars of the Ursa Major stream, and therefore the region in which stars of Ursa Major stream should be concentrated in Fig. 4c (a strip near the μ_T axis) is populated only by field stars. At the same time, the corresponding region of the observed diagram shows a conspicuous concentration of data points in this region. This is partially due to the existence of the Ursa Major stream and partially to the nonuniformity of the overall directional field in the solar neighborhood. One of the Kapteyn streams also shows up in this region.

Thus, we can see in Fig. 8 that regions of concentrations of data points are associated with the motion of the Sun. Most of the stars shown in the diagram move toward the solar antapex. We can also see a small concentration of data points among the stars of the southern hemisphere, which represents the Lupus–Centaurus stream.

10. CONCLUSIONS

(1) Our modification of the VA method enables it to be applied in analyses of the kinematics of field stars and the stars of the Ursa Major stream, which are scattered over the entire celestial sphere. This method was applied earlier only to samples whose areas did not exceed one-quarter of the celestial sphere.

(2) Based on a simple model for the kinematics of the centroid of the nearest stars, we have analyzed the structure of the proper-motion diagram for field stars. We have traced the relationship between the positions of stars on the celestial sphere and their positions in the proper-motion diagram. The proper-motion diagrams form symmetric figures with the shape visible in Figs. 4a and 4b. This shape changes abruptly if we make the transformation to reduced coordinates, as is evident from Fig. 4c.

(3) We have constructed the proper-motion diagram for a sample of stars from the Hipparcos catalog. The observed diagram is similar to the diagram we obtained for our model. Both diagrams exhibit regions of enhanced density in the direction toward the solar antapex seen against the nonuniform stellar background.

ACKNOWLEDGMENTS

This work was supported by the Russian Foundation for Basic Research (project no. 01-02-16306).

REFERENCES

1. van Altena, Astron. J. **74**, 2 (1969).
2. *The Hipparcos and Tycho Catalogues* (ESA SP-1200, 1997).
3. N. V. Chupina, V. G. Reva, and S. V. Vereshchagin, Astron. Astrophys. **371**, 115 (2001).
4. C. W. Allen, *Astrophysical Quantities* (Athlone Press, London, 1973).

Translated by A. Dambis